DTU Physics
Department of Physics

Master Thesis

Theory and simulation of microscale acoustic streaming in 3 dimensions

A study in effective modelling

Jacob Søberg Bach
s113069

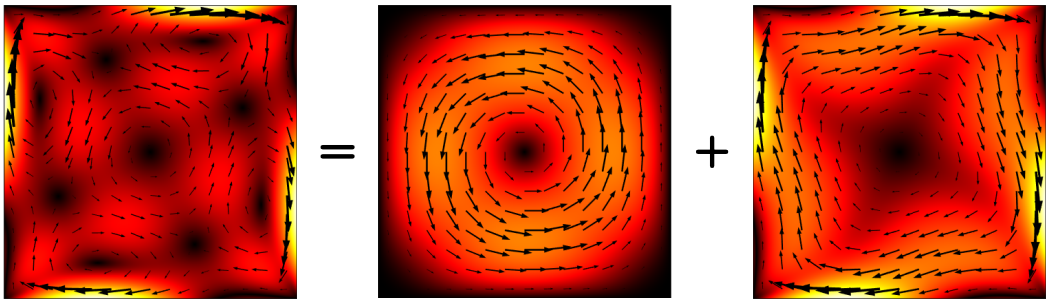

Supervisor: Henrik Bruus

Department of Physics
Technical University of Denmark

22 January 2017

Front page figure shows a beautiful streaming pattern in a square channel which can be thought of as constituted by two kinds of streaming with different physical origin as we will show in Chapter 6 of this thesis.

Abstract

A major challenge within the field of acoustofluidics is to be able to control sub-micron particles suspended in a fluid. Whereas larger particles are successfully focused in an acoustic pressure field, sub-micron particles tend to follow the circulating acoustic streaming instead. Therefore the prediction of acoustic streaming patterns is an important step towards future engineering of acoustofluidic devices. However, due to large velocity gradients inside the so-called acoustic boundary layer a full numeric analysis often requires huge amounts of memory and many larger 3-dimensional systems are very hard to simulate.

In this thesis we present two effective models for calculation of acoustics close to a solid boundary without resolving the acoustic boundary layer numerically. First, we provide a new boundary condition on the acoustic pressure which takes the shear damping inside the acoustic boundary layer into account. We show in an example how we approximate the right resonant properties of an acoustic system in a much more realistic way than the usual approach for effective modelling of acoustic pressure. Secondly, based on the limiting velocity theory developed by Nyborg[1] we derive an effective model for the second order acoustic streaming where we also allow for parallel surface oscillations. More importantly, we formulate a decomposition of the otherwise very complicated streaming equations into three kinds of streaming distinguished by their physical origin: inner streaming, outer streaming and bulk streaming. We then show how this decomposition can be used to analyse a special streaming pattern observed experimentally.

To assess the quality of our modelling we will compare with full simulations where the boundary layers are resolved and find good agreement in most cases. Finally as a proof of concept we use our effective models to simulate acoustic streaming in a larger 3-dimensional system.

Resumé

En af de største udfordringer indenfor feltet akutofluidik er at opnå kontrol over partikler mindre end en mikrometer i en væske. Hvor større partikler let kontrolleres i et akustisk trykfelt, har partikler mindre end en mikrometer tendens til at følge den cirkulerende akustiske strømning i stedet. Det er derfor afgørende at kunne forudsige de akustiske strømningsmønstre med henblik på at designe nye systemer indenfor akustofluidik. Desværre, på grund af store hastighedsgradienter indenfor det så-kaldte akustiske grænselag, kræver en fuld numerisk analyse ofte ekstremt meget hukommelse og større 3-dimensionelle systemer kan være meget svære at simulere.

I denne opgave præsenterer vi to effektive modeller til beregning af akustik tæt på en fast overflade, hvor det akustiske grænselag ikke behøver at blive numerisk opløst. Først opstiller vi en ny grænsebetingelse for det akustiske tryk, som tager højde for den viskøse dæmpning inden i det akustiske grænselag. Vi viser med et eksempel, hvordan vi kan estimere resonansegenskaber for et akustisk system på en langt mere realistisk måde end med den hidtil anvendte effektive model for akustisk tryk. Dernest, med udgangspunkt i Nyborgs[1] grænsehastighedsteori, udleder vi en effektiv model for anden ordens akustisk strømning, hvor vi også tilader parallelle overfladehastigheder. Det vigtigste bidrag her er dog en dekomposition af de ellers komplicerede ligninger for akustisk strømning, hvor vi opdeler strømingen i tre felter adskilt af deres fysiske årsager: Indre strømning, ydre strømning og intern strømning. Vi viser herefter, hvordan denne dekomposition kan bruges til at forstå et særligt strømningsmønster, som er observeret eksperimentelt.

For at vurdere kvaliteten af vores effektive modeller vil vi sammenligne med fulde simuleringer, hvor det akustiske grænselag er opløst og vi vil se god overensstemmelse i de fleste tilfælde. Til sidst, som et eksempel, vil vi med de effektive modeller vise at vi nu kan simulere akustisk strøming i et større 3-dimensionelt system.

Preface

This thesis is submitted as fulfilment of the prerequisites for obtaining the degree as Master of Science and Engineering in Physics and Nanotechnology at the Technical University of Denmark. The work was carried out at the Department of Physics in the Theoretical Microfluidics group (TMF) headed by Professor Henrik Bruus. The duration of the project was 5 months from 22 September 2016 to 22 January 2017 corresponding to 30 ECTS points.

First and foremost I would like to thank my supervisor Henrik Bruus for many inspiring discussions about physics through which I have gradually seen what it means to be a real physicist. Also I would thank the remaining part of the TMF group, Mikkel Ley and Jonas Karlsen for beeing the good old experienced guys, my office-buddy Nils Skov for brewing the best coffee and for his technical help, and Wei Qui for some nice pizza-evenings during the work. Further I will thank the TMF alumni in particular Peter Muller for their important fundamental work which this projects stands upon.

Finally a special thank goes to my family and friends for their interest and support during this project in particular to my sister Kathrine for proofreading, to my parents, and to my girlfriend Julie.

signature

Jacob Søberg Bach
Department of Physics
Technical University of Denmark
22 January 2017

Contents

List of Figures

List of Tables

List of symbols

Symbol	Description	Unit
Geometry		
$(\cdot)^{\mathrm{s}}$	Property $(\cdot)$ of the surface	
$\partial(\cdot)$	Boundary of $(\cdot)$	
$\boldsymbol{e}_{(\cdot)}$	Unit vector in the direction of increasing $(\cdot)$	
h_ξ, h_η, h_ζ	Scale factor ξ, η, ζ	
H	Height of channel	m
$\mathcal{H}$	Twice the negative mean curvature	m^{-1}
l	Acoustic field variation length scale close to surface	m
l_κ	Curvature variation length scale	m
L	Length of channel	m
$\kappa_{(\cdot)}$	Curvature along coordinate $(\cdot)$	m^{-1}
$\boldsymbol{n}$	Unit normal vector towards fluid	
Ω	Domain	
$\boldsymbol{Q}_{(\cdot)}$	Geometric vector with components $(\kappa_\xi(\cdot)_\xi, \kappa_\eta(\cdot)_\eta)$	m^{-1} $[(\cdot)]$
$\boldsymbol{r}$	Position vector	m
$R_{(\cdot)}$	Curvature radius along coordinate $(\cdot)$	m
R	Minimum curvature radius of surface	m
$\boldsymbol{s}$	Local surface position vector	m
$\boldsymbol{t}_{(\cdot)}$	Unit tangent vector in the direction of increasing $(\cdot)$	
τ_ξ (τ_η)	Torsion of η-curve (ξ-curve) when increasing ξ (η)	m^{-1}
V	Volume	m^3
W	Width of channel	m
(x, y, z)	Cartesian coordinates	m
(ξ, η, ζ)	Local curvilinear coordinates	m
Mathematics		
$\sim$	Similar to	
$\lesssim$	Smaller than or similar to	
$\gtrsim$	Greater than or similar to	
$\approx$	Approximately equal to	
$\propto$	Proportional to	

Symbol	Description	Unit
$\rightarrow$	Approaches	
$\Rightarrow$	Implies	
$\Leftrightarrow$	If and only if	
$\langle(\cdot)\rangle$	Time average of $(\cdot)$ over one period	
$\lvert(\cdot)\rvert$	Absolute value of $(\cdot)$	
$(\cdot)^*$	Complex conjugate of $(\cdot)$	
$(\cdot)_\parallel$	Parallel components of $(\cdot)$	
$\times$	Cross product or multiplication	
$\cdot$	Dot product	
$(\cdot)_0$	Unperturbed value of $(\cdot)$	
$(\cdot)_1$	First order in Ma perturbation of $(\cdot)$	
$(\cdot)_2$	Second order in Ma perturbation of $(\cdot)$	
$\mathbf{0}$	Zero-vector	
$\mathbf{1}$	Identity matrix	
C_n	Coefficient to basis function n	
$C(g)$	Convergence parameter for g	
d	Defect of finite element approximation	
$\partial_{(\cdot)}$	Partial derivative with respect to $(\cdot)$	m^{-1}
$\partial^2_{(\cdot)}$	Partial derivative with respect to $(\cdot)$ twice	m^{-2}
$\boldsymbol{\nabla}$	Gradient operator	m^{-1}
$\boldsymbol{\nabla}\cdot$	Divergence operator	m^{-1}
$\boldsymbol{\nabla}\times$	Curl operator	m^{-1}
∇^2	Laplace operator	m^{-2}
$\mathrm{d}(\cdot)$	Infinitesimal change of $(\cdot)$	
DOF	Degrees of freedom	
ϵ_{ijk}	Levi-Cevita symbol	
g	General field	
$\hat{g}_n$	n'th basis function of general field	
g_{ref}	Reference solution to general field	
F	Generalized force	
h_{bulk} (h_{bl})	Mesh size in the bulk (boundary layer)	m
i	Imaginary unit	
$\boldsymbol{J}$	Generalized flux	
K_{mn}	Stiffness matrix	
$\max\{(\cdot)\}$	Maximum of $(\cdot)$	
$\min\{(\cdot)\}$	Minimum of $(\cdot)$	
n_{mesh}	Spatial resolution of mesh	
$\mathcal{O}(\cdot)$	In the order of $(\cdot)$	
ϕ_m	Test function	
$\mathrm{Re}\{(\cdot)\}$	Real part of $(\cdot)$	

Symbol	Description	Unit
Physics		
$(\cdot)^{\mathrm{E}}$ or $(\cdot)$	Property $(\cdot)$ in the Eulerian picture	
$(\cdot)^{\mathrm{L}}$	Property $(\cdot)$ in the Lagrangian picture	
$(\cdot)^{\mathrm{Res}}$	Property $(\cdot)$ at resonance	
β	Viscosity ratio	
c_0	Speed of sound	$\mathrm{m\,s^{-1}}$
δ	Acoustic boundary layer length scale	m
d_1	Wall oscillation amplitude	m
η_0	Shear viscosity	$\mathrm{Pa\,s}$
η_{B}	Bulk viscosity	$\mathrm{Pa\,s}$
ε	Ratio of shear variations to compressional variations	
E_{ac}	Spatial average of energy density stored in a system	$\mathrm{J\,m^{-3}}$
E_{dis}	Spatial average of dissipated energy density per cycle	$\mathrm{J\,m^{-3}\,s}$
f	Frequency	$\mathrm{s^{-1}}$
g	General field	
G	Boundary velocity profile	
Γ	Bulk damping factor	
Γ^{BL}	Boundary layer damping factor	
κ_0	Compressibility	$\mathrm{Pa^{-1}}$
k_0	Inviscid wave number	$\mathrm{m^{-1}}$
k_{c}	Compressional wave number	$\mathrm{m^{-1}}$
k_{s}	Shear wave number	$\mathrm{m^{-1}}$
$k_{(\cdot)}$	Wave number in $(\cdot)$-direction	$\mathrm{m^{-1}}$
λ	Acoustic wavelength	m
λ_y	Acoustic wavelength in the y-direction	m
Ma	Acoustic Mach number	
ν_0	Kinematic viscosity	$\mathrm{m^2\,s}$
ω	Angular frequency	$\mathrm{s^{-1}}$
p	Pressure	Pa
p_2^w	Second order pressure associated with $\boldsymbol{w}_2$	Pa
$\tilde{p}_2$	Second order effective pressure associated with $\boldsymbol{u}_2$	Pa
$\tilde{p}_2^{\mathrm{Bulk}}$	Second order effective pressure associated with $\boldsymbol{u}_2^{\mathrm{Bulk}}$	Pa
$\tilde{p}_2^{\mathrm{Out}}$	Second order effective pressure associated with $\boldsymbol{u}_2^{\mathrm{Out}}$	Pa
Φ_M	Total mass flux out of system	$\mathrm{kg\,s^{-1}}$
ϕ	Phase difference	
ϕ^{Bulk}	Scalar potential of $\boldsymbol{u}_2^{\mathrm{Bulk}}$	$\mathrm{m^2\,s^{-1}}$
$\boldsymbol{\Psi}^{\mathrm{Bulk}}$	Vector potential of $\boldsymbol{u}_2^{\mathrm{Bulk}}$	$\mathrm{m^2\,s^{-1}}$
Q	Quality factor	
ρ	Mass density	$\mathrm{kg\,m^{-3}}$
S	Ratio of bulk streaming to outer streaming	
$\boldsymbol{\sigma} = \boldsymbol{\tau} - p\mathbf{1}$	Stress tensor	Pa

Symbol	Description	Unit
t	Time	s
U	Magnitude of first order acoustic velocity	$\mathrm{m\,s^{-1}}$
$\boldsymbol{u}$	Long-range fluid velocity vector	$\mathrm{m\,s^{-1}}$
$\boldsymbol{u}_1^0$	$\boldsymbol{u}_1$ evaluated at the surface	$\mathrm{m\,s^{-1}}$
$\boldsymbol{u}_2^{\mathrm{Bulk}}$	Second order bulk streaming	$\mathrm{m\,s^{-1}}$
$\boldsymbol{u}_2^{\mathrm{Lim}}$	Limiting velocity	$\mathrm{m\,s^{-1}}$
$\boldsymbol{u}_2^{\mathrm{Out}}$	Second order outer streaming	$\mathrm{m\,s^{-1}}$
$\boldsymbol{v}$	Total fluid velocity vector	$\mathrm{m\,s^{-1}}$
$\boldsymbol{w}$	Short-range fluid velocity vector	$\mathrm{m\,s^{-1}}$
$Y(y)$	y-dependent part of p_1	Pa
$Z(z)$	z-dependent part of p_1	

Chapter 1

Introduction to acoustofluidics and acoustic streaming

1.1 The field of acoustofluidics

The field of acoustofluidics is an important part of the technological development towards controlled handling of micro particles. In particular within the field of health care and biotechnology it is important to be able to analyse samples by focusing or separating microparticles such as bacteria, vira, or blood-cells. Here acoustofluidics offers a cheap, efficient, and label free method to control particles in their natural medium and without contact. As an example we show in Fig. 1.1(a) an experiment from Adams *et al.*[2] where

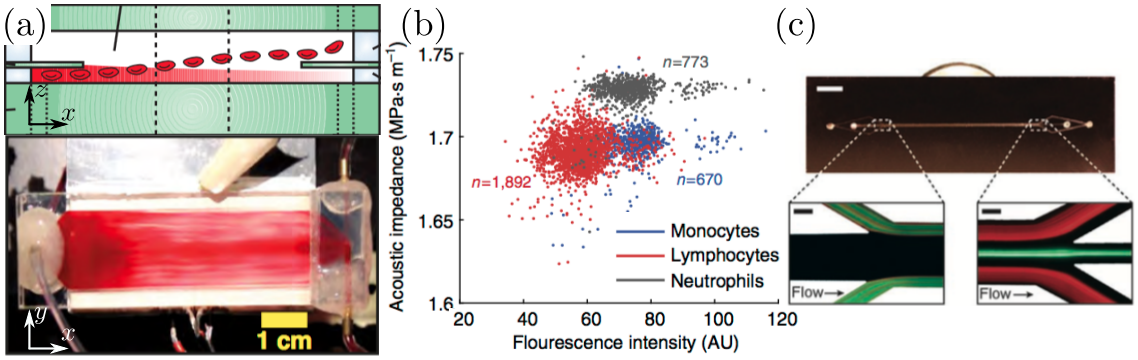

Figure 1.1: Three different applications of acoustofluidics. (a) Set-up from Adams *et al.*[2] for separation of blood cells. Upper: whole blood is injected from the left and due acoustics blood-cells are lifted to the upper outlet in a channel of height 830 µm. Lower: Top view of experiment where blood-cells leave in the lower right corner. (b) Data from Augustsson *et al.*[3] phenotyping three types of white blood-cells based on their acoustic impedance and fluorescence intensity. (c) Experimental setup from Thévoz *et al.*[4]. Upper: the entire device with flow from left to right (scale bar=5 mm). Lower: Fluorescence micrographs at inlet and outlet. Green (red) marks 5 µm (2 µm) polystyrene beads (scalebar=50 µm).

blood cells are separated from whole blood in a continuous flow due to an acoustic field. Acoustofluidics can also be used along with other methods as in Fig. 1.1(b) showing an experiment by Augustsson *et al.*[3] where both acoustic impedance and fluorescence intensity is used in phenotyping three different kinds of white blood-cells simultaneously. Finally, Fig. 1.1(c) show an experiment Thévoz *et al.*[4] where a mixture of 5 µm and 2 µm particles are separated due to the presence of an acoustic field.

Acoustofluidics is often carried out in microsystems and one of the reasons is clearly seen from Fig. 1.1(c-lower) showing a nice laminar flow. Consequently the acoustic resonance frequencies are typically around $\sim$ MHz. Such a resonance is usually induced by a piezoelectric transducer as sketched in Fig. 1.2 where we also show some of the many complex physical phenomena involved in acoustofluidics. The piezoelectric transducer excites a coupled acoustic mode in both the solid and the fluid. Inside the fluid the acoustic pressure field give rise to particularly two important non-linear effects: (i) Wave-particle scattering on suspended particles which gives the so-called acoustic radiation force on the particles and (ii) acoustic streaming in the fluid (blue rolls in Fig. 1.2) giving viscous drag on the particles. The main focus in this thesis will be on the acoustic streaming.

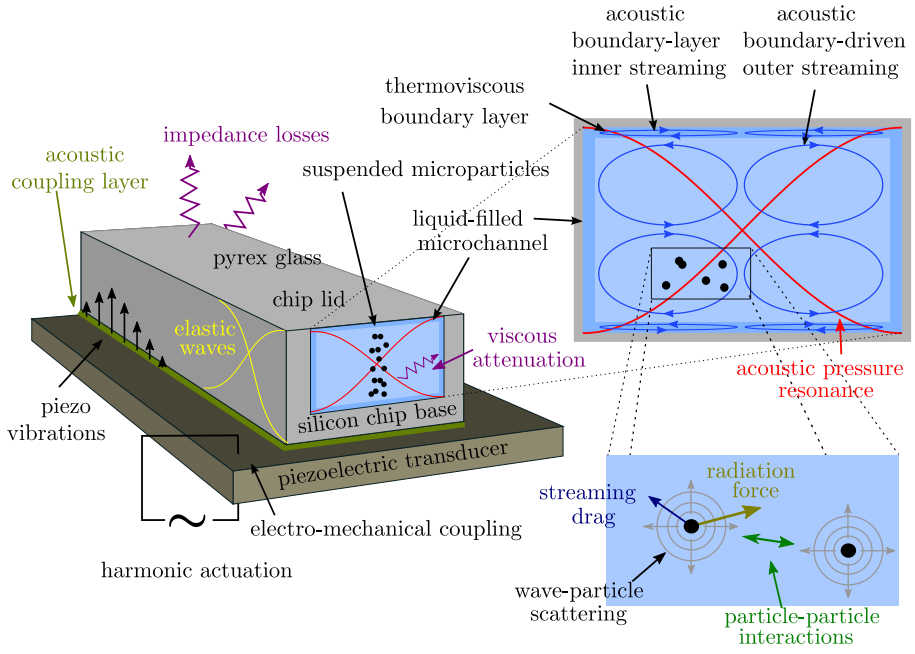

Figure 1.2: Sketch showing different physical aspects in acoustofluidics, adapted from Barnkob[5]. Left: The microchannel is oscillated by a piezoelectic transducer. This initiates oscillations in the channel walls and in the fluid. Right: An acoustic pressure mode (red) is excited in the channel. This gives rise to (i) wave-particle-scattering and (ii) acoustic streaming (blue rolls).

1.2 Acoustic streaming

The importance of acoustic streaming in acoustofluidic devices is best understood by considering the two most important forces discussed above. The acoustic radiation force usually focuses particles towards pressure nodes and its magnitude scales with the particle volume a^3[6]. The drag force on the other hand follows the circulating acoustic streaming and thus acts as a defocusing force which scales with the surface area a^2 of the particles. Hence, acoustic streaming often sets the lower limit on the particle size that can be focused in acoustic microsystems. This limit turns out to be around 1 µm. Therefore an understanding of the streaming patterns is an essential step in the development of microscale acoustiofluidic systems.

The history of acoustic streaming theory goes back to Lord Rayleigh[7] who first described the phenomenon in 1884. As the theory developed, acoustic streaming fell into three different categories, here referred to as inner streaming, outer streaming, and bulk streaming. In Fig. 1.3 we show the regions where these are observed. In general all acoustic stream-

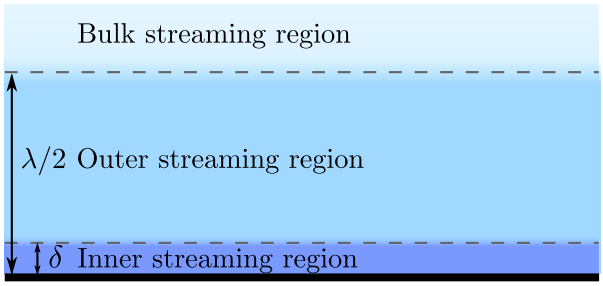

Figure 1.3: Sketch of the different streaming regions close to a wall (black bold line). The inner streaming decays over the length scale $\delta \sim 0.5$ µm whereas the outer streaming decays over the wavelength scale $\lambda/2 \sim 10^2$ µm. The bulk streaming is driven by interior forces and can therefore exist everywhere.

ing is due to nonlinear stress from velocity gradients in an oscillating fluid. When a fluid oscillates near a solid boundary there will be large velocity gradients confined to a narrow region close the the boundary and consequently, there will be large stresses on the fluid in that region, which is called the *acoustic boundary layer* and will be a main topic of this thesis. These stresses inside the boundary layer are responsible for two kinds of streaming: (i) the inner streaming which is confined to the boundary layer and (ii) the outer streaming which is confined to a region comparable with the acoustic wavelength. The third kind of streaming, the bulk streaming, is driven by stresses from velocity gradients in the bulk only. Most often the characteristic length scale of this last kind of streaming is comparable with the system length scale but in special cases shown in this thesis one can have bulk streaming with a length scale comparable with the acoustic wavelength λ.

The bulk streaming (or Eckard streaming[8]) is rarely seen in experiments and in this thesis we will give an estimate on when to expect bulk streaming. The most significant streaming

in experiments is the outer streaming. Lord Rayleigh[7] calculated a special case of outer streaming near flat stationary walls and gave name to the classical Rayleigh streaming pattern which we will explain in Chapter 6 as being characterized by four streaming rolls per acoustic wavelength. However, as we will see in this thesis many different streaming patterns can be observed depending on the geometry and wall oscillation. Finally, the inner streaming (or Schlichting streaming[9]) is also less significant since it is confined to the acoustic boundary layer which has a width of $\delta \sim 0.5$ µm for water in the MHz regime. However, in calculations we cannot ignore the inner streaming since it affects the outer streaming.

The approach by Lord Rayleigh was to use the inner streaming velocity at the edge of the boundary layer as a slip boundary condition on the outer streaming. This idea was later generalized by Nyborg[1] in 1958 for curved surfaces with length scales much larger than the boundary layer thickness δ. Nyborg also introduced the concept of *limiting velocity* as the non-zero velocity of the inner streaming at the edge of the boundary layer which drives the outer streaming. The theory by Nyborg was later adjusted in 1989 by Lee *et al.*[10] with small modifications to the analysis in curvilinear coordinates. Recent advances within the field of acoustofluidics include actuation with surface acoustic waves (SAW) where the wall oscillates both in the parallel and perpendicular direction. This kind of actuation was included to the limiting velocity theory for flat walls by Vanneste *et al.* [11] in 2010. In this thesis one of of the main goals is to combine these theories and formulate a limiting velocity theory for curved walls with both parallel and perpendicular actuation.

The limiting velocity theory is an effective modelling of the acoustic boundary layer which gives a great insight in the essential physics involved. Further as many other effective models this one also has a great impact within computational physics which has developed significantly over the past few decades. As an example from *Web Of Science* (6. Jan 2017) the paper by Nyborg from 1958 has received 183 citations where 150 are received within the past 20 years within fields from acoustics, biochemistry and computer science. The great advantage is that in the effective model one do not have to resolve the large velocity gradients inside the boundary layer. The full numerical simulation of acoustic streaming in 2 dimensions (2D) have been carried out by e.g. Muller *et al.*[12]. However, full simulation of larger 3D systems are not possible on normal workstations and the limiting velocity theory is therefore a great tool to reach simulation of larger systems.

1.3 Outline of the thesis

In this thesis the main focus is on effective modelling of acoustics near a weakly oscillating curved surface. To reach this goal we first need to understand the fundamentals governing fluid equations, the Lagrangian fluid picture at an oscillating boundary, the finite element method for numeric calculations, and the basic geometry of curved surfaces. This will be presented in Chapters 2-4. The important contributions to effective modelling are

then found in Chapters 5-6 and in Chapter 7 we give an example of a 3D calculation of streaming. Hence, the outline of the thesis will be as follows,

Chapter 2: Theory of viscous fluids We introduce the fundamental theory of viscous fluids and introduce basic concepts such as acoustic perturbation theory, field decomposition, acoustic boundary layer, and the viscous damping factor. We then describe the Lagrangian and Eulerian fluid picture through which we establish the boundary condition on a fluid near an oscillating surface.

Chapter 3: The finite element method and memory requirements We briefly introduce the finite element method used in the software COMSOL. We then test the memory requirements for the models considered in this thesis and thus motivate the use of effective models.

Chapter 4: Geometry of curved surfaces and model assumptions In this chapter we introduce a local curvilinear coordinate system at any point on the surface. We then give an overview of the different length scales of the system and establish the range of validity for our model.

Chapter 5: Effective modelling of acoustic fields near a solid surface We here develop a general analytic expression for the acoustic fields inside the acoustic boundary layer. In particular this leads to the first main result of this theses, namely a new boundary condition on the acoustic pressure at a solid surface which takes the damping effects of the acoustic boundary layer into account. This finally allows a comparison between a full model with the boundary layers resolved numerically and the effective model.

Chapter 6: Acoustic streaming and limiting velocity theory We proceed the effective modelling but now regarding the steady streaming. We present the second main result of the thesis namely a physical decomposition of the streaming into inner, outer, and bulk streaming. Thus formulation is not only a computational advantage but also demystifies the otherwise complicated equations for streaming. Further, we formulate the limiting velocity theory for curved surfaces with both parallel and perpendicular oscillations. We again compare with a full model and we find that our decomposition can be used to understand a special kind of bulk-streaming observed experimentally.

Chapter 7: 3-dimensional acoustic streaming This chapter serves as a proof of concept where we show how we can model streaming in larger 3D systems with the new effective models. This will be shown through an example of acoustic streaming around a sphere in a box, which is of great experimental relevance(e.g. [13]).

Chapter 8: Conclusion and outlook

Chapter 2

Theory of viscous acoustics

In this chapter we present and discuss the governing equations for acoustic motion in viscous fluids. We present the theory of acoustic perturbation theory and show how the acoustic velocity field can be decomposed into a compressional field and a shear field. Finally in the last section we will discuss boundary conditions at a solid wall in the Lagrangian and Eulerian picture.

2.1 Fluid equations

On length scales much larger than the intermolecular distance in fluids ($\sim 0.3\,\mathrm{nm}$ for solids and liquids[14]) we make the *continuum hypothesis* and model fluids as continuous matter filling out all space rather than being constituted by discrete molecules. At each point we then define the Eulerian mass density $\rho(\boldsymbol{r},t)$ and the Eulerian velocity $\boldsymbol{v}(\boldsymbol{r},t)$ of the fluid located at position $\boldsymbol{r}$ at time t. We then claim conservation of mass and momentum in any point in space which is formulated in the continuity equation and Navier-Stokes equations respectively,

$$\partial_t \rho = -\boldsymbol{\nabla}\cdot[\rho\boldsymbol{v}]\,, \tag{2.1a}$$

$$\partial_t(\rho\boldsymbol{v}) = -\boldsymbol{\nabla}\cdot[(\rho\boldsymbol{v})\boldsymbol{v}] + \boldsymbol{\nabla}\cdot\boldsymbol{\sigma}. \tag{2.1b}$$

Here $\boldsymbol{\sigma}$ is the stress tensor defined as,

$$\boldsymbol{\sigma} = -p\mathbf{1} + \boldsymbol{\tau}, \tag{2.2a}$$

$$\boldsymbol{\tau} = \eta_0\left[\boldsymbol{\nabla}\boldsymbol{v} + (\boldsymbol{\nabla}\boldsymbol{v})^{\mathrm{T}}\right] + \left[\eta_{\mathrm{B}} - \frac{2}{3}\eta_0\right](\boldsymbol{\nabla}\cdot\boldsymbol{v})\mathbf{1}, \tag{2.2b}$$

where $\mathbf{1}$ is the unit tensor, p is the pressure, η_0 is the shear viscosity, η_{B} is the bulk viscosity and superscript 'T' denotes transpose. We will in this thesis only consider pure water for which the important parameters are given in Table 2.1.

Eq. (2.1a) expresses that the mass inside a fixed infinitesimal volume element can only change due to convection of mass to that volume element. Eq. (2.1b) states the same for

Table 2.1: Table of parameters[15] used in this thesis for pure water at temperature 25°C and pressure 0.1013 MPa. The three lower parameters are calculated from the upper ones.

Parameter	Symbol	Value	Unit
Mass density	ρ_0	9.970×10^2	$\mathrm{kg\,m^{-3}}$
Compressibility	κ_0	4.477×10^{-10}	$\mathrm{Pa^{-1}}$
Shear viscosity	η_0	8.900×10^{-4}	$\mathrm{Pa\,s}$
Bulk viscosity	η_B	2.485×10^{-3}	$\mathrm{Pa\,s}$
Speed of sound	$c_0 = \sqrt{1/(\kappa_0\rho_0)}$	1.497×10^3	$\mathrm{m\,s^{-1}}$
Kinematic viscosity	$\nu_0 = \eta_0/\rho_0$	8.927×10^{-7}	$\mathrm{m^2\,s}$
Viscosity ratio	$\beta = \eta_\mathrm{B}/\eta_0 + 1/3$	3.125	1

momentum but here momentum can also be changed due to stresses in the i direction on a surface with normal in the j-direction given in σ_{ij}. Combining Eqs. (2.1) and (2.2) we get the Navier-Stokes equations in the well known form,

$$\rho\left(\partial_t + \boldsymbol{v}\cdot\boldsymbol{\nabla}\right)\boldsymbol{v} = -\boldsymbol{\nabla}p + \eta_0\nabla^2\boldsymbol{v} + \eta_0\beta\boldsymbol{\nabla}\left(\boldsymbol{\nabla}\cdot\boldsymbol{v}\right). \tag{2.3}$$

where we have defined the viscosity ratio $\beta \equiv \dfrac{\eta_\mathrm{B}}{\eta_0} + \dfrac{1}{3} \approx 3$ from Table 2.1. Having now 5 dependent variables and only 4 equations we will need a constitutive relation. Therefore we define the isentropic compressibility κ_0 which gives the relative volume change of the fluid due to a change in pressure or equivalently,

$$\kappa_0 \equiv \frac{1}{\rho_0}\left(\frac{\partial\rho}{\partial p}\right)_S, \tag{2.4}$$

where the value of κ_0 for water is given in Table 2.1. As we will see in the below, small pressure perturbations can propagate through space with the speed of sound given by,

$$c_0^2 = \left(\frac{\partial p}{\partial\rho}\right)_S = \frac{1}{\rho_0\kappa_0}. \tag{2.5}$$

The dynamics of acoustic waves will be treated by using acoustic perturbation theory which we will present in the following.

2.2 Acoustic perturbation theory

Acoustic motion is almost always induced from a time harmonic oscillating boundary of the system. This boundary oscillation compresses the fluid a small amount and thereby excites acoustic motion. Please note the distinction between the fluid velocity which has a magnitude U and the parameter c_0. For intuition, consider a fluid with unperturbed density ρ_0 which caries a sound wave of frequency f and wavelength $\lambda = c_0/f$. If the fluid within a section λ is compressed the small distance r_1 the velocity of that fluid will be

$U \sim r_1 f \sim (r_1/\lambda)c_0$. Consequently the density will change the small amount $\rho_1 \sim \rho_0(r_1/\lambda)$ and from Eq. (2.4) the pressure will change $p_1 \sim (r_1/\lambda)/\kappa_0$. We then have the scaling $r_1/\lambda \sim U/c_0 \sim \rho_1/\rho_0 \sim p_1\kappa_0$ and in particular we see that the fluid velocity U is much smaller than c_0 for small displacements compared to the wavelength. This motivates the introduction of the smallness parameter Ma which is called the acoustic Mach number,

$$\mathrm{Ma} \equiv \frac{U}{c_0} \ll 1, \tag{2.6}$$

where we will use U as the magnitude of the acoustic velocity. We will then expand all fields in the following form,

$$\boldsymbol{v} = \boldsymbol{0} + \boldsymbol{v}_1(\boldsymbol{r})\mathrm{e}^{-\mathrm{i}\omega t} + \boldsymbol{v}_2(\boldsymbol{r},t), \tag{2.7a}$$

$$\rho = \rho_0 + \rho_1(\boldsymbol{r})\mathrm{e}^{-\mathrm{i}\omega t} + \rho_2(\boldsymbol{r},t), \tag{2.7b}$$

$$p = p_0 + p_1(\boldsymbol{r})\mathrm{e}^{-\mathrm{i}\omega t} + p_2(\boldsymbol{r},t), \tag{2.7c}$$

where the subscripts indicate order of smallness in the Mach number. In this theses we will always assume this form where the unperturbed zeroth order fields are homogeneous in space and time and where the first order fields are harmonic in time just as the oscillating boundary. For scaling purposes we write down the relation between the order of magnitudes of the fields,

$$1 \gg \mathrm{Ma} \sim \frac{|\boldsymbol{r}_1|}{\lambda} \sim \frac{U}{c_0} \sim \frac{|\rho_1|}{\rho_0} \sim \frac{|p_1|}{1/\kappa_0} \sim \frac{|\boldsymbol{v}_2|}{U} \sim \frac{|\rho_2|}{|\rho_1|} \sim \frac{|p_2|}{|p_1|}, \tag{2.8}$$

where $\boldsymbol{r}_1$ is the fluid displacement vector with $\partial_t \boldsymbol{r}_1 = \boldsymbol{v}_1$.

The oscillatory motion in fluids is then governed by the first order version of Eqs. (2.1a) and (2.3),

$$-\mathrm{i}\omega\rho_1 = -\rho_0 \boldsymbol{\nabla}\cdot\boldsymbol{v}_1, \tag{2.9a}$$

$$-\mathrm{i}\omega\rho_0\boldsymbol{v}_1 = -\boldsymbol{\nabla}p_1 + \eta_0\nabla^2\boldsymbol{v}_1 + \eta_0\beta\boldsymbol{\nabla}(\boldsymbol{\nabla}\cdot\boldsymbol{v}_1). \tag{2.9b}$$

Here we have used that the first order fields are harmonic in time so we will frequently interchange between $\partial_t \leftrightarrow -\mathrm{i}\omega$.

The second order fields have both harmonic and steady components. The harmonic components will be of order Ma compared to the first order fields and thus insignificant. The steady motion on the other hand is qualitatively different from the first order motion and will be measurable in experiments. To get the steady motion we take the time average over one period $\langle(\cdot)\rangle \equiv \frac{1}{2\pi/\omega}\int_0^{2\pi/\omega}(\cdot)\,\mathrm{d}t$. In particular the time average of products of first order fields is understood as,

$$\langle A_1 B_1\rangle = \left\langle \mathrm{Re}\left\{A_1(\boldsymbol{r})\mathrm{e}^{-\mathrm{i}\omega t}\right\}\mathrm{Re}\left\{B_1(\boldsymbol{r})\mathrm{e}^{-\mathrm{i}\omega t}\right\}\right\rangle = \frac{1}{2}\mathrm{Re}\left\{A_1(\boldsymbol{r})[B_1(\boldsymbol{r}_1)]^*\right\} = \frac{1}{2}\mathrm{Re}\left\{A_1 B_1^*\right\}. \tag{2.10}$$

The second order time averaged version of Eq. (2.1) then become,

$$0 = -\boldsymbol{\nabla}\cdot(\rho_0\boldsymbol{v}_2 + \langle\rho_1\boldsymbol{v}_1\rangle), \tag{2.11a}$$

$$\mathbf{0} = -\boldsymbol{\nabla}p_2 + \eta_0\nabla^2\boldsymbol{v}_2 + \eta_0\beta\boldsymbol{\nabla}(\boldsymbol{\nabla}\cdot\boldsymbol{v}_2) - \boldsymbol{\nabla}\cdot\langle(\rho_0\boldsymbol{v}_1)\boldsymbol{v}_1\rangle\,, \tag{2.11b}$$

where we will only write the average $\langle(\cdot)\rangle$ explicitly on products of first order fields and for now on let subscript 2 denote time-averaged second order fields. Here we have used that $\langle\partial_t(\cdot)\rangle = 0$ for time harmonic fields.
We see that the time averaged Navier-Stokes Eq. (2.11b) is a steady force balance equation where the driving term $-\boldsymbol{\nabla}\cdot\langle(\rho_0\boldsymbol{v}_1)\boldsymbol{v}_1\rangle$ is the divergence of nonlinear stress from the first order velocity. $-\rho_0\boldsymbol{v}_1\boldsymbol{v}_1$ is called the Reynolds stress and is responsible for the steady second order streaming as we will see in Chapter 6.

2.3 Compressional bulk field $\boldsymbol{u}_1$ and shear boundary layer field $\boldsymbol{w}_1$

The first order equations Eq. (2.9b) describe both the physics of (i) compression of fluids which give acoustic motion and (ii) the momentum diffusion due to shear forces inside the fluid where the latter phenomena is most significant close to a solid boundary. In the following we will separate these two phenomena into the fields $\boldsymbol{u}_1$ and $\boldsymbol{w}_1$ respectively.

We first take the divergence of Eq. (2.9b) and use Eq. (2.9a) together with $\rho_1 = p_1/c_0^2$ to see that the pressure satisfies a Helmholtz equation,

$$\nabla^2 p_1 + k_\mathrm{c}^2 p_1 = 0, \tag{2.12a}$$

$$\text{where} \qquad k_\mathrm{c} \equiv k_0\left(1 + \mathrm{i}\frac{\Gamma}{2}\right), \qquad \Gamma \equiv \frac{\eta_0(1+\beta)\omega}{\rho_0 c_0^2}. \tag{2.12b}$$

Here we have defined the compressional wave number k_c, where $k_0 = \omega/c_0$ is the inviscid wave number. Further we have defined the bulk damping factor Γ. For the parameters in Table 2.1 and e.g. $\omega = 2\pi\ \times 10^6$ MHz we find $\Gamma \approx 10^{-5}$ so Γ will be treated as a small parameter and all terms of $\mathcal{O}(\Gamma^2)$ will be ignored.

To get an equation for the velocity $\boldsymbol{v}_1$ we instead take the time derivative of Eq. (2.9b) and use Eq. (2.9a) to get,

$$\boldsymbol{\nabla}(\boldsymbol{\nabla}\cdot\boldsymbol{v}_1) - \frac{k_\mathrm{c}^2}{k_\mathrm{s}^2}\boldsymbol{\nabla}\times\boldsymbol{\nabla}\times\boldsymbol{v}_1 + k_\mathrm{c}^2\boldsymbol{v}_1 = \mathbf{0}, \tag{2.13a}$$

$$\text{where} \qquad k_\mathrm{s} \equiv \frac{1+\mathrm{i}}{\delta}, \qquad \delta \equiv \sqrt{\frac{2\nu_0}{\rho_0\omega}}, \tag{2.13b}$$

where we have used that $\nabla^2\boldsymbol{v}_1 = -\boldsymbol{\nabla}\times\boldsymbol{\nabla}\times\boldsymbol{v}_1 + \boldsymbol{\nabla}(\boldsymbol{\nabla}\cdot\boldsymbol{v}_1)$. Here we have defined the shear wave number k_s and δ is the characteristic length scale of momentum diffusion as

we will see soon. For the same parameters as before we find $\delta \sim 0.5\,\mu\text{m}$. Please note the relation between the compressional and shear wave numbers,

$$\frac{|k_\text{c}|^2}{|k_\text{s}|^2} \sim \Gamma = \frac{(1+\beta)}{2}(k_0\delta)^2, \tag{2.14}$$

so the shear length scale δ is usually much smaller than the compressional length scale $1/k_0$.

From Eq. (2.13) we are motivated to make a Helmholtz decomposition of $\boldsymbol{v}_1$ so,

$$\boldsymbol{v}_1 = \boldsymbol{u}_1 + \boldsymbol{w}_1 \qquad \text{where} \qquad \boldsymbol{\nabla}\times\boldsymbol{u}_1 = \boldsymbol{0}, \qquad \boldsymbol{\nabla}\cdot\boldsymbol{w}_1 = 0. \tag{2.15}$$

Inserting this into Eq. (2.13) gives,

$$\left[\nabla^2\boldsymbol{u}_1 + k_\text{c}^2\boldsymbol{u}_1\right] + \frac{k_\text{c}^2}{k_\text{s}^2}\left[\nabla^2\boldsymbol{w}_1 + k_\text{s}^2\boldsymbol{w}_1\right] = \boldsymbol{0}. \tag{2.16}$$

We see that one solution to this problem is found by requiring each bracket to vanish individually from which we find the governing equation of compressional and shear motion respectively.

2.3.1 Nature of the compressional motion

The compressional field $\boldsymbol{u}_1$ satisfy,

$$\nabla^2\boldsymbol{u}_1 + k_\text{c}^2\boldsymbol{u}_1 = \boldsymbol{0}, \qquad \text{with} \qquad k_\text{c} = k_0\left(1 + \text{i}\frac{1}{2}\Gamma\right) \qquad \text{and} \qquad \boldsymbol{\nabla}\times\boldsymbol{u}_1 = \boldsymbol{0}. \tag{2.17}$$

Since the imaginary part of k_c is much smaller than the real part, the significance of $\boldsymbol{u}_1$ will be acoustic waves with a wave length $\lambda \sim 2\pi/k_0$ which are damped over the much longer distance $\sim 1/(k_0\Gamma/2)$. Hence we $\boldsymbol{u}_1$ is a long-range field compared to $\boldsymbol{w}_1$ as we will see. We see that only $\boldsymbol{u}_1$ enters in the continuity equation Eq. (2.9a),

$$\frac{\text{i}\omega}{\rho_0 c_0^2}p_1 = \boldsymbol{\nabla}\cdot\boldsymbol{u}_1, \tag{2.18}$$

where we have used Eq. (2.5) to write $c_0^2\rho_1 = p_1$. From this relation we see that indeed $\boldsymbol{u}_1$ is the compressional velocity. An alternative way of think of this equation is in terms of the fluid displacement $\boldsymbol{r}_1 = \text{i}\boldsymbol{u}_1/\omega$ giving $p_1\kappa_0 = -\boldsymbol{\nabla}\cdot\boldsymbol{r}_1$, where $p_1\kappa_0$ is the relative fluid compression which must be the same as the convergence $-\boldsymbol{\nabla}\cdot\boldsymbol{r}_1$ in the fluid displacement. Please note that is the quantitative description of our estimate above (before Eq. (2.6)). Finally, taking the gradient of Eq. (2.18) and using Eq. (2.17) we can find $\boldsymbol{u}_1$ from p_1,

$$\boldsymbol{u}_1 = \frac{1}{\text{i}\omega\rho_0}\boldsymbol{\nabla}p_1(1 - \text{i}\Gamma). \tag{2.19}$$

Of course, since $\boldsymbol{\nabla}\times\boldsymbol{u}_1 = \boldsymbol{0}$, $\boldsymbol{u}_1$ must be directly related to a scalar, here p_1. So having p_1 one can find $\boldsymbol{u}_1$ and vice versa. In this theses the strategy will be to first solve for p_1 and then use Eq. (2.19) to find $\boldsymbol{u}_1$.
Finally please note that Eq. (2.19) implies that the *total* velocity is,

$$\boldsymbol{v}_1 = \frac{1}{\text{i}\omega\rho_0}\boldsymbol{\nabla}p_1(1 - \text{i}\Gamma) + \boldsymbol{w}_1. \tag{2.20}$$

2.3.2 Nature of the shear motion

We proceed to analyse the properties of the incompressible field $\boldsymbol{w}_1$ satisfying,

$$\nabla^2\boldsymbol{w}_1 + k_\mathrm{s}^2\boldsymbol{w}_1 = \boldsymbol{0} \qquad \text{with} \qquad k_\mathrm{s} = \frac{1+\mathrm{i}}{\delta} \qquad \text{and} \qquad \boldsymbol{\nabla}\cdot\boldsymbol{w}_1 = 0. \tag{2.21}$$

This is also a Helmholtz equation but since k_s has equal real and imaginary parts the solution will oscillate and decay over the same length scale δ and $\boldsymbol{w}_1$ is thought of as a short range field. An alternative way to understand $\boldsymbol{w}_1$ is by writing out $k_\mathrm{s}^2 = (2\mathrm{i})/\delta^2$ with $\delta = \sqrt{2\eta_0/(\rho_0\omega)}$ to find the diffusion equation,

$$\partial_t\boldsymbol{w}_1 = \nu_0\nabla^2\boldsymbol{w}_1. \tag{2.22}$$

where we used $(-\mathrm{i}\omega) \to \partial_t$ and defined the kinematic viscosity $\nu_0 \equiv \eta_0/\rho_0$. The shear field $\boldsymbol{w}_1$ thus describes diffusion of velocity (or momentum) where ν_0 takes the role as diffusion coefficient. Since the fluid oscillates with the angular frequency ω the characteristic diffusion length must be $\delta = \sqrt{2\nu_0/\omega}$.

The field $\boldsymbol{w}_1$ will be most significant close to a solid boundary where the total velocity $\boldsymbol{v}_1 = \boldsymbol{u}_1 + \boldsymbol{w}_1$ has to vanish due to the no-slip boundary condition (see Section 2.4). It will then be confined to a narrow region of width $\sim 5\delta$ close to the surface which is called the acoustic boundary layer.

2.4 The Lagrangian and Eulerian fluid picture

So far all fields have been formulated in the Eulerian picture, i.e. where we ask for any property g of the fluid at some fixed point $\boldsymbol{r}$ and time t and get $g^\mathrm{E}(\boldsymbol{r}, t)$. We should however be aware that the fluid at $\boldsymbol{r}$ might move away from that point such that $g^\mathrm{E}(\boldsymbol{r}, t+\mathrm{d}t)$ describe some other fluid particles that just arrived to that point. In particular, close to an oscillating boundary the Eulerian picture fails because some fixed point $\boldsymbol{r}$ might refer to the fluid at one instant of time and to the solid the next instant of time.

In the Lagrangian picture we instead focus at some particular fluid particle located at position $\boldsymbol{r}_0$ at some time t_0. The Lagrangian field $g^\mathrm{L}(\boldsymbol{r}_0, t)$ then gives the property g of the exact same fluid particle as it moves through space. For small displacements around the position $\boldsymbol{r}_0$ we can describe the actual position of that fluid particle as $\boldsymbol{r}(t) = \boldsymbol{r}_0 + \boldsymbol{r}_1^\mathrm{L}(\boldsymbol{r}_0, t)$, where $\boldsymbol{r}_1^\mathrm{L}(\boldsymbol{r}_0, t)$ gives the displacement of *that* particle and is therefore a Lagrange field. This enables us to calculate the Eulerian field from the Lagrangian field since,

$$g^\mathrm{L}(\boldsymbol{r}_0, t) = g^\mathrm{E}(\boldsymbol{r}(t), t) \approx g^\mathrm{E}(\boldsymbol{r}_0, t) + \boldsymbol{r}_1^\mathrm{L}(\boldsymbol{r}_0, t)\cdot\boldsymbol{\nabla}g^\mathrm{E}(\boldsymbol{r}_0, t). \tag{2.23}$$

We have here expanded in $\boldsymbol{r}_1$. If we also expand g in Ma so $g = g_1 + g_2 \ldots$ we find

$$g_1^\mathrm{L} = g_1^\mathrm{E}, \tag{2.24a}$$

$$g_2^\mathrm{L} = g_2^\mathrm{E} + \left\langle \boldsymbol{r}_1^\mathrm{L}\cdot\boldsymbol{\nabla}g_1^\mathrm{E}\right\rangle, \tag{2.24b}$$

where we have kept our convention that subscript 2 is the time averaged second order field. In this thesis all fields will be Eulerian fields and in the following we will omit the superscript E. Only on Lagrangian fields we will explicitly write superscript L.

2.4.1 Particle velocity and boundary conditions on oscillating boundaries

We first define the time averaged particle velocity from the discussion above,

$$\boldsymbol{v}_2^{\mathrm{L}} = \boldsymbol{v}_2 + \langle \boldsymbol{r}_1 \cdot \boldsymbol{\nabla} \boldsymbol{v}_1 \rangle \qquad \text{time averaged particle velocity.} \tag{2.25}$$

Rather than just $\boldsymbol{v}_2$, this is the expression for the time averaged particle motion[1]. On a possibly moving boundary we then apply the assumption that fluid particles at the wall follow the wall position as it oscillates[16],

$$\boldsymbol{v}^{\mathrm{L}} = (\boldsymbol{v}^{\mathrm{s}})^{\mathrm{L}} \qquad \text{for particles with mean position } \boldsymbol{r} = \boldsymbol{r}_0^{\mathrm{s}}, \tag{2.26}$$

where superscript s will always refer to the surface. Since the solid surface can have no steady motion $(\boldsymbol{v}_2^{\mathrm{s}})^{\mathrm{L}} = \boldsymbol{0}$ we get the boundary condition on the *Eulerian* fields in each order,

$$\boldsymbol{v}_1 = \boldsymbol{v}_1^{\mathrm{s}} \qquad \text{at the wall mean level } \boldsymbol{r} = \boldsymbol{r}_0^{\mathrm{s}}, \tag{2.27a}$$

$$\boldsymbol{v}_2 + \langle \boldsymbol{r}_1 \cdot \boldsymbol{\nabla} \boldsymbol{v}_1 \rangle = \boldsymbol{0}. \qquad \text{at the wall mean level } \boldsymbol{r} = \boldsymbol{r}_0^{\mathrm{s}}. \tag{2.27b}$$

We call this the *particle-no-slip* boundary condition. Please note that we cannot simply substitute $\boldsymbol{v}_1 \to \boldsymbol{v}_1^{\mathrm{s}}$ in Eq. (2.27b) since $\boldsymbol{v}_1$ has a normal derivative whereas $\boldsymbol{v}_1^{\mathrm{s}}$ has not.

2.4.2 Conservation of mass to second order

Clearly, since the first order fields are harmonic there is mass conservation in every fixed volume over one period. The question is now if Eq. (2.27b) implies conservation of second order mass in a closed system. To investigate this we first consider the Eulerian mass flux which can be written as,

$$(\rho \boldsymbol{v})_2 = \rho_0 \boldsymbol{v}_2 + \langle \rho_1 \boldsymbol{v}_1 \rangle = \rho_0 \left(\boldsymbol{v}_2 + \langle \boldsymbol{r}_1 \boldsymbol{\nabla} \cdot \boldsymbol{v}_1 \rangle \right) \tag{2.28}$$

where we have used Eq. (2.9a) to rewrite ρ_1 and $\langle (\mathrm{i}A)B \rangle = -\langle A(\mathrm{i}B) \rangle$. In particular at the wall we can use Eq. (2.27b) to get the mass flux at the wall mean level $\boldsymbol{r} = \boldsymbol{r}_0^{\mathrm{s}}$,

$$(\rho \boldsymbol{v})_2 = \rho_0 \left(-\langle \boldsymbol{r}_1 \cdot \boldsymbol{\nabla} \boldsymbol{v}_1 \rangle + \langle \boldsymbol{r}_1 \boldsymbol{\nabla} \cdot \boldsymbol{v}_1 \rangle \right) \tag{2.29a}$$

$$= \frac{1}{2} \rho_0 \boldsymbol{\nabla} \times \langle \boldsymbol{r}_1 \times \boldsymbol{v}_1 \rangle \tag{2.29b}$$

where we have used the vector identity $\boldsymbol{\nabla} \times (\boldsymbol{A} \times \boldsymbol{B}) = \boldsymbol{A} \boldsymbol{\nabla} \cdot \boldsymbol{B} - \boldsymbol{B} \boldsymbol{\nabla} \cdot \boldsymbol{A} + \boldsymbol{B} \cdot \boldsymbol{\nabla} \boldsymbol{A} - \boldsymbol{A} \cdot \boldsymbol{\nabla} \boldsymbol{B}$. Please note that this is proportional to the curl of angular momentum density so there will only be *local* Eulerian mass flux at the wall mean level if the fluid undergoes rotational

motion here. We can examine the *global* conservation of mass by investigating the total mass flux Φ_{M} out of the system Ω, where $\boldsymbol{n}$ points towards the fluid,

$$\Phi_{\mathrm{M}} = \int_{\partial\Omega} (\rho \boldsymbol{v})_2 \cdot (-\boldsymbol{n}) \, \mathrm{d}A = -\frac{1}{2}\rho_0 \oint_{\partial\partial\Omega} \langle \boldsymbol{r}_1^{\mathrm{s}} \times \boldsymbol{v}_1^{\mathrm{s}} \rangle \cdot \, \mathrm{d}\boldsymbol{l}, \tag{2.30}$$

where we have used Stokes theorem to convert the surface integral over the surface $\partial\Omega$ to a line integral over the enclosing line $\partial\partial\Omega$. Please note that in the last expression we have replaced $\boldsymbol{v}_1 \to \boldsymbol{v}_1^{\mathrm{s}}$ from Eq. (2.27a). We see that for a closed surface with no boundary curve Φ_M vanishes trivially as we expect physically. Consequently the boundary condition Eq. (2.27) conserves mass in any *closed* system.

2.4.3 Fictitious pumping

We have seen from Eqs. (2.29) and (2.30) that we can have a *local* mass flux at the wall mean level but still conserve mass *globally*. The local mass flux into the system is best understood from Eq. (2.29a),

$$\boldsymbol{n} \cdot (\rho \boldsymbol{v})_2 = \rho_0 \left(- \langle \boldsymbol{r}_1^{\mathrm{s}} \cdot \boldsymbol{\nabla} [\boldsymbol{n} \cdot \boldsymbol{v}_1] \rangle + \langle [\boldsymbol{n} \cdot \boldsymbol{r}_1^{\mathrm{s}}] \boldsymbol{\nabla} \cdot \boldsymbol{v}_1 \rangle \right), \tag{2.31}$$

where we have assumed here that $\boldsymbol{n}$ is constant in space for simplicity. In Fig. 2.1 we

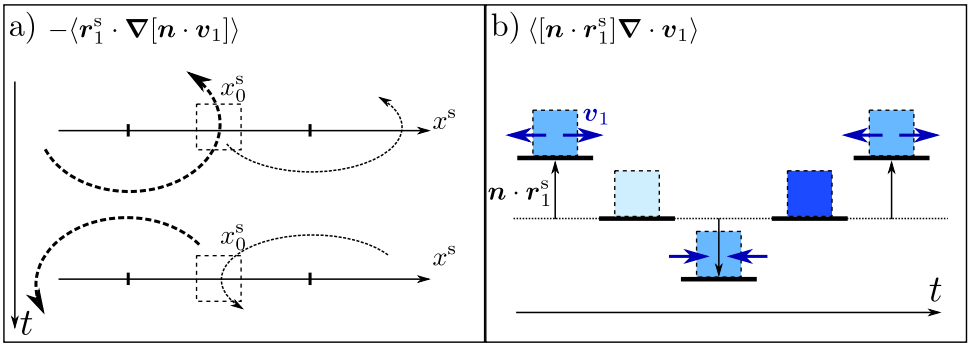

Figure 2.1: Sketch of acoustic pumping effects. a) shows the first term in Eq. (2.31) at the position x_0^{s} marked with the dashed square. The dashed arrows show the trajectories of the surface points which have mean position just next to x_0^{s}. The point to the left of x_0^{s} has a larger perpendicular velocity component than the point to the right. This situation will result in a net upward mass transportation. b) shows the second term in Eq. (2.31). If the velocity has positive divergence in the upper position and negative in the lower position, less dense fluid (light square) is transported downwards and more dense fluid (dark square) is transported upwards. This situation gives net upward mass flux.

show a sketch of the physical interpretation of each term in Eq. (2.31). The first term expresses that the *Eulerian* surface velocity at a point $\boldsymbol{r}_0^{\mathrm{s}}$ is actually the velocity of the surface point with mean position $\boldsymbol{r}_0^{\mathrm{s}} - \boldsymbol{r}_1^{\mathrm{s}}$ right next to $\boldsymbol{r}_0^{\mathrm{s}}$. In Fig. 2.1a) we show how this can lead to net upward mass flux. The second term in Eq. (2.31) expresses that if fluid is less dense when moving down and more dense when moving up, there can be a net mass

flux at some point $\boldsymbol{r}_0^{\mathrm{s}}$. This is shown in Fig. 2.1b) where mass is transported upwards. Please note that both situations imply circular fluid motion as predicted in Eq. (2.29b).

Finally we should emphasize that no mass is really penetrating the *physical wall*. We should just be aware that in the Eulerian fluid picture local mass penetration through the *mean* surface position is allowed.

Chapter 3

The finite element method and memory requirements

In this thesis we will develop effective models for both first order acoustics and second order streaming. These are developed in Chapters 5 and 6. From a numerical point of view the most important advantage of the effective models is that we do not have to resolve the large variations within the narrow acoustic boundary layer.

In this chapter we briefly introduce the finite element method (FEM) used to solve problems numerically through COMSOL. We then show a convergence test and establish the sufficient mesh size to use in the full and effective model respectively. Finally we test the memory consumption for the problems considered in this thesis in 2D and 3D and thus motivate effective modelling.

3.1 Introduction to the finite element method

The continuity and Navier-Stokes equation in Eq. (2.1) are both conservation equations of the form,

$$\boldsymbol{\nabla}\cdot\boldsymbol{J}[g(\boldsymbol{r})] = F, \tag{3.1}$$

where $\boldsymbol{J}$ is a generalized flux, F is a generalized force, and $g(\boldsymbol{r})$ is some generalized field variable we want to solve for. In the FEM we first construct a mesh of a finite number of elements usually triangular(see e.g.Fig. 3.2) or quad elements. At the n'th vertex we then define *basis* functions $\hat{g}_n$ which are by definition continuous and only non-zero at elements neighbouring vertex n. The idea in the FEM is then to approximate the solution $g(\boldsymbol{r})$ by a linear combination of these basis functions,

$$g(\boldsymbol{r}) \approx \sum_n C_n \hat{g}_n(\boldsymbol{r}) \tag{3.2}$$

where C_n are unknown constants to be found. Inserting this into Eq. (3.1) gives

$$\boldsymbol{\nabla}\cdot\boldsymbol{J}\left[\sum_n C_n \hat{g}_n(\boldsymbol{r})\right] - F = d(\boldsymbol{r}) \tag{3.3}$$

where $d(\boldsymbol{r})$ is the defect which is only zero if Eq. (3.2) is exactly satisfied. In the general *weak formulation* we then define test functions ϕ_m associated with vertex m and require that the projection of $d(\boldsymbol{r})$ on each test function vanishes. It turns out to be convenient to choose $\phi_m = \hat{g}_m$ so we have,

$$\int_\Omega \hat{g}_m \left\{ \boldsymbol{\nabla}\cdot\boldsymbol{J}\left[\sum_n C_n \hat{g}_n(\boldsymbol{r})\right] - F \right\} \mathrm{d}V = 0, \tag{3.4}$$

where Ω is the entire domain. For linear $\boldsymbol{J}$ we can use integration by parts and write this as,

$$\sum_n \left\{ \int_{\partial\Omega} \hat{g}_m \boldsymbol{J}[\hat{g}_n]\cdot\boldsymbol{n}\,\mathrm{d}A + \int_\Omega (-\boldsymbol{\nabla}\hat{g}_m)\cdot\boldsymbol{J}[\hat{g}_n]\,\mathrm{d}V \right\} C_n = \int_\Omega \hat{g}_m F\,\mathrm{d}V, \tag{3.5}$$

which forms the matrix problem $\sum_n K_{mn}C_n = F_m$, where K_{mn} is the stiffness matrix to be inverted to find the coefficients C_n. In the FEM software COMSOL we write in the integrands of this equations.

3.1.1 Boundary conditions in FEM

The most simple boundary condition to impose is the Neumann condition. Here we replace $\boldsymbol{J}\cdot\boldsymbol{n} = N(\boldsymbol{r})$ in Eq. (3.5). For any other general boundary condition written as $R(\boldsymbol{r}) = 0$ we introduce the auxiliary field λ with associated basis functions $\hat{\lambda}_m$ defined on elements neighbouring *boundary* vertexes only. In the first integrand in Eq. (3.5) we then replace

$$\hat{g}_m \boldsymbol{J}[\hat{g}_n]\cdot\boldsymbol{n} \quad \rightarrow \quad \hat{g}_m\lambda(\boldsymbol{r}) + \hat{\lambda}_m(\boldsymbol{r})R(\boldsymbol{r}). \tag{3.6}$$

With the introduction of the field λ we have increased the size of the matrix in Eq. (3.5) and since $\hat{\lambda}_m$ only appear in one term, that term must vanish leading to $R(\boldsymbol{r}) = 0$ as we wanted. Consequently we see that the solution λ gives us the actual flux $\lambda = \boldsymbol{J}\cdot\boldsymbol{n}$ resulting from $R = 0$.

3.2 Convergence test

For each model used in this thesis we have made a convergence test. This was done using the convergence parameter,

$$C(g) = \sqrt{\frac{\int (g - g_{\mathrm{ref}})^2\,\mathrm{d}A}{\int (g_{\mathrm{ref}})^2\,\mathrm{d}A}}, \tag{3.7}$$

where g is a general field and g_{ref} is a reference solution calculated on a very fine mesh. By decreasing the mesh size we then monitor the decrease of this parameter. This is shown in Fig. 3.1. For all effective models we used a homogeneous mesh with a mesh size $h_{\mathrm{bulk}} = (1/k_0)1/n_{\mathrm{mesh}}$ where n_{mesh} gives the spatial resolution. For the full model we choose the same in the bulk but at all walls we choose $h_{\mathrm{bl}} = (10\delta)/n_{\mathrm{mesh}}$. As reference mesh we then choose $n_{\mathrm{mesh}} = 30$. In Fig. 3.1 we have marked the line $C = 10^{-3}$ where

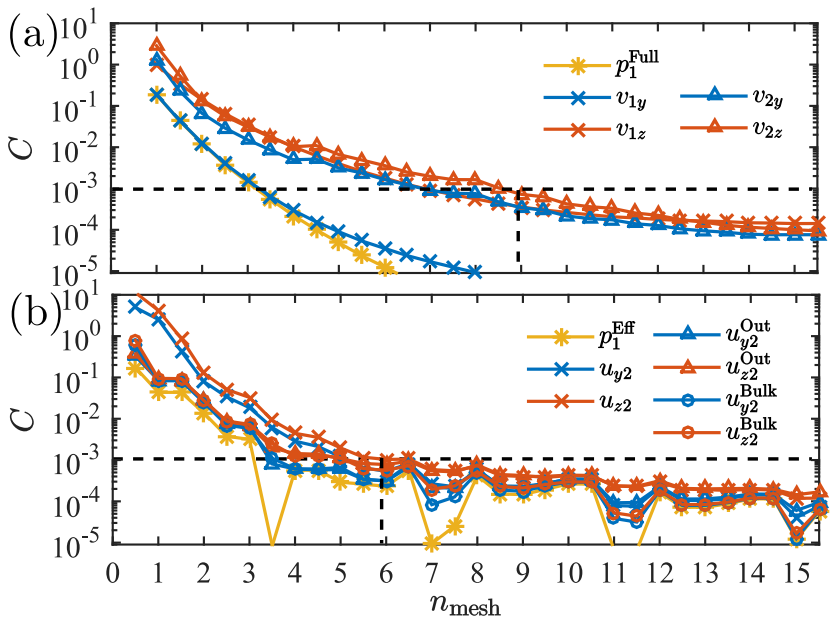

Figure 3.1: Convergence tests for each model used in this thesis performed on a $H \times W = 160 \times 380$ µm^2 channel as in Section 5.2. (a) Convergence for the full model with resolved boundary layers. (b) Convergence for the effective models developed in this thesis. p_1^{Eff} is the pressure calculated from the first order effective model explained in Chapter 5. The second order effective model is described in Chapter 6.

we accept the solution. We then show the accepted mesh in Fig. 3.2 for both the full and effective models. Please note the great advantage of not resolving the acoustic boundary layer. As the full model has different length scales it will need an inhomogeneous mesh which makes the meshing optimization very complicated and we do not claim that the mesh in Fig. 3.2(left) is the optimal one. The effective model on the other hand has only one length scale and we can use a simple homogeneous mesh as in Fig. 3.2(right).

3.3 Memory consumption for larger systems

We will now motivate the need for effective models by giving an idea of the memory consumptions needed to solve acoustic problems in larger systems of both 2D and 3D. We will give an estimate of the memory consumptions as a function of the number of degrees of freedom (DOF).

3.3.1 Discretization order and degrees of freedom

The integration in Eq. (3.5) involves the integration of the basis functions $\hat{g}_m$ associated with the vertex m. These basis functions are constructed by *shape* functions N_i defined on each element i neighbouring vertex m. We use Lagrangian shape functions which are polynomials of any order p and in the integration Eq. (3.5) these polynomials are easily

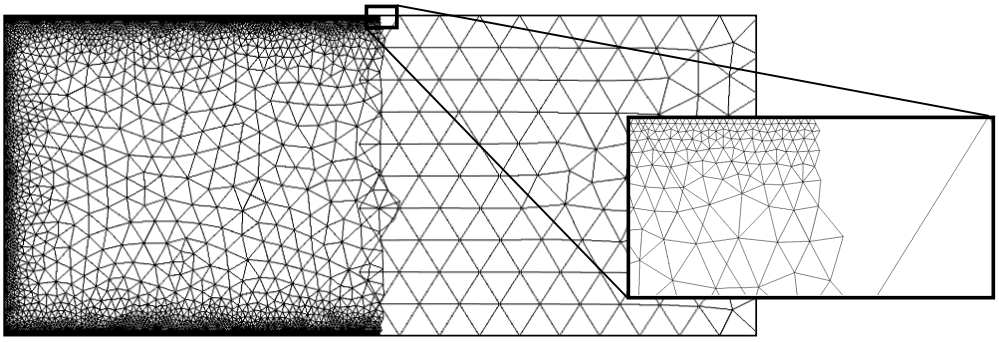

Figure 3.2: The mesh used for the full model (left) with and effective model (right) with $n_{\text{mesh}} = 9$ for the full model and $n_{\text{mesh}} = 6$ for the effective model as found from Fig. 3.1.

integrated by COMSOL. However, the order of these shape functions becomes important for the degrees of freedom DOF. A polynomial of degree p in N dimensions will in general have n_{pN} parameters, where

$$n_{pN} = \frac{(p+N)!}{p!N!}. \tag{3.8}$$

As an example a third order polynomial in two dimensions has $n_{32} = 10$ parameters: $a_1 + a_2x + a_3y + a_4x^2 + a_5y^2 + a_6xy + a_7x^3 + a_8y^3 + a_9x^2y + a_{10}xy^2$. These parameters are chosen by placing a sufficient number of nodes within each element and requiring the shape function to be zero at these nodes and unity at the mesh vertex m. As a rule of thump the total number of DOF then becomes[17],

$$\text{DOF} = \text{total number of nodes} \times \text{number of dependent variables}. \tag{3.9}$$

The exact number of nodes can be difficult to predict since neighbouring elements might share nodes but it is clear from Eq. (3.8) that the number of DOF will be strongly dependent on the order of the shape functions and the dimension of the problem.
In Table 3.1 we give an overview of the shape functions used in this thesis. In the full modelling of the Navier-Stokes equations we see that $\boldsymbol{\nabla v}$ enters in the stress tensor together with p. Therefore we must choose the shape functions for $\boldsymbol{v}$ one larger than those for p. In the effective first order model (introduced in Chapter 5) on the other hand we solve for p_1 and then calculate $\boldsymbol{u}_1 \propto \boldsymbol{\nabla} p_1$ so here the shape functions for p_1 must be one larger than we want for $\boldsymbol{u}_1$.

As an example with the mesh from Fig. 3.2 and shape functions of Table 3.1 both the first and second order full model required 626243 DOF. In contrast, the effective first order model (see Chapter 5) required 5036 DOF and all the effective second order models (see Chapter 6) required 8836 DOF.

3.3.2 Memory test

The exact memory required to solve problems can be very hard to predict. This is because it depends on the particular problem, the mesh structure, the order of the shape func-

Table 3.1: Overview of shape function order used in this thesis and in Fig. 3.3. The hierarchy between these orders must always be like in this table as described in the text.

2D	Effective	Full		3D	Effective	Full
5. order	p_1			4. order	p_1	
4. order	u_2	v_1,v_2		3. order	u_2	v_1,v_2
3. order	p_2	p_1,p_2		3. order	p_2	p_1,p_2

tions, the numeric solver *etc.* However since both the mesh and shape functions affect the DOF it turns out that DOF is a good fundamental parameter when comparing different models[17]. A reliable way to test the memory requirements for a particular problem is therefore to do a measurement as shown in Fig. 3.3. Here we have solved the problems investigated in this thesis i.e. the full model from Muller *et al.*[12] (Eq. (2.1)) and the effective model developed in this thesis (Eq. (5.1c) with Eq. (5.10) in first order and Eq. (6.15) in second order. For the values from Tables 2.1 and 3.1 we changed the DOF by decreasing the mesh size and plotted the required physical memory reported by COMSOL. For this measurement we used $h_{\text{bulk}} = (1/k_0)1/n_{\text{mesh}}$ and $h_{\text{bl}} = \delta/n_{\text{mesh}}$ (only for the full problem).

In Fig. 3.3 all the 2D graphs run from $n_{\text{Mesh}} = [1, 100]$. For the 3D graphs we first ran from $n_{\text{Mesh}} = [1, 6.5]$ for all models. Since the effective models only gave a memory consumption up to $10 - 15$ GB we then ran a second sweep from $n_{\text{Mesh}} = [6.5, 10]$ for the effective models (note the small discontinuity for the graphs 3D Eff p_1 and 3D Eff u_2, p_2). We see clearly that the 3D-calculations require much more memory per DOF. Further for both 2D and 3D we see that the DOF of the effective models do not increase as rapidly as for the full models as we increase n_{Mesh}. Since there are many parameters to play with in numerical optimization we do not claim that this is a fully developed proof of concept but the tendency from this analysis is that the effective model require much less memory than the full model - especially in 3D.

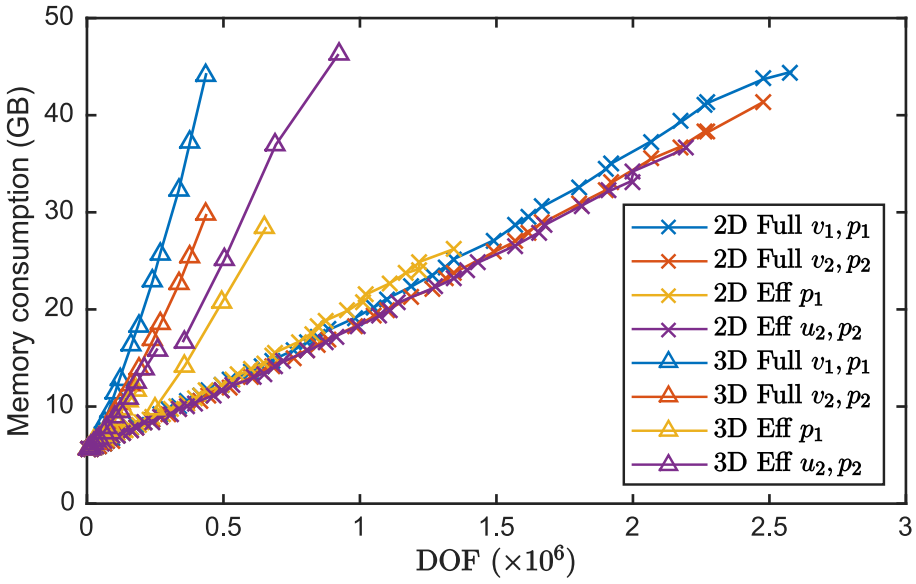

Figure 3.3: Plot of physical memory consumption reported by COMSOL as a function of degrees of freedom (DOF). We solved both 2D and 3D acoustic problem with the parameters in Table 2.1 in geometries of $380 \times 160\,\mu\text{m}^2$ and $380 \times 160 \times 160\,\mu\text{m}^3$ respectively both at resonance frequency $f = 1.96\,\text{MHz}$. We then increased DOF by increasing the parameter n_{Mesh} (see text). Only in the full model we used a mesh with fine boundary layers. We used COMSOL with the shape functions from Table 3.1 on a work station with 2.66 GHz quad core Intel(R) Xeon(R) CPU and 48 GB RAM. The graphs 3D Eff p_1 (yellow triangles) and 3D Eff u_2, p_2 (purple triangles) were collected in two steps coursing the small discontinuity on these graphs.

Chapter 4

Geometry of curved surfaces and model assumptions

The first important step in the analysis of streaming near curved surfaces is to understand the curvilinear geometry. Nyborg formulated his limiting velocity theory in a simple tangential coordinate system ignoring the differential of the basis vectors. This was later adjusted by Lee and Junjun[10] who implemented the theory in general global coordinates and applied it in e.g. spherical coordinates. It is however not always convenient neither possible to work in one single global curvilinear coordinate system.

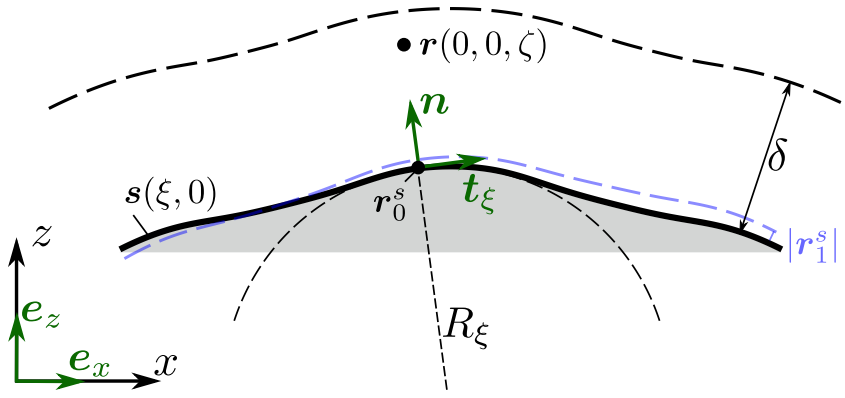

Figure 4.1: 2D sketch of the surface geometry. The surface segment close to the surface point $\boldsymbol{r}_0^{\mathrm{s}}$ is described by $\boldsymbol{s}(\xi,\eta)$ parametrized by arclength ξ,η. We show the $\eta = 0$ plane so the bold black line is the line of curvature $\boldsymbol{s}(\xi,0)$ passing through $\boldsymbol{r}_0^{\mathrm{s}}$. We have sketched the boundary layer length δ and the wall oscillation amplitude $|\boldsymbol{r}_1^{\mathrm{s}}|$. Please note that for illustrational purpose we have drawn the radius of curvature $R_\xi \approx \delta$ which is not allowed in our model.

The approach in this thesis will be to formulate the limiting velocity theory in a *local* coordinate system near any point $\boldsymbol{r}_0^{\mathrm{s}}$ on the surface. We will only need the curvilinear derivatives at that point so there is no need to formulate global coordinates. Computa-

tionally we will then always work in a background Cartesian coordinate system (x, y, z) (see Fig. 4.1) and then apply the following approach,

1) Calculate results in the background Cartesian coordinate system (x, y, z)

2) At each point $\boldsymbol{r}_0^{\mathrm{s}}$ transform the result from (x, y, z) to the local curvilinear coordinate system (ξ, η, ζ)

3) Do calculations in the curvilinear coordinates

4) At the point $\boldsymbol{r}_0^{\mathrm{s}}$ transform the curvilinear results back from (ξ, η, ζ) to (x, y, z).

The technical details and the implementation of this procedure in COMSOL is explained in Chapter D. To understand the range of validity of our model we first introduce the local basis at each point $\boldsymbol{r}_0^{\mathrm{s}}$.

4.1 Local basis for curves embedded in a surface

Consider the small surface segment $\boldsymbol{s}(\xi, \eta)$ where $\boldsymbol{s}(0, 0) = \boldsymbol{r}_0^{\mathrm{s}}$ as drawn in Fig. 4.1. The lines $\boldsymbol{s}(\xi, 0)$ and $\boldsymbol{s}(0, \eta)$ are chosen to be principal lines of curvature parametrized by arc length ξ, η. The orthogonal tangent vectors at $\boldsymbol{r}_0^{\mathrm{s}}$ are then defined as,

$$\boldsymbol{t}_\xi \equiv \partial_\xi \boldsymbol{s}, \qquad \boldsymbol{t}_\eta \equiv \partial_\eta \boldsymbol{s}, \qquad \text{at } \boldsymbol{r} = \boldsymbol{r}_0^{\mathrm{s}}. \tag{4.1}$$

Furthermore since lines of curvature share their normal vector with the surface normal vector $\boldsymbol{n}$ we have by definition[18],

$$\partial_\xi \boldsymbol{t}_\xi = \kappa_\xi \boldsymbol{n}, \qquad \partial_\eta \boldsymbol{t}_\eta = \kappa_\eta \boldsymbol{n}, \qquad \text{at } \boldsymbol{r} = \boldsymbol{r}_0^{\mathrm{s}}, \tag{4.2}$$

where κ_ξ, κ_η are the curvatures of $\boldsymbol{s}(\xi, 0)$ and $\boldsymbol{s}(0, \eta)$ respectively. We choose the parametrization such that $\boldsymbol{t}_\xi, \boldsymbol{t}_\eta, \boldsymbol{n}$ form a local right handed basis,

$$\boldsymbol{t}_\xi \times \boldsymbol{t}_\eta = \boldsymbol{n}. \tag{4.3}$$

Along with the tangential coordinates ξ, η we also define the perpendicular coordinate ζ. Any point $\boldsymbol{r}$ close to $\boldsymbol{r}_0^{\mathrm{s}}$ is then (see Fig. 4.1),

$$\boldsymbol{r} = \boldsymbol{s}(\xi, \eta) + \zeta \boldsymbol{n}(\xi, \eta) \qquad \text{for } \boldsymbol{r} \approx \boldsymbol{r}_0^{\mathrm{s}}. \tag{4.4}$$

Please note that we are only interested in the *derivatives* at $\boldsymbol{r}_0^{\mathrm{s}}$ so this description suffices. To find these derivatives we first note that since $\boldsymbol{n}$ is a unit vector,

$$\boldsymbol{n} \cdot (\partial_\xi \boldsymbol{n}) = \frac{1}{2} \partial_\xi (\boldsymbol{n} \cdot \boldsymbol{n}) = \frac{1}{2} \partial_\xi (1) = 0, \tag{4.5}$$

so $\boldsymbol{n}$ is perpendicular to both $\partial_\xi \boldsymbol{n}$ and $\partial_\eta \boldsymbol{n}$. Now, since $\boldsymbol{t}_\eta = \boldsymbol{n} \times \boldsymbol{t}_\xi$ we have,

$$\partial_\xi \boldsymbol{t}_\eta = \partial_\xi \boldsymbol{n} \times \boldsymbol{t}_\xi + \boldsymbol{n} \times \partial_\xi \boldsymbol{t}_\xi = \partial_\xi \boldsymbol{n} \times \boldsymbol{t}_\xi, \tag{4.6}$$

but both $\partial_\xi \boldsymbol{n}$ and $\boldsymbol{t}_\xi$ are perpendicular to $\boldsymbol{n}$ so $\partial_\xi \boldsymbol{t}_\eta$ must be parallel with $\boldsymbol{n}$,

$$\partial_\xi \boldsymbol{t}_\eta = \tau_\eta \boldsymbol{n}, \tag{4.7}$$

where we have defined the torsion τ_ξ of the curve $\boldsymbol{s}(0,\eta)$. We see that this torsion gives the change of $\boldsymbol{t}_\eta$ along $\boldsymbol{n}$ (rotation) when increasing ξ,

$$\tau_\eta = \boldsymbol{n} \cdot (\partial_\xi \boldsymbol{t}_\eta). \tag{4.8}$$

The derivative of $\boldsymbol{n}$ is now straight forward,

$$\partial_\xi \boldsymbol{n} = \partial_\xi \boldsymbol{t}_\xi \times \boldsymbol{t}_\eta + \boldsymbol{t}_\xi \times \partial_\xi \boldsymbol{t}_\eta = (\kappa_\xi \boldsymbol{n}) \times \boldsymbol{t}_\eta + \boldsymbol{t}_\xi \times (\tau_\xi \boldsymbol{n}) = -\kappa_\xi \boldsymbol{t}_\xi - \tau_\eta \boldsymbol{t}_\eta. \tag{4.9}$$

Following the same approach for $\partial_\eta \boldsymbol{t}_\xi$ and $\partial_\eta \boldsymbol{n}$ we find,

$$\begin{bmatrix} \partial_\xi \boldsymbol{t}_\xi \\ \partial_\xi \boldsymbol{n} \\ \partial_\xi \boldsymbol{t}_\eta \end{bmatrix} = \begin{bmatrix} 0 & \kappa_\xi & 0 \\ -\kappa_\xi & 0 & -\tau_\xi \\ 0 & \tau_\xi & 0 \end{bmatrix} \begin{bmatrix} \boldsymbol{t}_\xi \\ \boldsymbol{n} \\ \boldsymbol{t}_\eta \end{bmatrix}, \qquad \begin{bmatrix} \partial_\eta \boldsymbol{t}_\eta \\ \partial_\eta \boldsymbol{n} \\ \partial_\eta \boldsymbol{t}_\xi \end{bmatrix} = \begin{bmatrix} 0 & \kappa_\eta & 0 \\ -\kappa_\eta & 0 & -\tau_\eta \\ 0 & \tau_\eta & 0 \end{bmatrix} \begin{bmatrix} \boldsymbol{t}_\eta \\ \boldsymbol{n} \\ \boldsymbol{t}_\xi \end{bmatrix}. \tag{4.10}$$

This is the general Frenet-Serret frame apparatus for curves on a surface sharing the normal vector with the surface[18]. We will now establish the goal of accuracy and make some assumptions on the relation between the length scales of the system.

4.2 Physical length scales

In this thesis we will restrict our selves to surfaces where the principal lines of curvature (at least locally) have zero torsion, $\tau_\xi = \tau_\eta = 0$. This is the case for all two dimensional objects as well as most of the shapes used in micro-fluids including straight channels of any cross section, closed rectangular or cylindrical containers with closed ends[19] or spheres[13] (see Chapter 7). The theory can easily be extended but leads to unnecessary complexity here.

Introducing the radii of curvature $R_\xi = 1/\kappa_\xi$, $R_\eta = 1/\kappa_\eta$ as well as the length scales $l_{\kappa_\xi}, l_{\kappa_\eta}$ over which κ_ξ and κ_η changes, we can now give an overview over the length scales in the system,

$$\begin{aligned} R &\equiv \min\{R_\xi, R_\eta\} && \text{Surface variations,} \\ l_\kappa &\equiv \min\{L_{\kappa_\xi}, L_{\kappa_\eta}\} && \text{Curvature variations,} \\ l &\equiv \min\{R, 1/k_0\} && \text{Acoustic field variations close to the surface,} \\ \delta &= \sqrt{2\nu_0/\omega} && \text{Viscous boundary layer length scale,} \\ |\boldsymbol{r}_1^{\mathrm{s}}| & && \text{Amplitude of wall oscillations.} \end{aligned} \tag{4.11}$$

We will assume that the wall oscillation amplitude $|\boldsymbol{r}_1^{\mathrm{s}}|$ is always much smaller than the viscous boundary layer length scale δ. Further, we assume all other length scales to be much larger than δ,

$$|\boldsymbol{r}_1^{\mathrm{s}}| \ll \delta \ll l, l_\kappa. \tag{4.12}$$

We then introduce the important smallness parameter,

$$\varepsilon \equiv \delta/l, \tag{4.13}$$

which we will extensively refer to in the rest of the thesis. It expresses the fraction between the shear variation length scale and the compressional variation length scale. In particular we have from Chapter 2 that $(k_0\delta) \sim \varepsilon$ and $\Gamma \sim \varepsilon^2$. The goal in the following is now to define geometric quantities to first order in ε within the boundary layer region i.e. $0 < \zeta \lesssim 5\delta$.

4.3 Geometric quantities and mathematical operators in curvilinear coordinates

We first define the scaling factors h_i as the change in position per change in i-coordinate,

$$h_i \equiv |\partial_i \boldsymbol{r}| \,. \tag{4.14}$$

From Eqs. (4.1), (4.4) and (4.10) with $\tau_\xi = \tau_\eta = 0$ we find,

$$h_\xi = 1 - \zeta\kappa_\xi, \tag{4.15a}$$
$$h_\eta = 1 - \zeta\kappa_\eta, \tag{4.15b}$$
$$h_\zeta = 1. \tag{4.15c}$$

We see that these are only dependent on ζ to first order in ε. An important geometric quantity is then,

$$\mathcal{H} = \frac{\partial(h_\xi h_\eta)}{(h_\xi h_\eta)\partial\zeta} = -\kappa_\xi - \kappa_\eta - \zeta(\kappa_\xi^2 + \kappa_\eta^2) + \mathcal{O}(\varepsilon^2), \tag{4.16}$$

which is twice the negative mean curvature.

For later reference we here give some differential operators in the local curvilinear basis. We shall only evaluate these exactly at the surface $\zeta = 0$, so we shall use $h_\xi = h_\eta = h_\zeta = 1$ and $\mathcal{H} = -\kappa_\xi - \kappa_\eta$. For more detailed calculations please consult the appendix Chapter A. The gradient is

$$\boldsymbol{\nabla} f \approx \boldsymbol{\nabla}_\parallel f + \boldsymbol{n}\partial_\zeta f, \tag{4.17}$$

where $\boldsymbol{\nabla}_\parallel \equiv \boldsymbol{t}_\xi\partial_\xi + \boldsymbol{t}_\eta\partial_\eta$ is the parallel gradient. The divergence is,

$$\boldsymbol{\nabla}\cdot\boldsymbol{A} \approx \boldsymbol{\nabla}_\parallel\cdot\boldsymbol{A}_\parallel + \frac{\partial A_\zeta}{\partial\zeta} + \mathcal{H}A_\zeta \tag{4.18}$$

where $\boldsymbol{\nabla}_\parallel\cdot\boldsymbol{A}_\parallel \equiv \partial_\xi A_\xi + \partial_\eta A_\eta$ is the parallel divergence. The laplacian is $\boldsymbol{\nabla}\cdot(\boldsymbol{\nabla} f)$,

$$\nabla^2 f \approx \nabla_\parallel^2 f + \partial_\zeta^2 f + \mathcal{H}\partial_\zeta f, \tag{4.19}$$

where $\nabla_\parallel^2 \equiv \partial_\xi^2 + \partial_\eta^2$ is the parallel laplacian. Finally we give the convective derivative $\boldsymbol{A} \cdot \boldsymbol{\nabla} \boldsymbol{B}$ in its parallel components,

$$(\boldsymbol{A} \cdot \boldsymbol{\nabla} \boldsymbol{B})_\parallel \approx \boldsymbol{A}_\parallel \cdot \boldsymbol{\nabla}_\parallel \boldsymbol{B}_\parallel + A_\zeta \frac{\partial \boldsymbol{B}_\parallel}{\partial \zeta} - A_\zeta \boldsymbol{Q}_B \tag{4.20}$$

where $\boldsymbol{Q}_B \equiv (\kappa_\xi B_\xi, \kappa_\eta B_\eta)$ and perpendicular components,

$$(\boldsymbol{A} \cdot \boldsymbol{\nabla} \boldsymbol{B})_\zeta \approx \boldsymbol{A}_\parallel \cdot \boldsymbol{\nabla}_\parallel B_\zeta + A_\zeta \frac{\partial B_\zeta}{\partial \zeta} + \boldsymbol{A}_\parallel \cdot \boldsymbol{Q}_B. \tag{4.21}$$

We mention that the quantity $\boldsymbol{Q}_B$ was ignored in the work by Nyborg[1] but taken into account by Lee *et al.*[10] in more general coordinates.

Chapter 5

Effective modelling of acoustic fields near a solid surface

Having established the governing equations in Chapter 2 and the surface geometry in Chapter 4 we are now ready to formulate the effective model of first order acoustics near a solid surface. Together with Chapter 6 this chapter is where we present the main work of this thesis.

In this section we derive an analytic expression for the acoustic velocity field within the boundary layer region. The expression will be valid to lowest order in ε (see Eq. (4.13)) which become $\mathcal{O}(\varepsilon^0)$ for the parallel fields and $\mathcal{O}(\varepsilon^1)$ for the perpendicular fields. The key is to use that the shear-part $\boldsymbol{w}_1$ of the velocity $\boldsymbol{v}_1$ has much larger variations in the perpendicular direction than in the parallel direction. The derivation reveals a condition on p_1 at the boundary to ensure $\boldsymbol{v}_1 = \boldsymbol{v}^{\mathrm{s}}$ at the surface. This boundary condition is one of the main results of this thesis and as we show in an example it reveals some important physical effects from the boundary layer which can not be obtained from the usual approach $\partial_\zeta p_1 = 0$ on stationary walls.

5.1 The velocity field within the boundary layer region

As described in Section 2.3 the first order velocity $\boldsymbol{v}_1$ can be decomposed into a compressional field $\boldsymbol{u}_1$ and a shear field $\boldsymbol{w}_1$. We here summarize the field equations we need to solve to first order in the Ma-number,

$$\boldsymbol{v}_1 = \boldsymbol{u}_1 + \boldsymbol{w}_1, \qquad \text{where} \qquad \boldsymbol{\nabla} \times \boldsymbol{u}_1 = \boldsymbol{0}, \qquad \nabla^2 \boldsymbol{u}_1 + k_{\mathrm{c}}^2 \boldsymbol{u}_1 = 0, \tag{5.1a}$$

$$\boldsymbol{\nabla} \cdot \boldsymbol{w}_1 = 0, \qquad \nabla^2 \boldsymbol{w}_1 + k_{\mathrm{s}}^2 \boldsymbol{w}_1 = 0, \tag{5.1b}$$

$$\boldsymbol{u}_1 = \frac{(1 - \mathrm{i}\Gamma)}{\mathrm{i}\omega\rho_0} \boldsymbol{\nabla} p_1, \qquad \nabla^2 p_1 + k_{\mathrm{c}}^2 p_1 = 0. \tag{5.1c}$$

where $k_{\mathrm{c}} = k_0(1 + \mathrm{i}\Gamma/2)$ and $k_{\mathrm{s}} = (1 + \mathrm{i})/\delta$. We show the qualitative behaviour of $\boldsymbol{v}_1$, $\boldsymbol{u}_1$ and $\boldsymbol{w}_1$ in Fig. 5.1.

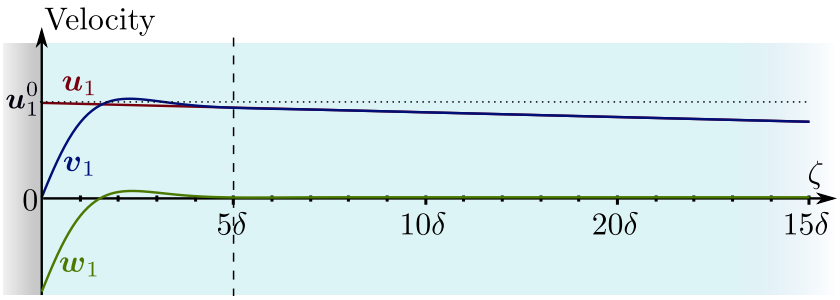

Figure 5.1: The qualitative behaviour of the three velocity fields $\boldsymbol{u}_1$, $\boldsymbol{w}_1$ and their sum $\boldsymbol{v}_1 = \boldsymbol{u}_1 + \boldsymbol{w}_1$ near a solid boundary (here stationary). Note the small variations in $\boldsymbol{u}_1$ along the normal coordinate ζ compared to $\boldsymbol{w}_1$. The extend of the boundary layer region is around $0 < \zeta \lesssim 5\delta$.

In Eq. (2.27a) we have explained the boundary condition on the full first order velocity field $\boldsymbol{v}_1$ also restated below. Further we will assume that the shear field $\boldsymbol{w}_1$ is confined to the wall so we have,

$$\boldsymbol{v}_1 = \boldsymbol{u}_1 + \boldsymbol{w}_1 = \boldsymbol{v}_1^{\mathrm{s}} \qquad \text{at the surface mean level } \zeta = 0, \tag{5.2a}$$

$$\boldsymbol{w}_1 \to 0 \qquad \text{away from the surface} \quad \zeta \to \infty, \tag{5.2b}$$

where $\boldsymbol{v}_1^{\mathrm{s}}$ is the surface velocity.

First we solve for $\boldsymbol{w}_1$ in Eq. (5.1b). Please recall that $\boldsymbol{w}_1$ expresses the momentum diffusion which will be large close to the wall. The parallel variations will be over the length scale $1/k_0$ whereas the the perpendicular variations will be over δ. Consequently the curvilinear Laplacian from Eq. (4.19) can be written as

$$\nabla^2 \boldsymbol{w}_1 = \partial_\zeta^2 \boldsymbol{w}_1 + \mathcal{O}(\varepsilon). \tag{5.3}$$

In this approximation $\boldsymbol{w}_1$ has a decaying solution of the form $\boldsymbol{w}_1 = \boldsymbol{A}\mathrm{e}^{\mathrm{i}k_{\mathrm{s}}\zeta}$ and imposing Eq. (5.2a) we have for the *parallel* component,

$$\boldsymbol{w}_{1\parallel} = -(\boldsymbol{u}_{1\parallel}^0 - \boldsymbol{v}_{1\parallel}^{\mathrm{s}})\mathrm{e}^{\mathrm{i}k_{\mathrm{s}}\zeta}, \tag{5.4}$$

where superscript 0 on $\boldsymbol{u}_{1\parallel}^0 \equiv \boldsymbol{u}_{1\parallel}(\xi, \eta, 0)$ means evaluated at $\zeta = 0$. We then choose $w_{1\zeta}$ to ensure continuity $\boldsymbol{\nabla}\cdot\boldsymbol{w}_1 = 0$. From Eq. (4.18) we see that within the same approximation as Eq. (5.3) this gives,

$$\partial_\zeta w_{1\zeta} = -\boldsymbol{\nabla}_\parallel \cdot \boldsymbol{w}_{1\parallel} = \boldsymbol{\nabla}_\parallel \cdot (\boldsymbol{u}_{1\parallel}^0 - \boldsymbol{v}_{1\parallel}^{\mathrm{s}})\mathrm{e}^{\mathrm{i}k_{\mathrm{s}}\zeta} \quad \Rightarrow \quad w_{1\zeta} = \boldsymbol{\nabla}_\parallel \cdot \left[\boldsymbol{u}_{1\parallel}^0 - \boldsymbol{v}_{1\parallel}^{\mathrm{s}}\right] \frac{\mathrm{e}^{\mathrm{i}k_{\mathrm{s}}\zeta}}{\mathrm{i}k_{\mathrm{s}}}, \tag{5.5}$$

which indeed also solves Eq. (5.1b) to sufficient accuracy. We now have $\boldsymbol{w}_1$ and we have satisfied the parallel boundary condition of Eq. (5.2a). To fulfil the perpendicular version of Eq. (5.2a) we then need to claim on $u_{1\zeta}$,

$$u_{1\zeta}^0 = v_{1\zeta}^{\mathrm{s}} - w_{1\zeta}^0 = v_{1\zeta}^{\mathrm{s}} - \frac{1}{\mathrm{i}k_{\mathrm{s}}} \boldsymbol{\nabla}_\parallel \cdot \left[\boldsymbol{u}_{1\parallel}^0 - \boldsymbol{v}_{1\parallel}^{\mathrm{s}}\right] \qquad \text{at } \zeta = 0. \tag{5.6}$$

Finally to finish our fields we see from Eq. (5.6) that $u^0_{1\zeta}$ is $\mathcal{O}(\varepsilon)$ if $v^{\mathrm{s}}_1 = 0$. In that case we cannot ignore the slow variations in $u_{1\zeta}$ so we write within the boundary layer region,

$$u_{1\zeta} \approx u^0_{1\zeta} + \zeta \partial_\zeta u^0_{1\zeta}. \tag{5.7}$$

In conclusion the fields are,

$$\boldsymbol{u}_{1\parallel} = \boldsymbol{u}^0_{1\parallel}, \tag{5.8a}$$

$$\boldsymbol{w}_{1\parallel} = -(\boldsymbol{u}^0_{1\parallel} - \boldsymbol{v}^{\mathrm{s}}_{1\parallel})\mathrm{e}^{\mathrm{i}k_{\mathrm{s}}\zeta}, \tag{5.8b}$$

$$u_{1\zeta} = v^{\mathrm{s}}_{1\zeta} - \frac{1}{\mathrm{i}k_{\mathrm{s}}}\boldsymbol{\nabla}_\parallel \cdot \left[\boldsymbol{u}^0_{1\parallel} - \boldsymbol{v}^{\mathrm{s}}_{1\parallel}\right] + \zeta \partial_\zeta u^0_{1\zeta}, \tag{5.8c}$$

$$w_{1\zeta} = \frac{\mathrm{e}^{\mathrm{i}k_{\mathrm{s}}\zeta}}{\mathrm{i}k_{\mathrm{s}}}\boldsymbol{\nabla}_\parallel \cdot \left[\boldsymbol{u}^0_{1\parallel} - \boldsymbol{v}^{\mathrm{s}}_{1\parallel}\right]. \tag{5.8d}$$

And for completeness and later reference we write the total field $\boldsymbol{v}_1 = \boldsymbol{u}_1 + \boldsymbol{w}_1$,

$$\boldsymbol{v}_{1\parallel} = \boldsymbol{v}^{\mathrm{s}}_{1\parallel}\mathrm{e}^{\mathrm{i}k_{\mathrm{s}}\zeta} + \boldsymbol{u}^0_{1\parallel}\left(1 - \mathrm{e}^{\mathrm{i}k_{\mathrm{s}}\zeta}\right) \tag{5.9a}$$

$$v_{1\zeta} = v^{\mathrm{s}}_{1\zeta} + \zeta \partial_\zeta u^0_{1\zeta} - \frac{1}{\mathrm{i}k_{\mathrm{s}}}\boldsymbol{\nabla}_\parallel \cdot \left[\boldsymbol{u}^0_{1\parallel} - \boldsymbol{v}^{\mathrm{s}}_{1\parallel}\right]\left(1 - \mathrm{e}^{\mathrm{i}k_{\mathrm{s}}\zeta}\right). \tag{5.9b}$$

Eqs. (5.8) and (5.9) are the velocity fields valid close to a solid boundary and they are sketched in Fig. 5.1 for $\boldsymbol{v}^{\mathrm{s}}_1 = \boldsymbol{0}$. Please notice that we have here derived the total field just from knowing $\boldsymbol{u}^0_{1\parallel}$ which is to be found from the pressure.

5.1.1 New boundary condition on p_1

From the analysis above we can now easily deduce a boundary condition on p_1 to ensure Eq. (5.6). Using Eq. (5.1c) we find,

$$\boxed{\partial_\zeta p_1 = \mathrm{i}\omega\rho_0\left[v^{\mathrm{s}}_{1\zeta} - \frac{\mathrm{i}}{k_{\mathrm{s}}}\boldsymbol{\nabla}_\parallel \cdot \boldsymbol{v}^{\mathrm{s}}_1\right] - \frac{\mathrm{i}}{k_{\mathrm{s}}}\left(\partial^2_\zeta p_1 + k^2_c p_1\right) \qquad \text{at } \zeta = 0}, \tag{5.10}$$

This is the boundary condition to apply on p_1 to take into account the $\mathcal{O}(\varepsilon)$-effects from the acoustic boundary layer as we will see. To lowest order in ε we can use $|p_1| \sim \rho_0 c_0 |\boldsymbol{u}_1|$ and write this boundary condition in the two common cases: (i) a perpendicular surface velocity with small parallel fluid velocity and (ii) a stationary surface,

$$\text{(i)} \qquad \left|v^{\mathrm{s}}_{1\zeta}\right| \gg \varepsilon\left|\boldsymbol{u}_{1\parallel}\right|, \varepsilon\left|\boldsymbol{v}^{\mathrm{s}}_{1\parallel}\right| \qquad \Rightarrow \qquad \partial_\zeta p_1 = \mathrm{i}\omega\rho_0 v^{\mathrm{s}}_{1\zeta}, \tag{5.11a}$$

$$\text{(ii)} \qquad \boldsymbol{v}^{\mathrm{s}}_1 = \boldsymbol{0} \qquad \Rightarrow \qquad \partial_\zeta p_1 = -\frac{\mathrm{i}}{k_{\mathrm{s}}}\left(\partial^2_\zeta p_1 + k^2_c p_1\right). \tag{5.11b}$$

Whereas case (i) is the well known boundary condition presented in common teaching books (e.g. Bruus[14] or Landau and Lifshitz[20]), case (ii) is to the extend of our knowledge not used before. It arise since it is not only the compressional velocity $u_{1\zeta}$ that must vanish at the surface but the *total* velocity $u_{1\zeta} + w_{1\zeta}$ and to have continuity $\boldsymbol{\nabla}\cdot\boldsymbol{w}_1 = 0$,

$w_{1\zeta}$ is not necessarily zero.

To find the fluid velocity in the bulk $\boldsymbol{u}_1$ we can now solve Eq. (5.1c) and use Eq. (5.10) to get the effects from the boundary layer *without* resolving the large variations numerically. In the following we will therefore refer to Eqs. (5.1c) and (5.10) as the *effective model* to calculate the first order fields.

We will now investigate this boundary condition by applying it to a simple well-understood set-up, namely the rectangular channel studied numerically by Muller *et al.*[12] and in full analytical detail (with boundary layers) by Karlsen[21]. From a comparison with the full model by Muller we show that we approximate the correct resonant properties i.e., resonance frequency and Q-factor which is in contrast to the simple approach $\partial_z p_1 = 0$ on stationary walls.

5.2 Example: Rectangular 2-dimensional channel

Consider the x-invariant channel in the domain $y \in [-W/2, W/2]$ and $z \in [-H/2, H/2]$, where W is the total width and H is total height. The side walls are then oscillated symmetrically as sketched in Fig. 5.2 and the top/bottom walls are stationary. We now

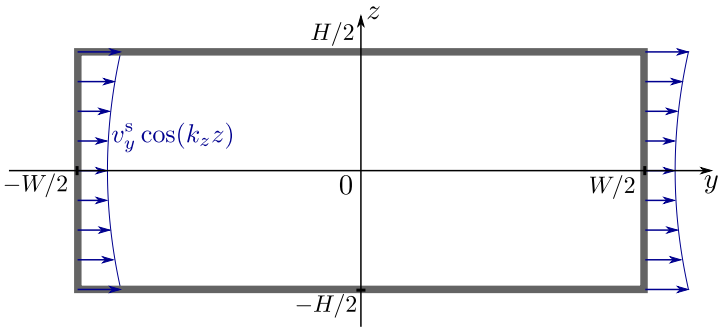

Figure 5.2: Sketch of rectangular channel set-up. Note that k_z is here complex.

solve for the pressure in this channel and then calculate $\boldsymbol{u}_1$ from Eq. (5.1c). We will assume small parallel velocity at the side walls at $y = \pm W/2$ so we can use the simplified boundary conditions Eq. (5.11). To be clear we therefore solve,

$$\nabla^2 p_1 + k_c^2 p_1 = 0 \tag{5.12a}$$

$$\mp \partial_y p_1 = \mp \mathrm{i}\omega\rho_0 [v_{1y}^{\mathrm{s}} G(z)] \qquad \text{at} \quad y = \pm W/2 \tag{5.12b}$$

$$\mp \partial_z p_1 = -\frac{\mathrm{i}}{k_{\mathrm{s}}} (\partial_z^2 p_1 + k_c^2 p_1) \qquad \text{at} \quad z = \pm H/2. \tag{5.12c}$$

$$\boldsymbol{u}_1 = \frac{1}{\mathrm{i}\omega\rho_0} \boldsymbol{\nabla} p_1 \tag{5.12d}$$

where $G(z)$ is the surface velocity profile and v_{1y}^{s} is a constant. Using separation of variables gives,

$$p_1 = Y(y)Z(z) \qquad Y'' = -k_y^2 Y, \qquad Z'' = -k_z^2 Z, \qquad k_c^2 = k_y^2 + k_z^2. \tag{5.13}$$

From Eq. (5.12b) we see that $\partial_y p_1(W/2) = \partial_y p_1(-W/2)$ so p_1 must be antisymmetric in y. Further if we choose $G(z)$ to be symmetric in z, p_1 must be symmetric in z suggesting the ansatz,

$$Y(y) = A_y \sin(k_y y), \tag{5.14a}$$
$$Z(z) = \cos(k_z z). \tag{5.14b}$$

At the stationary bottom wall $z = -H/2$ the boundary condition in Eq. (5.12c) separates completely to a boundary condition on $Z(z)$. From insertion of Eq. (5.14b) we get,

$$k_z \sin\left(k_z \frac{H}{2}\right) = \frac{1}{\mathrm{i}k_{\mathrm{s}}}\left(-k_z^2 + k_c^2\right)\cos\left(k_z \frac{H}{2}\right), \tag{5.15}$$

which gives the condition for k_z,

$$k_c^2 = k_z^2 + \mathrm{i}k_s k_z \tan\left(k_z \frac{H}{2}\right). \tag{5.16}$$

At the oscillating wall at $y = -W/2$ we find using Eq. (5.12b),

$$A_y k_y \cos\left(k_y \frac{W}{2}\right)\cos(k_z z) = \mathrm{i}\omega\rho_0 v_y^{\mathrm{s}} G(z) \tag{5.17}$$

We now choose the simplest case where the wall velocity profile is $G(z) = \cos(k_z z)$ as shown in Fig. 5.2 (where k_z is complex). We note that this give a finite velocity at $z = \pm H/2$. However, this is only the $\boldsymbol{u}_1$-part of the velocity so we do not violate the no slip condition at these walls. The field solutions then become,

$$p_1(y,z) = \frac{\mathrm{i}\omega\rho_0 v_y^{\mathrm{s}}}{k_y}\frac{\sin(k_y y)}{\cos\left(k_y \frac{W}{2}\right)}\cos(k_z z), \tag{5.18a}$$

$$u_{1y}(y,z) = v_y^{\mathrm{s}}\frac{\cos(k_y y)}{\cos\left(k_y \frac{W}{2}\right)}\cos(k_z z), \tag{5.18b}$$

$$u_{1z}(y,z) = -v_y^{\mathrm{s}}\frac{k_z}{k_y}\frac{\sin(k_y y)}{\cos\left(k_y \frac{W}{2}\right)}\sin(k_z z). \tag{5.18c}$$

Approximate solution at the fundamental resonance We now find an approximate solution for k_y and k_z by solving Eq. (5.16) for k_z. Assuming $k_0\delta \ll 1$ we have $|k_{\mathrm{s}}| \gg |k_z|$ and the solutions to Eq. (5.16) is found when $\tan(k_z H/2)$ is small, i.e., around $|k_z| \approx 2n\pi/H$. We search for the lowest mode where $|k_z| \approx 0$ and $|k_y| \approx \pi/W$. We can then expand the tangent in Eq. (5.16) and solve for k_z^2 and then k_y^2,

$$k_y^2 \approx k_0^2\left(1 + (1+\mathrm{i})\frac{\delta}{H}\right), \qquad k_z^2 \approx -k_0^2(1+\mathrm{i})\frac{\delta}{H}, \tag{5.19}$$

where we have used that $k_c = k_0 + \mathcal{O}(\varepsilon^2) \approx k_0$. We see here that the ratio δ/H now becomes the important parameter. The wavelength in the y-direction is then $\lambda_y = 2\pi/\mathrm{Re}\{k_y\}$ or,

$$\lambda_y = \frac{c_0}{f}\left(1 - \frac{1}{2}\frac{\delta}{H}\right). \tag{5.20}$$

We see that the y-wavelength in a system with boundary layers is a bit smaller than c_0/f as one would get without boundary layers. Resonance is found by minimizing the denominators of the fields in Eq. (5.18). Since $\mathrm{Im}\{k_y\}$ is small we have resonance when $\mathrm{Re}\{k_y\} = \pi/W$ or in terms of frequency $f = k_0 c_0/2\pi$,

$$\boxed{f^{\mathrm{Res}} = \frac{c_0}{2W}\left(1 - \frac{1}{2}\frac{\delta}{H}\right) \quad \text{Resonance frequency}}. \tag{5.21}$$

Please note that this is actually an implicit equation since δ depends on the frequency, $\delta = \sqrt{2\nu_0/\omega^{\mathrm{Res}}}$. This will however be a second order contribution in δ/H and we can use $\delta \approx \sqrt{2\nu_0/(2\pi c_0/(2W))}$ in this calculation. We see that this resonance is slightly lower than $c_0/(2W)$ as one would get without boundary layers. Using Eq. (5.20) we see that at resonance we have indeed have $\lambda_y = 2W$. We can now write up the fields Eq. (5.18) at this fundamental resonance with $\mathrm{Re}\{k_y\} = \pi/W$ giving $k_y^{\mathrm{Res}} = \frac{\pi}{W}\left(1 + \mathrm{i}\frac{1}{2}\frac{\delta}{H}\right)$ and $k_z^{\mathrm{Res}} \approx \mathrm{i}\frac{\pi}{W}\sqrt{1+\mathrm{i}}\sqrt{\frac{\delta}{H}}$. We expand to first order in $\frac{\delta}{H}$ to get,

$$p_1^{\mathrm{Res}}(y,z) = \frac{\mathrm{i}\omega\rho_0 v_y^{\mathrm{s}}}{\pi/W}\left[\mathrm{i}\frac{\sin\left(\frac{\pi y}{W}\right)}{\frac{\pi}{4}\frac{\delta}{H}} - \frac{y}{W/2}\cos\left(\frac{\pi y}{W}\right)\right]\left[1 + \frac{\delta}{H}\frac{(1+\mathrm{i})}{2}\left(\frac{\pi z}{W}\right)^2\right], \tag{5.22a}$$

$$u_{1y}^{\mathrm{Res}}(y,z) = v_y^{\mathrm{s}}\left[\mathrm{i}\frac{\cos\left(\frac{\pi y}{W}\right)}{\frac{\pi}{4}\frac{\delta}{H}} + \frac{y}{W/2}\sin\left(\frac{\pi y}{W}\right)\right]\left[1 + \frac{\delta}{H}\frac{(1+\mathrm{i})}{2}\left(\frac{\pi z}{W}\right)^2\right], \tag{5.22b}$$

$$u_{1z}^{\mathrm{Res}}(y,z) = v_y^{\mathrm{s}}\frac{\delta}{H}\left[\mathrm{i}\frac{\sin\left(\frac{\pi y}{W}\right)}{\frac{\pi}{4}\frac{\delta}{H}} - \frac{y}{W/2}\cos\left(\frac{\pi y}{W}\right)\right](1+\mathrm{i})\left(\frac{\pi z}{W}\right). \tag{5.22c}$$

Please note that we have used $k_z z \ll 1$, valid for channels with $H \ll W^2/\delta$. Consider e.g. a small channel of $W = 200$ µm with water $\delta \approx 0.4$ µm, giving $H \ll 1$ m which is usually satisfied.

From these equations we see that at resonance u_{1y}^{Res} is around (H/δ) larger than the wall velocity and actually $u_{1\zeta}^{\mathrm{Res}}$ has the same magnitude as the wall velocity. We also see that all the resonant parts (first terms in square brackets) has a phase factor of i exactly at resonance. Please also note that u_{1z}^{Res} do not vanish at the walls at $z = \pm H/2$ which is normally assumed[14, 20]. In fact $u_{1z}^{\mathrm{Res}}(y, H/2)$ increases with (H/W) at the these walls as long $H \ll W^2/\delta$ as mentioned above.

Comparison with full model We show the resonance solution in Fig. 5.3 together with a simulation of the full Navier-Stokes-problem Eq. (2.1) solved in a similar way as

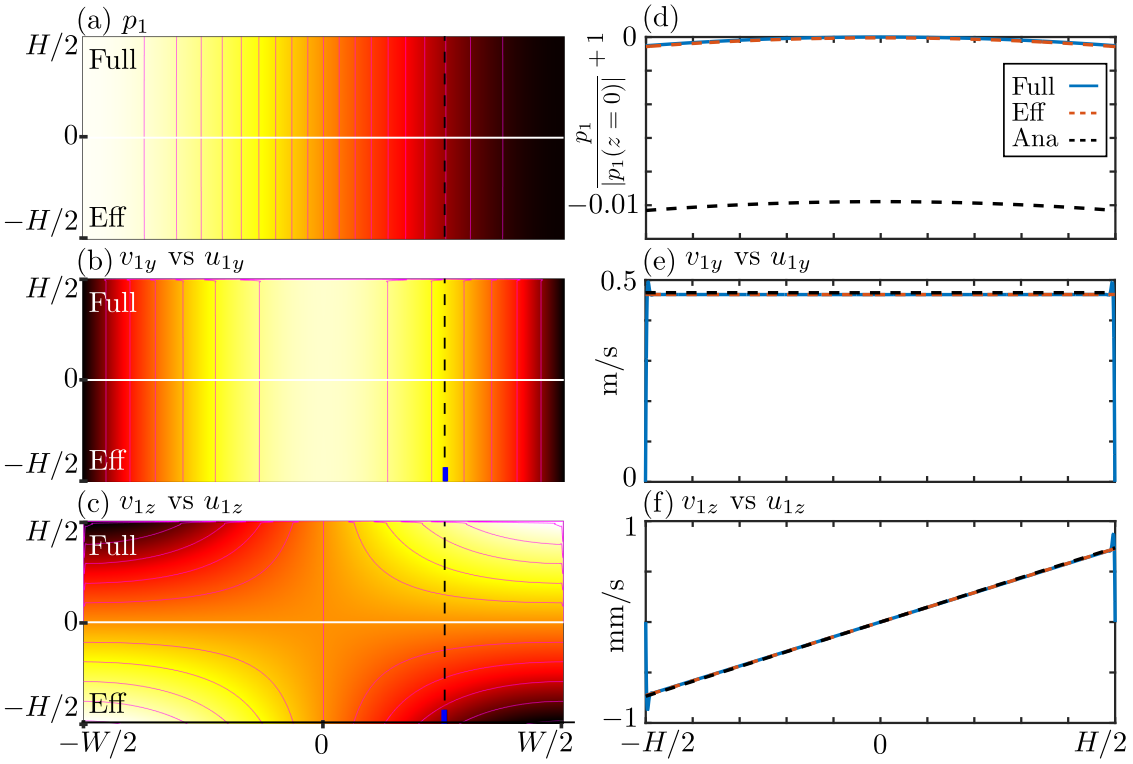

Figure 5.3: Plot of the first order fields in a rectangular channel of dimensions $H = 160\,\mu\text{m}$ and $W = 380\,\mu\text{m}$ with the parameters of Table 2.1 and $f = f^{\text{Res}} = 1.967\,\text{MHz}$. The color plots (a)-(c) compare the full model (upper part) with the effective model (lower part). (a) p_1 from -1 to $1\,\text{MPa}$ (black-white). Contour separation is $0.1\,\text{MPa}$. (b) v_{1y} and u_{1y} from $0 - 0.5\,\text{m}\,\text{s}^{-1}$ (black-white). Contour separation is $0.1\,\text{m}\,\text{s}^{-1}$. (c) v_{1z} and u_{1z} from -1 to $1\,\text{mm}\,\text{s}^{-1}$ (black-white). Contour separation is $0.2\,\text{mm}\,\text{s}^{-1}$. (d)-(f) show a line plot of the fields along the vertical dashed line $y = W/4$ drawn in (a)-(c) respectively.

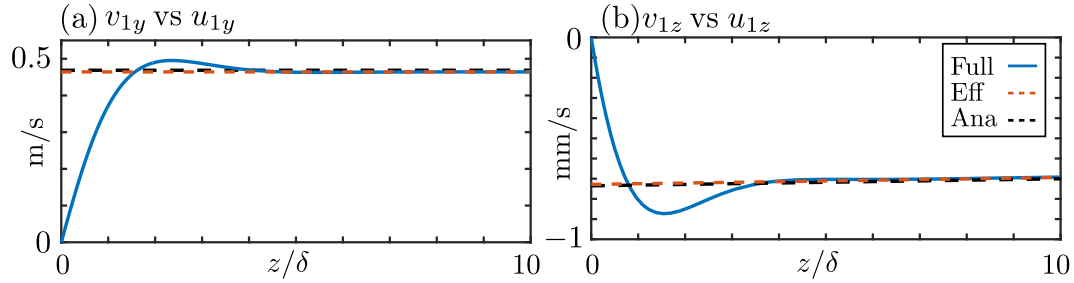

Figure 5.4: The velocity field plotted close to the lower boundary at $y = W/4$ as shown with blue line in Fig. 5.3(b-c). Please note that the effective model (orange) is slightly closer to the full model (blue) than the analytic model of Eq. (5.22) (dashed black) is.

Muller *et al.*[12]. We also plot the result from the effective model presented in this chapter i.e. Eqs. (5.1c) and (5.10). We have chosen a channel of dimensions $H = 160\,\mu\text{m}$ and $W = 380\,\mu\text{m}$ which has been studied in full numerical detail by Muller *et al.*[12] and we found the resonance frequency at $f^{\text{Res}} = 1.967\,\text{MHz}$ in agreement with Eq. (5.21). Further, we used the actuation velocity of $v_{1y}^{\text{s}} = d_1\omega^{\text{Res}} \approx 1.2\,\text{mm}\,\text{s}^{-1}$ where $d_1 = 0.1$ nm is displacement amplitude. Note first how the contours fit in Fig. 5.3(a-c). In Fig. 5.3(d) we have plotted relative variations in pressure across the channel where we see that the effective model caches the parabolic behaviour. However, the analytical solution is wrong by a factor of 10^{-2}. Please recall that Eq. (5.22) is an approximation to first order in $(k_0\delta) \sim 3 \times 10^{-3}$ and $\delta/H \sim 2 \times 10^{-3}$. In the effective model on the other hand we have kept the full $k_{\text{c}} = k_0(1 + \text{i}\Gamma/2)$, so we expect this model to fit better with the full simulation. In Fig. 5.3(e-f) we have the same discrepancy for u_{1y} and u_{1z} although not as obvious as in Fig. 5.3(d).

In Fig. 5.4 we have zoomed in on the boundary layer region where we see how the effective model do not resolve the boundary layer variations as expected. We also note that $|v_{1z}| \,/\, |v_{1y}| \sim 10^{-3} \sim \varepsilon$ as expected.

We have here seen that the fields Eq. (5.22) approximates the full resonant solution to the expected accuracy. With these analytic result we will in the following section analyse the damping and quality factor of this resonator and again compare with a full model to show that we approximate the right resonant properties.

5.2.1 Effective damping and Q-factor

For any harmonically oscillating system we have that the acoustic energy density stored in the system is twice the time average of the kinetic energy density. The perpendicular energy becomes negligible in this calculation and we can calculate the space averaged energy density E_{ac} from Eq. (5.18b) using $k_z \ll k_y$,

$$E_{\text{ac}} = 2\frac{1}{W}\int_{-W/2}^{W/2}\frac{1}{2}\rho_0\left(\frac{1}{2}\left|u_{1y}\right|\right)\,\text{d}y = \frac{\rho_0(v_y^{\text{s}})^2}{2W}\int_{-W/2}^{W/2}\frac{\left|\cos(k_y y)\right|^2}{\left|\cos(k_y\frac{W}{2})\right|^2}\,\text{d}y, \tag{5.23}$$

where we have used that $\left\langle u_{1y}^2\right\rangle = \frac{1}{2}\left|u_{1y}\right|^2$. We now evaluate this integral around resonance $k_y \approx k_y^{\text{Res}} \equiv \frac{\pi}{W}\left(1 + \text{i}\frac{1}{2}\frac{\delta}{H}\right)$ writing

$$k_y = k_y^{\text{Res}} + \frac{\omega - \omega^{\text{Res}}}{c_0} \tag{5.24}$$

where $(\omega - \omega^{\text{Res}})/c_0 \ll k_y^{\text{Res}}$ and ω^{Res} is given in Eq. (5.21). We then expand Eq. (5.23) in δ/H and $(\omega - \omega^{\text{Res}})/c_0$ and integrate. The after some straight forward integration we find,

$$E_{\text{ac}} \approx \frac{\rho_0(v_y^{\text{s}})^2}{\pi^2}\frac{\left(\omega^{\text{Res}}\right)^2}{(\omega - \omega^{\text{Res}})^2 + \left(\omega^{\text{Res}}\right)^2\left(\Gamma^{\text{BL}}\right)^2} \quad \text{for } \omega \approx \omega^{\text{Res}} \tag{5.25}$$

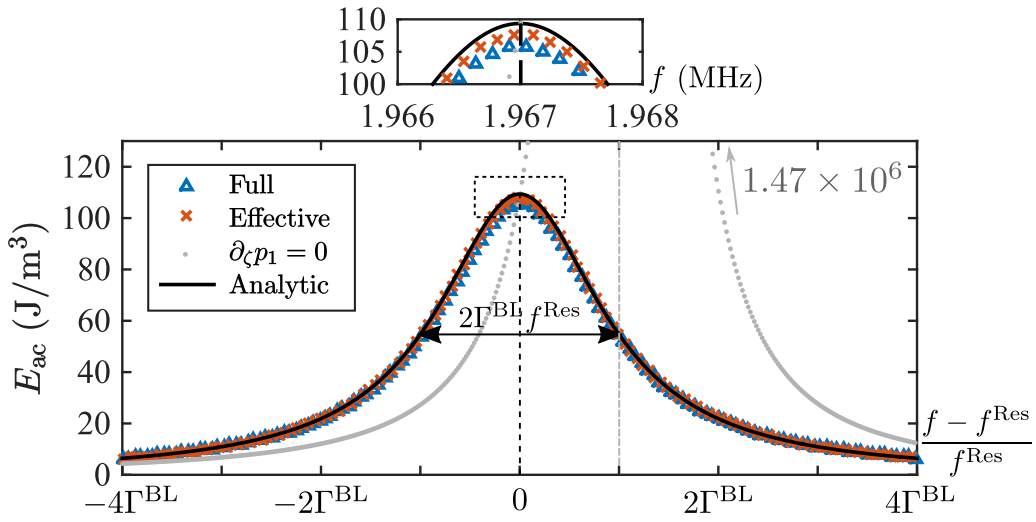

Figure 5.5: Lorentz curve for the rectangular channel with $f^{\mathrm{Res}} = 1.967\,\mathrm{MHz}$ and damping $\Gamma^{\mathrm{Res}} = 0.0012$. The analytic result is from Eq. (5.25). The insert shows a zoom at the maximum of the Lorentz curve and the gray dots show the energy stored in the system for the simple approach $\partial_\zeta p_1 = 0$ on stationary walls which gives $E_{\mathrm{ac}}^{\mathrm{max}} = 1.47 \times 10^6\,\mathrm{J\,m^{-3}}$.

where we have defined the damping factor due to the acoustic boundary layers,

$$\Gamma^{\mathrm{BL}} \equiv \frac{1}{2}\frac{\delta}{H}. \tag{5.26}$$

We show this Lorentzian line shape in Fig. 5.5 together with the full model, the effective model, as well as the result from a simple approach using $\partial_\zeta p_1 = 0$ on stationary walls. The curves fit well within an error of 10^{-2} as for the curves in Fig. 5.3(d-f). The main difference between the analytic model and effective model is that the effective model takes bulk damping $\Gamma \sim \varepsilon^2$ into account. From Eq. (5.25) we find the maximum energy stored in the system at $\omega = \omega^{\mathrm{Res}}$,

$$E_{\mathrm{ac}}^{\mathrm{Res}} \approx \frac{\rho_0 (v_y^{\mathrm{s}})^2}{\pi^2} \frac{1}{(\Gamma^{\mathrm{BL}})^2}, \tag{5.27}$$

which scales with $(H/\delta)^2$. The full width at half maximum of this lineshape is found to be $\Delta\omega = 2\omega^{\mathrm{Res}}\Gamma^{\mathrm{BL}}$ and the Q-factor Q of this resonator become simply,

$$Q \equiv \frac{\omega^{\mathrm{Res}}}{\Delta\omega^{\mathrm{Res}}} = \frac{\omega^{\mathrm{Res}}}{2\Gamma^{\mathrm{BL}}\omega^{\mathrm{Res}}} = \frac{1}{2\Gamma^{\mathrm{BL}}} = \frac{H}{\delta}. \tag{5.28}$$

Please note in Fig. 5.5 that the simple approach $\partial_\zeta p_1 = 0$ (gray dots) gives a huge resonance energy with maximum shifted $f^{\mathrm{Res}}\Gamma^{\mathrm{BL}}$ away from the new approach.

5.3 Fluid interaction with the exterior

As we have seen we can get many interesting properties out of the oscillating system only by solving for p_1 with the right boundary condition Eq. (5.10). In this section we will

briefly go through energy dissipation and stress at the boundary walls for a more general system.

5.3.1 Energy dissipated in a general system

The spatial average of the dissipated energy density per cycle $\frac{2\pi}{\omega}$ in a system of volume V is found from integrating the power-density $(\boldsymbol{\nabla}\cdot\boldsymbol{\sigma})\cdot\boldsymbol{v}$,

$$E_{\text{dis}} = \frac{1}{V}\int_\Omega \frac{2\pi}{\omega}\left\langle(\boldsymbol{\nabla}\cdot\boldsymbol{\sigma})\cdot\boldsymbol{v}\right\rangle \,\mathrm{d}V. \tag{5.29}$$

At resonance the dominating term will be from the boundary layers $\langle(\boldsymbol{\nabla}\cdot\boldsymbol{\sigma})\cdot\boldsymbol{v}\rangle \approx \eta_0\left\langle(\partial_\zeta^2\boldsymbol{v}_{1\parallel})\cdot\boldsymbol{v}_{1\parallel}\right\rangle$. Since we have the ζ dependence of $\boldsymbol{v}_{1\parallel}$ from Eq. (5.9a) we can integrate over the boundary layer and be left with a surface integral. After some straight forward integration we then get,

$$E_{\text{dis}} \approx \frac{1}{V}\frac{2\pi}{\omega}\eta_0\int_{\partial\Omega}\int_0^\infty \left\langle(\partial_\zeta^2\boldsymbol{v}_{1\parallel})\cdot\boldsymbol{v}_{1\parallel}\right\rangle \mathrm{d}\zeta\ \mathrm{d}A \tag{5.30a}$$

$$= \pi\frac{\delta}{V}\int_{\partial\Omega}\frac{1}{2}\rho_0\left|\boldsymbol{u}_{1\parallel}^0\right|^2\ \mathrm{d}A, \qquad \text{at resonance} \tag{5.30b}$$

where we have used that $\boldsymbol{u}_{1\parallel}^0 \sim Q\boldsymbol{v}_{1\parallel}^{\text{s}} \gg \boldsymbol{v}_{1\parallel}^{\text{s}}$ at resonance. We see that the energy dissipated is simply proportional to the parallel kinetic energy of the compressional field close to the wall. Now turning back to the resonant rectangular set-up we have the resonant solution in Eq. (5.22) we find from the two boundary layers at $\zeta = \pm H/2$,

$$E_{\text{dis}} = 2\pi\frac{\delta}{HW}\frac{1}{2}\rho_0\int_{-W/2}^{W/2}\left(\frac{v_{1y}^{\text{s}}\cos\left(\frac{\pi y}{W}\right)}{\frac{\pi}{4}\frac{\delta}{H}}\right)^2\ \mathrm{d}y = \frac{8}{\pi}(v_{1y}^{\text{s}})^2\rho_0\frac{H}{\delta} \tag{5.31}$$

So we can calculate the Q-factor as,

$$Q = 2\pi\frac{\text{Energy stored in the system at resonance}}{\text{Energy lost per cycle}} = 2\pi\frac{E_{\text{ac}}^{\text{Res}}HW}{E_{\text{dis}}HW} = \frac{H}{\delta}, \tag{5.32}$$

in agreement with Eq. (5.28). This is probably the best way to understand the factor δ/H: Since energy is stored over the length H and dissipated over the length δ the Q-factor must scale with H/δ.

5.3.2 Stress on a solid wall

As a next step we can now model the damped pressure and velocity field inside a micro channel where we also model the elastic motion of the solid. This is beyond the scope of thesis but we will briefly present the strategy here.

The well known fluid-solid coupling is that the velocity of the fluid is set to the velocity of the solid, which we have already imposed in Eq. (5.2a). The boundary condition on the solid is to apply continuity in the stress on the interface,

$$\boldsymbol{n} \cdot \boldsymbol{\sigma}_1 = \boldsymbol{n} \cdot \boldsymbol{\sigma}_1^{\mathrm{s}}, \tag{5.33}$$

where $\boldsymbol{\sigma}_1$ is the first order version of Eq. (2.2) and the structure of the solid stress tensor $\boldsymbol{\sigma}^{\mathrm{s}}$ is irrelevant for this discussion. Please note that we keep our convention where $\boldsymbol{n}$ points towards the fluid. The point is now that we can get $\boldsymbol{n} \cdot \boldsymbol{\sigma}_1$ by using the first order solutions Eq. (5.9). After some manipulations we get,

$$\boldsymbol{n} \cdot \boldsymbol{\sigma}_1 = -p_1 \boldsymbol{n} - \mathrm{i} k_{\mathrm{s}} \eta_0 \left(\left[\frac{1}{\mathrm{i}\omega\rho_0} \boldsymbol{\nabla}_{\parallel} p_1 \right] - \boldsymbol{v}_{1\parallel}^{\mathrm{s}} \right) \tag{5.34}$$

where we have used $\boldsymbol{\nabla} \cdot \boldsymbol{u}_1 = \mathrm{i}\omega p_1/(\rho_0 c_0^2)$ and neglected terms of $\mathcal{O}(\varepsilon^2)$. Please note that we can now calculate the total stress including sheer on the wall only by calculating the pressure i.e., solving one *scalar* equation in the fluid.

5.4 Concluding remarks on effective modelling of acoustic fields and outlook

We have in this chapter derived a boundary condition on the pressure and we have shown in an example how this boundary condition gives the right resonant properties of an oscillating system. In modelling of pressure acoustics in 3D systems it is much more efficient to solve for p_1 satisfying a simple Helmholtz equation instead of solving the full Navier-Stokes problem with boundary layers and four fields. The usual approach of an effective modelling[11, 22–24] of the first order velocity is to use $\partial_\zeta p_1 = 0$ on stationary walls which gives a much larger resonance energy as we saw in Fig. 5.5. If we want to calculate e.g. the dynamics of suspended particles, both the radiation force[25] and the second order streaming velocity (as in Chapter 6) involve terms which are quadratic in p_1 (or $|\boldsymbol{u}_1|$) and the damping of p_1 therefore becomes crucial. Eq. (5.10) thus provides an important contribution to the field of pressure acoustics.

Further we have in this chapter provided an analytic expression for the velocity fields valid within the boundary layer region given in Eqs. (5.8) and (5.9). The behaviour of these fields determine the second order streaming velocity as we will see in the next chapter.

Chapter 6

Acoustic streaming and limiting velocity theory

So far we have in Chapter 4 established how we do calculations within the boundary layer region of a curved surface. In Chapter 5 we formulated an effective model for calculation of the first order acoustic fields and in particular we provided a general analytic expression for the fields within the boundary layer. In this chapter we proceed in the same way by searching for an effective model for the second order streaming velocity. The outset is the limiting velocity theory developed by Nyborg[1] and later Lee *et al.*[10] but we will here extend the limiting velocity theory to allow curved surfaces of *any* surface velocity (as long the amplitude $|\boldsymbol{r}_1^{\mathrm{s}}| \ll \delta$). Both Nyborg and Lee had an implicit implementation of the no-particle slip boundary condition $\boldsymbol{v}_2 + \langle \boldsymbol{r}_1 \cdot \boldsymbol{\nabla} \boldsymbol{v}_1 \rangle = \boldsymbol{0}$ of Eq. (2.27b) which we will here impose more rigorously in a similar way as Vanneste *et al.*[11] did for a flat surface. Inspired by Vanneste *et al.* we will develop a decomposition of the streaming field into three fields as described in Chapter 1: Inner streaming, outer streaming and bulk steaming. Finally we end this chapter by explaining a special kind of bulk streaming which has a length scale comparable with a half wavelength.

6.1 Solution strategy and decomposition

The time averaged second order continuity and Navier-Stokes equations are explained in Chapter 2 and restated here for convenience,

$$0 = \boldsymbol{\nabla} \cdot (\rho_0 \boldsymbol{v}_2 + \langle \rho_1 \boldsymbol{v}_1 \rangle) \tag{6.1a}$$

$$\boldsymbol{0} = -\boldsymbol{\nabla} p_2 + \eta_0 \nabla^2 \boldsymbol{v}_2 + \eta_0 \beta \boldsymbol{\nabla} (\boldsymbol{\nabla} \cdot \boldsymbol{v}_2) - \langle \boldsymbol{\nabla} \cdot ((\rho_0 \boldsymbol{v}_1) \boldsymbol{v}_1) \rangle \,. \tag{6.1b}$$

Please note that the time derivatives have been averaged out and therefore these equations describe a *steady* problem for the time averaged fields $\boldsymbol{v}_2$ and p_2. Physically Eq. (6.1) can be very difficult to get an intuition about. First, Eq. (6.1a) states that the second order Eulerian mass current density $\rho_0 \boldsymbol{v}_2 + \langle \rho_1 \boldsymbol{v}_1 \rangle$ is divergence free i.e.no mass can leave or enter any point. But we have already solved for some of this mass current $\langle \rho_1 \boldsymbol{v}_1 \rangle$ in Chapter 5

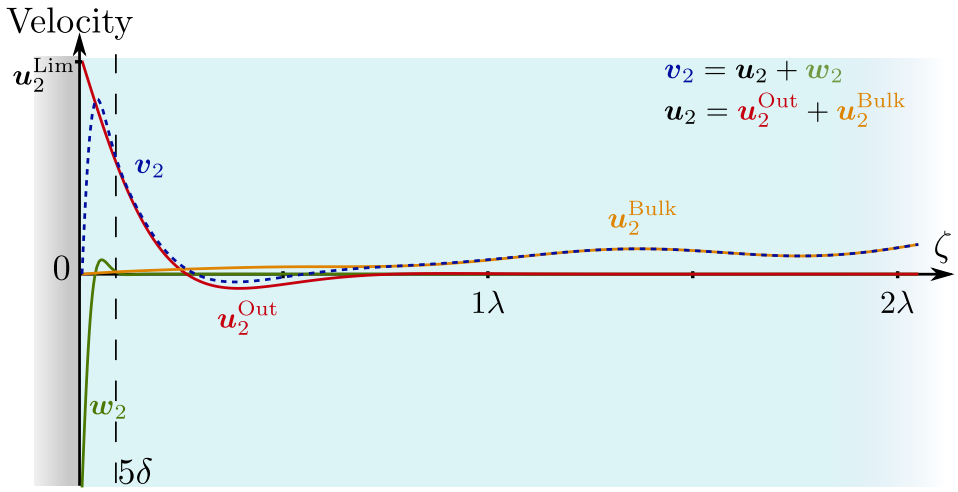

Figure 6.1: Sketch (not to scale) of second order streaming velocities near a boundary. Close to the boundary layer the inner streaming $\boldsymbol{w}_2$ changes rapidly, decays after $\zeta \approx 5\delta$ and is finite at the surface. This is what gives the limiting velocity $\boldsymbol{u}_2^{\mathrm{Lim}}$ as a boundary condition on the outer streaming $\boldsymbol{u}_2^{\mathrm{Out}}$ which decays approximately after one acoustic wavelength λ. The only possible streaming in the bulk is $\boldsymbol{u}_2^{\mathrm{Bulk}}$. The full streaming field is then the sum $\boldsymbol{v}_2 = \boldsymbol{u}_2^{\mathrm{Out}} + \boldsymbol{u}_2^{\mathrm{Bulk}} + \boldsymbol{w}_2$.

and if that happens to converge to some point then $\rho_0 \boldsymbol{v}_2$ *must* diverge away from that point to ensure continuity. Therefore the flow $\rho_0 \boldsymbol{v}_2$ might seem to have have mass sinks and sources and is not so physical in itself. The same is the case in Eq. (6.1b): If there happens to be a convergence of momentum current density to a point $-\langle \boldsymbol{\nabla} \cdot ((\rho_0 \boldsymbol{v}_1)\boldsymbol{v}_1) \rangle$ then $\boldsymbol{v}_2$ and p_2 must be such that the total second order momentum is conserved. Please note p_2 now only acts as a Lagrangian multiplier to be chosen to conserve mass and momentum in any point. One of the goals of this chapter is to reformulate Eq. (6.1) in a much simpler and intuitive way by using scaling and decompositions.

Whereas the first order fields were successfully Helmholtz decomposed into the long-range compressional field $\boldsymbol{u}_1$ and short-range shear field $\boldsymbol{w}_1$, the Helmholtz decomposition is now not so obvious. Instead we will here search a decomposition only based on the physical origin of each field. Please note that Eq. (6.1) has non-linear products of first order fields but is *linear* in $\boldsymbol{v}_2$ and p_2. Therefore we can write these field as a sum of fields each satisfying different parts of the problem. In Fig. 6.1 we have sketched the behaviour of all the the velocity fields we will consider in the following. We first give a short outline of the decomposition: The idea is to first decompose $\boldsymbol{v}_2 = \boldsymbol{u}_2 + \boldsymbol{w}_2$ into the short range field $\boldsymbol{w}_2$ which couples to $\boldsymbol{w}_1$ and the long range field $\boldsymbol{u}_2$ which couples to $\boldsymbol{u}_1$. We choose $\boldsymbol{w}_2$ to be confined to the boundary layer so $\boldsymbol{w}_2 \to 0$ as $\zeta \to \infty$. Consequently $\boldsymbol{w}_2$ will be finite at the surface which gives the limiting velocity $\boldsymbol{u}_2^{\mathrm{Lim}}$ as a boundary condition on $\boldsymbol{u}_2$. We then make a further decomposition of the long range $\boldsymbol{u}_2$ into the outer streaming $\boldsymbol{u}_2^{\mathrm{Out}}$ and bulk streaming $\boldsymbol{u}_2^{\mathrm{Bulk}}$. $\boldsymbol{u}_2^{\mathrm{Out}}$ has $\boldsymbol{u}_2^{\mathrm{Out}} = \boldsymbol{u}_2^{\mathrm{Lim}}$ at the surface and can therefore be

thought of as the boundary-driven part of $\boldsymbol{u}_2$. $\boldsymbol{u}_2^{\text{Bulk}}$ then feels the interior driving term from $-\boldsymbol{\nabla}\cdot(\rho_0\boldsymbol{v}_1\boldsymbol{v}_1)$ and can be seen as the interior driven part. $\boldsymbol{u}_2^{\text{Bulk}}$ will then have no slip at the surface. Formally we then have,

$$\boldsymbol{v}_2 = \boldsymbol{u}_2 + \boldsymbol{w}_2 = \boldsymbol{u}_2^{\text{Out}} + \boldsymbol{u}_2^{\text{Bulk}} + \boldsymbol{w}_2. \tag{6.2}$$

As a boundary condition on the second order streaming we use particle-no-slip at the *moving* boundary which is discussed around Eq. (2.27b) and restated here,

$$\boldsymbol{v}_2 + \left\langle \frac{\mathrm{i}}{\omega}\boldsymbol{v}_1\cdot\boldsymbol{\nabla}\boldsymbol{v}_1 \right\rangle = \boldsymbol{0}. \qquad \text{at the wall mean level } \zeta = 0. \tag{6.3}$$

From the discussion above we then choose for each field,

$$\boldsymbol{w}_2 \to \boldsymbol{0} \qquad \text{as } \zeta\to\infty, \tag{6.4a}$$

$$\boldsymbol{u}_2^{\text{Out}} = -\left\langle \frac{\mathrm{i}}{\omega}\boldsymbol{v}_1\cdot\boldsymbol{\nabla}\boldsymbol{v}_1 \right\rangle - \boldsymbol{w}_2(\zeta=0) \equiv \boldsymbol{u}_2^{\text{Lim}} \qquad \text{at the wall mean level } \zeta = 0, \tag{6.4b}$$

$$\boldsymbol{u}_2^{\text{Bulk}} = \boldsymbol{0} \qquad \text{at the wall mean level } \zeta = 0, \tag{6.4c}$$

where we see that the sum $\boldsymbol{v}_2 = \boldsymbol{w}_2 + \boldsymbol{u}_2^{\text{Out}} + \boldsymbol{u}_2^{\text{Bulk}}$ at $\zeta = 0$ satisfies Eq. (6.3). Please notice that we have here defined the limiting velocity $\boldsymbol{u}_2^{\text{Lim}}$ in Eq. (6.4b).

In this chapter we will extensively make use of the relations Eqs. (2.5), (2.18) and (2.19) to simplify expressions. For convenience we restate them here,

$$\frac{\mathrm{i}\omega}{\rho_0 c_0^2}p_1 = \boldsymbol{\nabla}\cdot\boldsymbol{u}_1, \qquad \mathrm{i}\omega\rho_0\boldsymbol{u}_1 = \boldsymbol{\nabla}p_1(1-\mathrm{i}\Gamma), \qquad c_0^2\rho_1 = p_1, \tag{6.5}$$

where we recall that $\Gamma \sim \varepsilon^2 \sim 10^{-5}$ is small.

6.2 Short-range and long-range decomposition

We now motivate the decomposition of $\boldsymbol{v}_2$ into long range $\boldsymbol{u}_2$ and short range $\boldsymbol{w}_2$ by considering the external terms i.e. the terms which are products of first order fields.

6.2.1 Short range and long range parts of external terms

Please recall that $\boldsymbol{v}_1 = \boldsymbol{u}_1 + \boldsymbol{w}_1$ where $\boldsymbol{u}_1$ is the long range compressional field with $\boldsymbol{\nabla}\times\boldsymbol{u}_1 = \boldsymbol{0}$ whereas $\boldsymbol{w}_1$ is the short range shear field with $\boldsymbol{\nabla}\cdot\boldsymbol{w}_1 = 0$. We first investigate what part of $\boldsymbol{\nabla}\cdot\langle\rho_1\boldsymbol{v}_1\rangle = \langle\rho_1\boldsymbol{\nabla}\cdot\boldsymbol{v}_1\rangle + \langle\boldsymbol{v}_1\cdot\boldsymbol{\nabla}\rho_1\rangle$ in Eq. (6.1a) is short and long range using Eq. (6.5),

$$\langle\rho_1\boldsymbol{\nabla}\cdot\boldsymbol{v}_1\rangle = \langle\rho_1\boldsymbol{\nabla}\cdot\boldsymbol{u}_1\rangle = \frac{\omega}{\rho_0}\langle\rho_1(\mathrm{i}\rho_1)\rangle = 0, \tag{6.6a}$$

$$\langle\boldsymbol{v}_1\cdot\boldsymbol{\nabla}\rho_1\rangle = \langle\boldsymbol{w}_1\cdot\boldsymbol{\nabla}\rho_1\rangle + \frac{\rho_0\omega}{c_0^2}\langle\boldsymbol{u}\cdot(\mathrm{i}\boldsymbol{u}_1(1+\mathrm{i}\Gamma)\rangle = \langle\boldsymbol{w}_1\cdot\boldsymbol{\nabla}\rho_1\rangle - \frac{\rho_0\omega}{2c_0^2}\Gamma\left|\boldsymbol{u}_1\right|^2, \tag{6.6b}$$

where we have used that $\langle A(\mathrm{i}A)\rangle = 0$ and $\langle AA\rangle = \frac{1}{2}|A|^2$. In conclusion we can therefore write Eq. (6.1a) as

$$\boldsymbol{\nabla}\cdot\boldsymbol{v}_2 = -\frac{1}{\rho_0}\langle \boldsymbol{w}_1\cdot\boldsymbol{\nabla}\rho_1\rangle + \frac{\omega}{2c_0^2}\Gamma|\boldsymbol{u}_1|^2\,, \tag{6.7}$$

where the first term on the right hand side is short-range and the second is long-range. For the term $\langle\boldsymbol{\nabla}\cdot((\rho_0\boldsymbol{v}_1)\boldsymbol{v}_1)\rangle$ in Eq. (6.1b) we will simply write,

$$\langle\boldsymbol{\nabla}\cdot((\rho_0\boldsymbol{v}_1)\boldsymbol{v}_1)\rangle = \rho_0\boldsymbol{\nabla}\cdot\langle\boldsymbol{u}_1\boldsymbol{u}_1\rangle + \rho_0\boldsymbol{\nabla}\cdot[\langle\boldsymbol{v}_1\boldsymbol{v}_1 - \boldsymbol{u}_1\boldsymbol{u}_1\rangle]\,, \tag{6.8}$$

where the first term is long-range and the second term is short range.

6.2.2 Decomposition

We can now decompose $\boldsymbol{v}_2 = \boldsymbol{u}_2 + \boldsymbol{w}_2$ into long range $\boldsymbol{u}_2$ and short range $\boldsymbol{w}_2$ and for convenience we rename the pressure $p_2 \to p_2 + p_2^w$ so p_2^w is a short-range pressure and p_2 is long-range. $\boldsymbol{w}_2$ then takes all the short range components involving $\boldsymbol{w}_1$,

$$-\frac{1}{\rho_0}\langle\boldsymbol{w}_1\cdot\boldsymbol{\nabla}\rho_1\rangle = \boldsymbol{\nabla}\cdot\boldsymbol{w}_2 \tag{6.9a}$$

$$\boldsymbol{0} = -\boldsymbol{\nabla}p_2^w + \eta_0\nabla^2\boldsymbol{w}_2 + \eta_0\beta\boldsymbol{\nabla}(\boldsymbol{\nabla}\cdot\boldsymbol{w}_2) - \rho_0\boldsymbol{\nabla}\cdot[\langle\boldsymbol{v}_1\boldsymbol{v}_1 - \boldsymbol{u}_1\boldsymbol{u}_1\rangle]\,, \tag{6.9b}$$

and $\boldsymbol{u}_2$ takes the long range components involving $\boldsymbol{u}_1$,

$$\frac{\omega}{2c_0^2}\Gamma|\boldsymbol{u}_1|^2 = \boldsymbol{\nabla}\cdot\boldsymbol{u}_2 \tag{6.10a}$$

$$\boldsymbol{0} = -\boldsymbol{\nabla}p_2 + \eta_0\nabla^2\boldsymbol{u}_2 + \eta_0\beta\boldsymbol{\nabla}(\boldsymbol{\nabla}\cdot\boldsymbol{u}_2) - \rho_0\boldsymbol{\nabla}\cdot\langle\boldsymbol{u}_1\boldsymbol{u}_1\rangle\,. \tag{6.10b}$$

We see that the sum of these equations restores Eq. (6.1). Since $\boldsymbol{w}_1$ is confined to the boundary layer Eq. (6.9) is the governing equation for the inner streaming. Note that $\boldsymbol{u}_2$ also lives inside the boundary layer (see Fig. 6.1). The usual approach in the limiting velocity theory[1, 10] is to think of $\boldsymbol{w}_2$ as the full streaming inside the boundary layer and use matched asymptotics to match $\boldsymbol{w}_2$ and $\boldsymbol{u}_2$ at the *edge* of the boundary layer. This would corrospond to adding a constant to $\boldsymbol{w}_2$ in Fig. 6.1 so $\boldsymbol{w}_2(0) = \boldsymbol{0}$. However in this derivation we will think of $\boldsymbol{u}_2$ and $\boldsymbol{w}_2$ as sketched in Fig. 6.1.
We will return to the short range field and for now only notice that it is allowed to have a finite velocity at the surface which gives the limiting velocity $\boldsymbol{u}_2^{\mathrm{Lim}}$ as a boundary condition on $\boldsymbol{u}_2$ as sketched in Fig. 6.1. We will then first concentrate about the long range fields Eq. (6.10).

6.3 Outer streaming and bulk streaming decomposition

We now proceed by decomposing $\boldsymbol{u}_2$ into the boundary driven outer streaming $\boldsymbol{u}_2^{\mathrm{Out}}$ and the interior driven bulk streaming $\boldsymbol{u}_2^{\mathrm{Bulk}}$.

6.3.1 Bulk streaming force density

We first consider the term $-\rho_0 \boldsymbol{\nabla}\cdot\langle \boldsymbol{u}_1\boldsymbol{u}_1\rangle$ in Eq. (6.10b) which is the excess momentum current density from the first order fields away from the wall where $\boldsymbol{v}_1 \approx \boldsymbol{u}_1$. Using the relations in Eq. (6.5) and $\boldsymbol{\nabla}\times\boldsymbol{u}_1 = \boldsymbol{0}$, it evaluates to,

$$\boxed{-\rho_0 \langle \boldsymbol{\nabla}\cdot(\boldsymbol{u}_1\boldsymbol{u}_1)\rangle = \frac{1}{4}\boldsymbol{\nabla}\left[\kappa_0 |p_1|^2 - \rho_0 |\boldsymbol{u}_1|^2\right] + \Gamma\omega \langle \boldsymbol{u}_1\rho_1\rangle \qquad \text{for} \quad \zeta \gg \delta.} \tag{6.11}$$

This is an important result since it gives the force density $\Gamma\omega\langle \boldsymbol{u}_1\rho_1\rangle$ which drives the bulk streaming as we will see. The first term is an external gradient term which will be balanced by the pressure p_2 thus defining the effective pressure in the bulk[24],

$$\tilde{p}_2 \equiv p_2 - \frac{1}{4}\left[\kappa_0 |p_1|^2 - \rho_0 |\boldsymbol{u}_1|^2\right]. \tag{6.12}$$

Note that *any* external force density which is a gradient can be absorbed into the pressure in this way. This is equivalent with the hydrostatic pressure in a closed container which exactly balances the gravity potential such that the gravity drives no motion in steady state.
The second term $\Gamma\omega\langle \boldsymbol{u}_1\rho_1\rangle$ in Eq. (6.11) arise due to the bulk damping factor Γ of the first order fields. We can check if this is also a gradient by taking the curl. Using the Levi-Cevita symbol ϵ_{ijk} together with $\boldsymbol{\nabla}\times\boldsymbol{u}_1 = \boldsymbol{0}$ and Eq. (6.5) the curl becomes,

$$\begin{aligned}(\boldsymbol{\nabla}\times\langle \boldsymbol{u}_1\rho_1\rangle)_i &= \epsilon_{ijk}\partial_j\langle u_{1k}\rho_1\rangle = \langle \epsilon_{ijk}u_{1k}(\partial_j\rho_1)\rangle = \frac{\omega\rho_0}{c_0^2}\langle \epsilon_{ijk}u_{1k}(\mathrm{i}u_{1j}(1+\mathrm{i}\Gamma))\rangle \\ &= \frac{\rho_0}{c_0^2}\langle(\mathrm{i}\omega\boldsymbol{u}_1)\times\boldsymbol{u}_1\rangle_i,\end{aligned} \tag{6.13}$$

where we used that of course $\boldsymbol{u}_1\times\boldsymbol{u}_1 = \boldsymbol{0}$. We see that if the acceleration of fluid $\partial_t\boldsymbol{u}_1 = -\mathrm{i}\omega\boldsymbol{u}_1$ happens to be perpendicular to the velocity $\boldsymbol{u}_1$ this term can be comparable to $k_0U\rho_1 \sim \omega\rho_0U^2/c_0^2$ and the force density $\Gamma\omega\langle \boldsymbol{u}_1\rho_1\rangle$ will not be a gradient and therefore be a significant driving force in the bulk. This is the case for a rotating flow. On the other hand in the case of a one dimensional sound wave as considered in the example of Chapter 5 this will be very small and $\langle \boldsymbol{u}_1\rho_1\rangle$ will be a gradient field which is absorbed into $\tilde{p}_2$ thus driving no fluid motion. In conclusion if any bulk streaming (also called Eckard streaming[8]) occur, the responsible force density is $\Gamma\omega\langle \boldsymbol{u}_1\rho_1\rangle$.

6.3.2 Decomposition into outer streaming and bulk streaming

We are now ready to decompose Eq. (6.10) into outer streaming and bulk straming. We first notice that we can insert Eq. (6.10a) into $\eta_0\beta\boldsymbol{\nabla}(\boldsymbol{\nabla}\cdot\boldsymbol{u}_2)$ so this term becomes a gradient force density and is absorbed into $\tilde{p}_2$ thus redefining the pressure again. We will then decompose $\boldsymbol{u}_2 = \boldsymbol{u}_2^{\mathrm{Out}} + \boldsymbol{u}_2^{\mathrm{Bulk}}$ into the outer streaming $\boldsymbol{u}_2^{\mathrm{Out}}$ and the bulk streaming

$\boldsymbol{u}_2^{\text{Bulk}}$. The bulk streaming takes all the terms that has the bulk damping factor Γ,

$$\frac{\omega}{2c_0^2}\Gamma\left|\boldsymbol{u}_1\right|^2 = \boldsymbol{\nabla}\cdot\boldsymbol{u}_2^{\text{Bulk}}, \tag{6.14a}$$

$$\mathbf{0} = -\boldsymbol{\nabla}\tilde{p}_2^{\text{Bulk}} + \eta_0\nabla^2\boldsymbol{u}_2^{\text{Bulk}} + \Gamma\omega\left\langle\boldsymbol{u}_1\rho_1\right\rangle \tag{6.14b}$$

and the outer streaming has no driving terms,

$$0 = \boldsymbol{\nabla}\cdot\boldsymbol{u}_2^{\text{Out}}, \tag{6.15a}$$

$$\mathbf{0} = -\boldsymbol{\nabla}\tilde{p}_2^{\text{Out}} + \eta_0\nabla^2\boldsymbol{u}_2^{\text{Out}}, \tag{6.15b}$$

where we have defined the associated pressure so $\tilde{p}_2 = \tilde{p}_2^{\text{Bulk}} + \tilde{p}_2^{\text{Out}}$.

6.3.3 Nature of the bulk streaming field

The bulk streaming field in Eq. (6.14) is a field with an interior driving $\Gamma\omega\left\langle\boldsymbol{u}_1\rho_1\right\rangle$ and with no slip at the boundaries $\boldsymbol{u}_2^{\text{Bulk}} = \mathbf{0}$ from Eq. (6.4). Trivially if $\Gamma\omega\left\langle\boldsymbol{u}_1\rho_1\right\rangle$ is small (or a gradient) the bulk streaming will also be small. We will now show that $\boldsymbol{u}_2^{\text{Bulk}}$ can actually be modelled as divergence free. Suppose for a moment $\boldsymbol{u}_2^{\text{Bulk}} = \boldsymbol{\nabla}\phi^{\text{Bulk}} + \boldsymbol{\nabla}\times\boldsymbol{\Psi}^{\text{Bulk}}$. We then use that $\left\langle\boldsymbol{u}_1\rho_1\right\rangle$ varies over the distance $1/k_0$ in the bulk and it is therefore reasonable to assume that $\boldsymbol{u}_2^{\text{Bulk}}$ also varies over $1/k_0$. Then Eq. (6.14) gives the scaling of these fields if we write $U = \left|\boldsymbol{u}_1\right|$ and $\boldsymbol{\nabla}\to k_0$,

$$\left|\boldsymbol{\nabla}\phi^{\text{Bulk}}\right| \sim \Gamma\frac{U}{c_0}U \qquad \text{and} \qquad \left|\boldsymbol{\nabla}\times\boldsymbol{\Psi}^{\text{Bulk}}\right| \sim l^2\frac{\Gamma\omega}{\eta_0}\left|\left\langle\boldsymbol{u}_1\rho_1\right\rangle\right| \sim (1+\beta)\frac{\left|\left\langle\boldsymbol{u}_1\rho_1\right\rangle\right|}{\rho_0} \sim (1+\beta)\frac{U}{c_0}U \tag{6.16}$$

where we used $\left|\rho_1\right|/\rho_0 \sim U/c_0$ from perturbation theory. Consequently $\left|\boldsymbol{\nabla}\times\boldsymbol{\Psi}^{\text{Bulk}}\right|$ will be much larger than $\boldsymbol{\nabla}\phi^{\text{Bulk}}$ and we can model $\boldsymbol{u}_2^{\text{Bulk}}$ as solenoidal i.e. with $\boldsymbol{\nabla}\cdot\boldsymbol{u}_2^{\text{Bulk}} = 0$. Please note that this scaling could be violated if $\left\langle\boldsymbol{u}_1\rho_1\right\rangle$ is either a gradient or $\boldsymbol{u}_1$ and ρ_1 are out of phase. In that case both $\boldsymbol{\nabla}\phi^{\text{Bulk}}$ and $\boldsymbol{\nabla}\times\boldsymbol{\Psi}^{\text{Bulk}}$ would be small (compared to $\frac{U}{c_0}U$) and we have still only made errors of $\mathcal{O}(\Gamma)$.

Physically with $\boldsymbol{\nabla}\cdot\boldsymbol{u}_2^{\text{Bulk}} = 0$, Eq. (6.14) now describes a well known incompressible Stokes flow with interior driving. To get an order of magnitude of $\boldsymbol{u}_2^{\text{Bulk}}$ we should use the part of $\left\langle\boldsymbol{u}_1\rho_1\right\rangle$ which is not a gradient, so we find from Eq. (6.16),

$$\left|\boldsymbol{u}_2^{\text{Bulk}}\right| \sim (1+\beta)\frac{\left|\boldsymbol{\nabla}\times\left\langle\boldsymbol{u}_1\rho_1\right\rangle\right|}{k_0\rho_0}. \tag{6.17}$$

We should however mention that since $\boldsymbol{u}_2^{\text{Bulk}} = \mathbf{0}$ at the wall this is an upper limit on $\left|\boldsymbol{u}_2^{\text{Bulk}}\right|$ and we will often see much smaller result depending on how the force density $\Gamma\omega\left\langle\boldsymbol{u}_1\rho_1\right\rangle$ is distributed in the channel.

6.3.4 Nature of the outer streaming

Eq. (6.15) gives the nature of the boundary-driven outer streaming. This has no interior driving terms but is set into motion due to the limiting velocity in Eq. (6.4b) which will

be of order $(lk_0)^{-1}\frac{U^2}{c_0}$ as we will see in Section 6.4.3. Please recall $l \equiv \min\{R, 1/k_0\}$ is the variations of the compressional velocity field close to the surface. We can investigate how this boundary driven streaming then propagates into the bulk by taking the curl of Eq. (6.15b) giving the vorticity equation,

$$\mathbf{0} = \nabla^2(\boldsymbol{\nabla} \times \boldsymbol{u}_2^{\mathrm{Out}}). \tag{6.18}$$

We see that the vorticity $\boldsymbol{\nabla} \times \boldsymbol{u}_2^{\mathrm{Out}}$ satisfy a Laplace equation and thus has its maximum and minimum at the boundaries. The variations into the bulk will then be equal to the parallel variations at the boundary which is given by the limiting velocity $\boldsymbol{u}_2^{\mathrm{Lim}}$. It turns out that this is around half the acoustic wavelength which is then the decay length of $\boldsymbol{u}_2^{\mathrm{Out}}$ into the bulk as sketched in Fig. 6.1.

6.3.5 Concluding long range fields

We here summarize the field equations to solve to get the long range field $\boldsymbol{u}_2 = \boldsymbol{u}_2^{\mathrm{Bulk}} + \boldsymbol{u}_2^{\mathrm{Out}}$,

$$0 = \boldsymbol{\nabla} \cdot \boldsymbol{u}_2^{\mathrm{Bulk}}, \tag{6.19a}$$

$$\mathbf{0} = -\boldsymbol{\nabla}\tilde{p}_2^{\mathrm{Bulk}} + \eta_0\nabla^2\boldsymbol{u}_2^{\mathrm{Bulk}} + \Gamma\omega\,\langle \boldsymbol{u}_1\rho_1\rangle \tag{6.19b}$$

and,

$$0 = \boldsymbol{\nabla} \cdot \boldsymbol{u}_2^{\mathrm{Out}}, \tag{6.20a}$$

$$\mathbf{0} = -\boldsymbol{\nabla}\tilde{p}_2^{\mathrm{Out}} + \eta_0\nabla^2\boldsymbol{u}_2^{\mathrm{Out}}. \tag{6.20b}$$

with the boundary conditions,

$$\boldsymbol{u}_2^{\mathrm{Bulk}} = \mathbf{0} \qquad \text{and} \qquad \boldsymbol{u}_2^{\mathrm{Out}} = \boldsymbol{u}_2^{\mathrm{Lim}} \qquad \text{at the surface mean level } \zeta = 0. \tag{6.21}$$

We have here gone from the full Navier-Stokes equations Eq. (6.1) to these two simple incompressible Stokes flow problems which are much more intuitive to think of. Please note that $\boldsymbol{u}_2^{\mathrm{Bulk}}$ and $\boldsymbol{u}_2^{\mathrm{Out}}$ are completely uncoupled. In general we will always have outer streaming close to a boundary. We can then predict whether the bulk streaming is significant by introducing the ratio S between the magnitude of the two kinds of streaming,

$$S \equiv \frac{\left|\boldsymbol{u}_2^{\mathrm{Bulk}}\right|}{\left|\boldsymbol{u}_2^{\mathrm{Out}}\right|} \sim \frac{(1+\beta)\dfrac{|\boldsymbol{\nabla} \times \langle \boldsymbol{u}_1\rho_1\rangle|}{k_0\rho_0}}{(lk_0)^{-1}\dfrac{U^2}{c_0}} \sim (1+\beta)(lk_0)\frac{|\boldsymbol{\nabla} \times \langle \boldsymbol{u}_1\rho_1\rangle|}{k_0 U\,|\rho_1|} \tag{6.22}$$

where we used that $\rho_1/\rho_0 \sim U/c_0$ from perturbation theory. Please note that $lk_0 \leq 1$ so $\boldsymbol{u}_2^{\mathrm{Bulk}}$ can only be around $(1+\beta)$ times larger than $\boldsymbol{u}_2^{\mathrm{Out}}$. Thus we have the two cases,

$$S \ll 1 \qquad \text{Only outer streaming,} \tag{6.23}$$

$$S \approx 1 \qquad \text{Potentially both outer and bulk streaming.} \tag{6.24}$$

Hence we can tell from the first order calculations whether the bulk streaming can be important. In many cases we can then forget about the bulk streaming and the numeric resolving of the interior driving force $\Gamma\omega\left\langle \boldsymbol{u}_1\rho_1\right\rangle$ which we have experienced as a great advantage. As we mentioned $\boldsymbol{u}_2^{\text{Bulk}}$ can be much smaller than in this estimation. As an example for the rectangular channel in Chapter 5 we found from the first order fields $S \approx 10^{-2}$ but the second order solution gave $\left|\boldsymbol{u}_2^{\text{Out}}\right| / \left|\boldsymbol{u}_2^{\text{Bulk}}\right| \approx 10^{-5}$.

6.4 The short range field and limiting velocity

So far we have formulated the equations for the long range fields. In general the idea is to solve these equations numerically. We are now searching for the limiting velocity on $\boldsymbol{u}_2^{\text{Out}}$ to fulfil the boundary condition in Eq. (6.4),

$$\boldsymbol{u}_2^{\text{Lim}} \equiv -\left\langle \frac{\mathrm{i}}{\omega}\boldsymbol{v}_1\cdot\boldsymbol{\nabla}\boldsymbol{v}_1\right\rangle - \boldsymbol{w}_2(\zeta=0), \tag{6.25}$$

which involves the determination $\boldsymbol{w}_2$. The goal of this section is to solve for $\boldsymbol{w}_2$ at the boundary ignoring terms of $\mathcal{O}(\varepsilon)$. Since $\boldsymbol{w}_2$ is confined to a narrow region close to a possibly curved surface we will use the curvilinear differential operators from Section 4.3.

The problem to solve is given in Eq. (6.9) and restated here for convenience,

$$-\frac{1}{\rho_0}\left\langle \boldsymbol{w}_1\cdot\boldsymbol{\nabla}\rho_1\right\rangle = \boldsymbol{\nabla}\cdot\boldsymbol{w}_2 \tag{6.26a}$$

$$\boldsymbol{0} = -\boldsymbol{\nabla}p_2^w + \eta_0\nabla^2\boldsymbol{w}_2 + \eta_0\beta\boldsymbol{\nabla}(\boldsymbol{\nabla}\cdot\boldsymbol{w}_2) - \rho_0\boldsymbol{\nabla}\cdot\left[\left\langle \boldsymbol{v}_1\boldsymbol{v}_1 - \boldsymbol{u}_1\boldsymbol{u}_1\right\rangle\right], \tag{6.26b}$$

where we can write out the last term,

$$\left\langle\boldsymbol{\nabla}\cdot(\boldsymbol{v}_1\boldsymbol{v}_1 - \boldsymbol{u}_1\boldsymbol{u}_1)\right\rangle = \left\langle \boldsymbol{w}_1\cdot\boldsymbol{\nabla}\boldsymbol{u}_1\right\rangle + \left\langle \boldsymbol{w}_1\boldsymbol{\nabla}\cdot\boldsymbol{u}_1\right\rangle + \left\langle \boldsymbol{v}_1\cdot\boldsymbol{\nabla}\boldsymbol{w}_1\right\rangle. \tag{6.27}$$

Please note that since $|u_{1\zeta}|$ and $|w_{1\zeta}|$ are much smaller than $\left|\boldsymbol{u}_{1\parallel}\right|$ and $\left|\boldsymbol{w}_{1\parallel}\right|$ this forcing term will be essentially in the parallel direction. The strategy will therefore again be to solve for the parallel part $\boldsymbol{w}_{1\parallel}$ and then choose $w_{1\zeta}$ such that Eq. (6.26a) is satisfied. The pressure will balance gradient terms giving the hydrostatic pressure and the parallel equation thus becomes,

$$\partial_\zeta^2\boldsymbol{w}_{2\parallel} = \nu_0\left(\left\langle \boldsymbol{w}_1\cdot\boldsymbol{\nabla}\boldsymbol{u}_1\right\rangle_\parallel + \left\langle \boldsymbol{w}_1\boldsymbol{\nabla}\cdot\boldsymbol{u}_1\right\rangle_\parallel + \left\langle \boldsymbol{v}_1\cdot\boldsymbol{\nabla}\boldsymbol{w}_1\right\rangle_\parallel\right), \tag{6.28}$$

where we have used that $\nabla^2\boldsymbol{w}_2 = \partial_\zeta^2\boldsymbol{w}_2 + \mathcal{O}(\varepsilon)$ from Eq. (4.19). In Chapter B we have written out the full integration of this equation evaluating each term on the right hand side in curvilinear coordinates. It is a rather lengthy calculation and we only present the key points here.

6.4.1 Solution to the parallel part $\boldsymbol{w}_{2\parallel}$

The solution which has $\boldsymbol{w}_{2\parallel} \to \boldsymbol{0}$ as $\zeta \to 0$ is given in Eq. (B.13) and restated here,

$$\boldsymbol{w}_{2\parallel} = \frac{1}{\omega}\mathrm{Re}\Big\{ \tilde{\boldsymbol{u}}_{1\parallel} \cdot \boldsymbol{\nabla}_\parallel \tilde{\boldsymbol{u}}^*_{1\parallel} n_1 + \tilde{\boldsymbol{u}}^*_{1\parallel} \left[\partial_\zeta u_{1\zeta} n_2 + \boldsymbol{\nabla}_\parallel \cdot \tilde{\boldsymbol{u}}_{1\parallel} n_3\right] + \left[\tilde{\boldsymbol{u}}^*_{1\parallel}\left(\mathcal{H} v^{\mathrm{s}}_{1\zeta} + \boldsymbol{\nabla}_\parallel \cdot \boldsymbol{v}^{\mathrm{s}}_{1\parallel}\right) + \boldsymbol{v}^{\mathrm{s}}_{1\parallel} \cdot \boldsymbol{\nabla}_\parallel \tilde{\boldsymbol{u}}^*_{1\parallel}\right] n_4 + \left[\tilde{\boldsymbol{u}}_{1\parallel} \cdot \boldsymbol{\nabla}_\parallel (\boldsymbol{v}^{\mathrm{s}}_{1\parallel})^* - (v^{\mathrm{s}}_{1\zeta})^* \boldsymbol{Q}_{\tilde{u}}\right] n_5 + \tilde{\boldsymbol{u}}^*_{1\parallel} v^{\mathrm{s}}_{1\zeta} n_6 \Big\}, \tag{6.29}$$

where $n_i = n_i(\zeta)$ are function of ζ only and are listed in the appendix Eqs. (B.9) and (B.12). Further $\tilde{\boldsymbol{u}}_{1\parallel} \equiv (\boldsymbol{u}_{1\parallel} - \boldsymbol{v}^{\mathrm{s}}_{1\parallel})$ is the fluid velocity relative to the surface velocity and $\boldsymbol{Q}_{\tilde{u}} \equiv (\kappa_\xi \tilde{u}_{1\xi}, \kappa_\eta, \tilde{u}_{1\eta})$ is a curvilinear correction term ignored by Nyborg[1] and included by Lee *et al.*[10]. We then have to evaluate $\boldsymbol{w}_{2\parallel}$ at the boundary by evaluating $n_i(\zeta = 0)$. From Eq. (B.14),

$$\boldsymbol{w}_{2\parallel}(\zeta = 0) = \frac{1}{4\omega}\mathrm{Re}\Big\{ \tilde{\boldsymbol{u}}_{1\parallel} \cdot \boldsymbol{\nabla}_\parallel \tilde{\boldsymbol{u}}^*_{1\parallel} + \tilde{\boldsymbol{u}}^*_{1\parallel} \left[\partial_\zeta u_{1\zeta}(-2\mathrm{i}) + \boldsymbol{\nabla}_\parallel \cdot \tilde{\boldsymbol{u}}_{1\parallel}(2+\mathrm{i})\right] + \left[\tilde{\boldsymbol{u}}^*_{1\parallel}\left(\mathcal{H} v^{\mathrm{s}}_{1\zeta} + \boldsymbol{\nabla}_\parallel \cdot \boldsymbol{v}^{\mathrm{s}}_{1\parallel}\right) + \boldsymbol{v}^{\mathrm{s}}_{1\parallel} \cdot \boldsymbol{\nabla}_\parallel \tilde{\boldsymbol{u}}^*_{1\parallel}\right](2\mathrm{i}) + \left[\tilde{\boldsymbol{u}}_{1\parallel} \cdot \boldsymbol{\nabla}_\parallel (\boldsymbol{v}^{\mathrm{s}}_{1\parallel})^* - (v^{\mathrm{s}}_{1\zeta})^* \boldsymbol{Q}_{\tilde{u}}\right](-2\mathrm{i}) + \tilde{\boldsymbol{u}}^*_{1\parallel} v^{\mathrm{s}}_{1\zeta} \frac{2-2\mathrm{i}}{\delta} \Big\}. \tag{6.30}$$

This is the parallel velocity at $\zeta = 0$ induced by the force density $\rho_0 \boldsymbol{\nabla} \cdot \langle \boldsymbol{v}_1 \boldsymbol{v}_1 - \boldsymbol{u}_1 \boldsymbol{u}_1 \rangle$. In particular consider the very last term. If the perpendicular velocity $v^{\mathrm{s}}_{1\zeta} \neq 0$ this term becomes much larger than any other terms since $1/\delta \gg \boldsymbol{\nabla}_\parallel \sim k_0$. For a continuous reading, the physical interpretation of this term is put in Chapter C. It turns out that it cancels exactly when evaluating the parallel limiting velocity and will therefore not affect the streaming outside the boundary layer. In a full simulation though, one can experience very large perpendicular velocities inside the boundary layer if $v^{\mathrm{s}}_{1\zeta} \neq 0$.

6.4.2 Solution to the perpendicular part $w_{2\zeta}$

Having the parallel solution from Eq. (6.30) we now find $w_{2\zeta}$ from the continuity equation Eq. (6.26a),

$$\boldsymbol{\nabla} \cdot \boldsymbol{w}_2 = \boldsymbol{\nabla}_\parallel \cdot \boldsymbol{w}_{2\parallel} + \partial_\zeta w_{2\zeta} + \mathcal{H} w_{2\zeta} = -\frac{1}{\rho_0} \langle \boldsymbol{w}_1 \cdot \boldsymbol{\nabla} \rho_1 \rangle \,. \tag{6.31}$$

Since $\boldsymbol{w}_2$ varies rapidly in the ζ direction we have $\partial_\zeta w_{2\zeta} \gg \mathcal{H} w_{2\zeta}$. So we can find $w_{2\zeta}$ from integration,

$$w_{2\zeta} = -\int \boldsymbol{\nabla}_\parallel \cdot \boldsymbol{w}_{2\parallel} \,\mathrm{d}\zeta - \frac{1}{\rho_0} \int \langle \boldsymbol{w}_1 \cdot \boldsymbol{\nabla} \rho_1 \rangle \,\mathrm{d}\zeta, \tag{6.32}$$

and use $w_{2\zeta} \to 0$ as $\zeta \to \infty$. All terms will be of $\mathcal{O}(\varepsilon)$ except the last term in Eq. (6.30) considered above. The result is (see Chapter B for details),

$$w_{2\zeta} = -\frac{1}{4\omega}\mathrm{Re}\left\{2\mathrm{i}\boldsymbol{\nabla}_\parallel \cdot \left[\tilde{\boldsymbol{u}}^*_{1\parallel} v^{\mathrm{s}}_{1\zeta}\right]\right\}. \tag{6.33}$$

6.4.3 The limiting velocity

We are now ready to evaluate the limiting velocity $\boldsymbol{u}_2^{\mathrm{Lim}}$. From Eqs. (6.25), (6.30) and (6.33) and some manipulations we find (see Eqs. (B.3) and (B.24) for the full details),

$$\boldsymbol{u}_{2\|}^{\mathrm{Lim}} = -\frac{1}{4\omega}\mathrm{Re}\Big\{ \tilde{\boldsymbol{u}}_{1\|}\cdot\boldsymbol{\nabla}_{\|}\tilde{\boldsymbol{u}}_{1\|}^{*} + \tilde{\boldsymbol{u}}_{1\|}^{*}\left[\boldsymbol{\nabla}_{\|}\cdot\tilde{\boldsymbol{u}}_{1\|}(2+\mathrm{i}) + (\mathcal{H}v_{1\zeta}^{\mathrm{s}} + \boldsymbol{\nabla}_{\|}\cdot\boldsymbol{v}_{1\|}^{\mathrm{s}} - \partial_\zeta u_{1\zeta})(2\mathrm{i})\right] + (2\mathrm{i})\left[(v_{1\zeta}^{\mathrm{s}})^{*}\boldsymbol{Q}_u + \boldsymbol{v}_{1\|}^{\mathrm{s}}\cdot\boldsymbol{\nabla}_{\|}\boldsymbol{u}_{1\|}^{*} - \boldsymbol{u}_{1\|}\cdot\boldsymbol{\nabla}_{\|}(\boldsymbol{v}_{1\|}^{\mathrm{s}})^{*} + \boldsymbol{v}_{1\|}^{\mathrm{s}}\cdot\boldsymbol{\nabla}_{\|}(\boldsymbol{v}_{1\|}^{\mathrm{s}})^{*}\right]\Big\}, \tag{6.34a}$$

$$u_{2\zeta}^{\mathrm{Lim}} = -\frac{1}{4\omega}\mathrm{Re}\left\{2\mathrm{i}\left(\boldsymbol{u}_{1\|}\cdot\boldsymbol{\nabla}_{\|}(v_{1\zeta}^{\mathrm{s}})^{*} + v_{1\zeta}^{\mathrm{s}}\partial_\zeta u_{1\zeta}^{*}\right)\right\}, \tag{6.34b}$$

where we remind that $\tilde{\boldsymbol{u}}_{1\|} \equiv \boldsymbol{u}_{1\|} - \boldsymbol{v}_{1\|}^{\mathrm{s}}$, $\boldsymbol{Q}_u = (\kappa_\xi u_\xi, \kappa_\eta u_\eta)$ and $\mathcal{H} = -\kappa_\xi - \kappa_\eta$. This is the limiting velocity of the outer streaming $\boldsymbol{u}_2^{\mathrm{Bulk}}$ at $\zeta = 0$ for a curved and oscillating surfaces ignoring terms of $\mathcal{O}(\varepsilon)$. Please note that the curvature variables $\mathcal{H}$ and $\boldsymbol{Q}_u$ are both multiplied by $v_{1\zeta}^{\mathrm{s}}$ thus the curvature of the surface only becomes important for perpendicular surface velocities.

6.4.4 Example: Rayleigh streaming

In the very simple case of a one-dimensional standing wave over a stationary flat surface we have $\tilde{\boldsymbol{u}}_{1\|} = u_{1\xi}\cos(k_0\xi)\boldsymbol{t}_\xi$ where $u_{1\xi}$ is real and only the first and second term in Eq. (6.34a) will contribute,

$$u_{2\xi}^{\mathrm{Lim}} = -\frac{3}{8\omega}\partial_\xi[u_{1\xi}\cos(k_0\xi)]^2 = \frac{3}{8}\frac{u_{1\xi}^2}{c_0}\sin(2k_0\xi). \tag{6.35}$$

This is the classical Rayleigh solution for the limiting velocity[1]. It serves as a standard example with the two main points valid for one-dimensional standing waves parallel to a stationary flat surface,

(i) The limiting velocity is in the direction of decreasing acoustic velocity amplitude.

(ii) The parallel period of the limiting velocity is half the acoustic wavelength $\lambda/2$.

The first point also hold for a curved surface and in the second point $\lambda/2$ should just replaced by the variations due to the surface curvature.

[1]Lord Rayleigh[7] did not use the term *limiting velocity* which was first introduced by Nyborg[1].

6.5 Summary of effective modelling and implementation

We are hereby done for now with the derivation of the effective modelling in first and second order. We here give a summary of the effective models explained in this thesis.

First order acoustics (6.36a)

$$\nabla^2 p_1 + k_c^2 p_1 = 0 \qquad \text{and} \quad \boldsymbol{u}_1 = \frac{(1 - \mathrm{i}\Gamma)}{\mathrm{i}\omega\rho_0}\boldsymbol{\nabla} p_1$$

$$\partial_\zeta p_1 = \mathrm{i}\omega\rho_0 \left[v_{1\zeta}^{\mathrm{s}} - \frac{\mathrm{i}}{k_{\mathrm{s}}}\boldsymbol{\nabla}_\parallel \cdot \boldsymbol{v}_1^{\mathrm{s}} \right] - \frac{\mathrm{i}}{k_{\mathrm{s}}}\left(\partial_\zeta^2 p_1 + k_c^2 p_1\right) \qquad \text{at all surfaces}$$

Second order acoustic streaming (6.36b)

$$0 = \boldsymbol{\nabla}\cdot\boldsymbol{u}_2^{\mathrm{Bulk}}, \qquad 0 = \boldsymbol{\nabla}\cdot\boldsymbol{u}_2^{\mathrm{Out}},$$

$$\boldsymbol{0} = -\boldsymbol{\nabla}\tilde{p}_2^{\mathrm{Bulk}} + \eta_0\nabla^2\boldsymbol{u}_2^{\mathrm{Bulk}} + \Gamma\omega\left\langle \boldsymbol{u}_1\rho_1 \right\rangle, \qquad \boldsymbol{0} = -\boldsymbol{\nabla}\tilde{p}_2^{\mathrm{Out}} + \eta_0\nabla^2\boldsymbol{u}_2^{\mathrm{Out}}$$

$$\boldsymbol{u}_2^{\mathrm{Bulk}} = \boldsymbol{0} \qquad \text{at all surfaces,} \qquad \boldsymbol{u}_2^{\mathrm{Out}} = \boldsymbol{u}_2^{\mathrm{Lim}} \qquad \text{at all surfaces.}$$

with $\boldsymbol{u}_2^{\mathrm{Lim}}$ from Eq. (6.34) and the full streaming velocity being $\boldsymbol{v}_2 \approx \boldsymbol{u}_2 = \boldsymbol{u}_2^{\mathrm{Bulk}} + \boldsymbol{u}_2^{\mathrm{Out}}$. We have described the weak formulation of these problems in Chapter 3. The implementation of curvilinear local coordinate systems involves extensive use of projections onto the basis vectors. This procedure is in principle straight forward and the details are described in Chapter D. In the more complicated case of 3 dimensions we will in Chapter 7 visualize the local coordinate system on a sphere (see Fig. 7.2(b)).

In the following we will show two examples of applications of these effective models. We first revisit the simple setup from Section 5.2 where we now calculate the streaming and again compare the full model with he effective model. We then turn to a set-up studied experimentally by Hagsäter *et al.*[26] where a special streaming pattern occur. We will then show that this streaming pattern can be related to the bulk streaming force $\Gamma\omega\left\langle \boldsymbol{u}_1\rho_1 \right\rangle$ explained above.

6.6 Example: Rectangular channel from Section 5.2

As stated above the bulk streaming for this set-up will 10^{-5} of the boundary streaming and therefore we should only calculate $\boldsymbol{u}_2^{\mathrm{Out}}$ in Eq. (6.36b). In Figs. 6.2 and 6.3 we show the streaming velocity for the exact same set-up as considered in Section 5.2. We see in Fig. 6.2(a) that the effective model catches the streaming pattern very well. Note that this field is the classical Rayleigh streaming explained in Section 6.4.4 whith two rolls per half wave length. In Fig. 6.2(b-e) we investigate both components of the streaming velocity. Note how the effective model do not catch the rapid variations inside the boundary layer but fits well just away from the boundary layer. There are however small deviations from the full model. Note e.g. the contour misalignment in Fig. 6.2(b). To investigate this we have zoomed in on the boundary layer in Fig. 6.3 at $y = W/4$ and $y = 0$ respectively (as marked with blue in Fig. 6.2(b-c)). We first see that the parallel y-component indeed approaches the full model around 5δ away from the wall and thus is a perfect example of

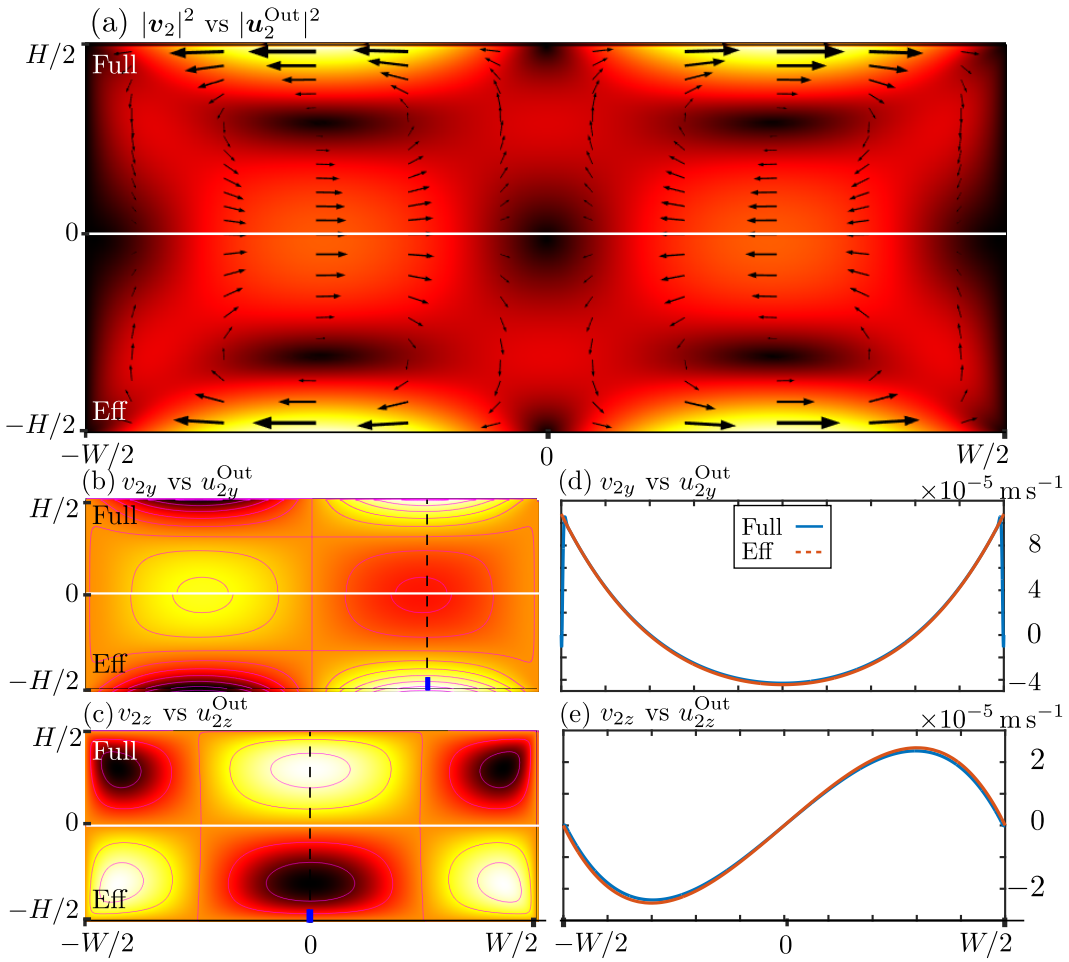

Figure 6.2: Plots of second order streaming with the same first order field as in Fig. 5.3. (a-c) Comparison between the a full model (upper part) and the effective model (lower part). (a) Streaming velocity amplitude from 0 to $10.8 \times 10^{-5}\,\mathrm{m\,s^{-1}}$ (black to white). (b) Horizontal streaming velocity from -1 to $1 \times 10^{-4}\,\mathrm{m\,s^{-1}}$ (black to white). (c) Vertical streaming velocity from -2.5 to $2.5 \times 10^{-5}\,\mathrm{m\,s^{-1}}$ (black to white). (d-e) Horizontal and vertical streaming velocity across the vertical dashed line at $y = W/4$ shown in (b-c) respectively.

the limiting velocity theory. The perpendicular component on the other hand does not approach the full velocity away from the boundary layer. We see that the perpendicular limiting velocity should ideally have been around $0.1 \times 10^{-5}\,\mathrm{m\,s^{-1}}$ larger than 0 as drawn with dashed line Fig. 6.3(b). Compared to the *maximum* parallel limiting velocity $10 \times 10^{-5}\,\mathrm{m\,s^{-1}}$ as seen in Fig. 6.3(a) this is an error of around 10^{-2}. Please recall that we in Eq. (6.32) estimated that $|w_{2\zeta}|$ would be $(k_0\delta) \sim 0.2 \times 10^{-2}$ smaller than $\max\left\{\left|\boldsymbol{w}_{2\parallel}\right|\right\}$ for stationary walls so this is a slightly larger error than expected. On the other hand we have seen that for Rayleigh streaming we have period doubling so $\left|\boldsymbol{\nabla}_\parallel \cdot \boldsymbol{w}_{2\parallel}\right| \sim 2k_0 \left|\boldsymbol{w}_{2\parallel}\right|$

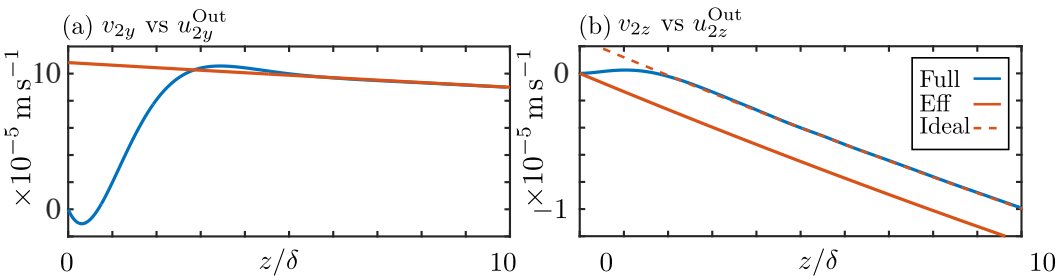

Figure 6.3: Plots of the streaming velocities close to the lower boundary $z = -H/2$ marked with blue line at $y = W/4$ and $y = 0$ as marked in Fig. 6.2(b) and (c) respectively.

and we should instead expect $|w_{2\zeta}| / \left|\boldsymbol{w}_{2\parallel}\right| \sim 2(k_0\delta) \sim 0.4 \times 10^{-2}$ which is more acceptable.

We have seen with this example that we can calculate the second order streaming in this simple case to sufficient accuracy. We will now move to a different set-up where the bulk streaming also becomes important.

6.7 Example: Bulk streaming from Hagsäter

In Fig. 6.2 we saw the characteristic Rayleigh streaming pattern also predicted in Section 6.4.4 where a half standing wave gave rise to *two* streaming rolls at each wall. However, in a paper by Hagsäter *et al.*[26] they observed experimentally only *one* streaming roll per half wavelength in a square chamber of $2 \times 2\,\text{mm}^2$ with 6 half waves in each direction as shown in Fig. 6.5(a). We will here show that this pattern can be related to the bulk streaming force $\Gamma \langle \boldsymbol{u}_1 \rho_1 \rangle$ explained in Section 6.3.1.

The experimental set-up and the reported pressure eigenmode is shown in Fig. 6.4(a) where a PIV-measurement tracks the velocity of 5 µm beads which are pushed towards the pressure nodes due to the acoustic radiation force[6]. The resulting streaming pattern is shown in Fig. 6.5(a) where 1 µm beads are used which follow the acoustic streaming rather than the radiation force. In Fig. 6.4(b) we have reproduced the pressure eigenmode in a channel of dimensions $H \times W = 2000 \times 2002\ \mu\text{m}^2$ where the slight asymmetry mimics the small arms in the experimental set-ups. Further Fig. 6.4(c-d) show this pressure at two different instants of time revealing the degeneracy of the mode with 3 wavelengths across the channel. i.e. the pressure is a superposition of two waves which have different phase and magnitude.

To analyse the impact on the streaming due to such degenerate modes we turn to a similar but much simpler set-up also studied numerically and experimentally by Antfolk and Muller[27] namely a $W \times H = 230 \times 230\,\mu\text{m}^2$ square channel with only one half wave in each direction. The idea is then to model 1/36 of the large Hagsäter-set-up in a much more controlled way as sketched in Fig. 6.5(b). We can then control the phase between the two waves by tuning the wall phase difference ϕ as shown in Fig. 6.5(b). For this particular

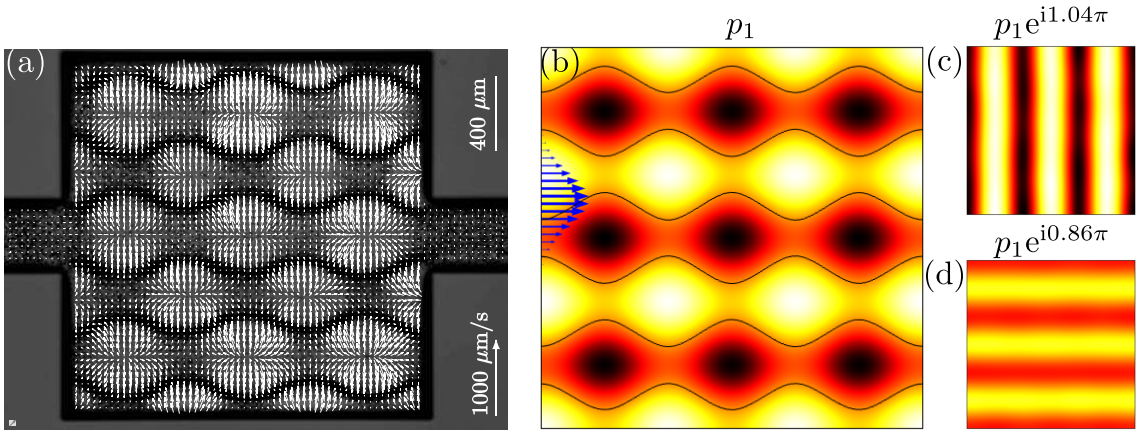

Figure 6.4: Experiment and simulation of the set-up by Hagsäter *et al.*[26]. (a) PIV measurement af $f = 2.17$ MHz of 5 µm beads which are pushed to the pressure nodes by the acoustic radiation force. Simulated pressure using the effective model with an arbitrary Gaussian actuation as shown in blue at $f = 2.24$ MHz. Black lines show $p_1 = 0$. (c-d) same as (b) but phase shifted. The colours of (c-d) are synchronized to $\pm 1.4 \times 10^4$ MPa (black-white).

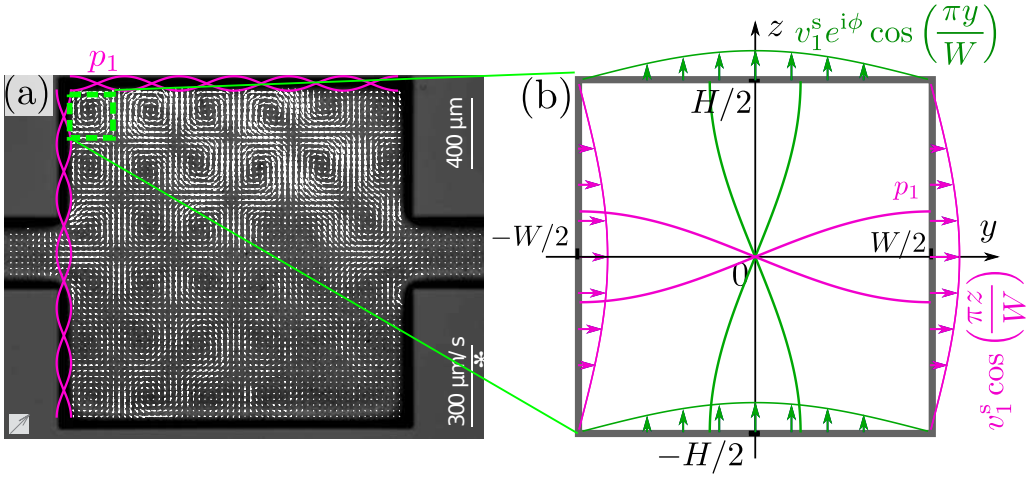

Figure 6.5: Illustration of the experiment by Hagsäter *et al.* and the simple model considered here. (a) Image from Hagsäter *et al.*[26] of a $2 \times 2\text{mm}^2$ champer with 6 pressure half-waves in each direction (magenta). The white arrows show the velocity of 1 µm particles from a PIV-measurement. For simplicity we only model one of theses structure (green square). (b) Sketch of a square channel with $W = 230\,\mu\text{m}$ as in[27] where both the side walls (magenta) and top/bottom walls (green) actuate an acoustic resonance in each direction with a temporal phase difference ϕ.

set-up (as we will see below) we have found $S \approx 2$ for $\phi = \pi/2$ so we now expect the bulk streaming to be significant.

6.7.1 Numerics

We first investigate how the bulk forcing term $\Gamma\omega \langle \boldsymbol{u}_1\rho_1 \rangle$ contribute to streaming. As discussed above, only the part which is not a gradient will contribute to bulk streaming. Therefore to measure the impact of this force we calculate the normalized average of the curl $\frac{1}{A}\int \frac{\boldsymbol{\nabla}\times\langle \boldsymbol{u}_1\rho_1\rangle}{k_0|\boldsymbol{u}_1||\rho_1|}\,\mathrm{d}A$. Please note that the fraction S is then $(1+\beta) = 4$ time this value. This is done in Fig. 6.6 where we change both the phase difference ϕ of the wall velocities and the height of the channel $H \to H + \frac{\mathrm{d}H}{H}$. From this figure we predict that the impact of this force is largest at symmetry $\frac{\mathrm{d}H}{H} = 0$ and $\phi = \pm\pi/2$. Further, as seen in Fig. 6.6(c) we can change the direction of this force by tuning the phase. In Fig. 6.7 we then show the calculated streaming pattern for nine characteristic sets of $(\phi, \frac{\mathrm{d}H}{H})$ calculated both in the full model and the effective model. We see that indeed a special streaming pattern occur at $\phi = \pm\pi/2$ and this is only significant close to symmetry $\frac{\mathrm{d}H}{H} = 0$ exactly as predicted from Fig. 6.6.

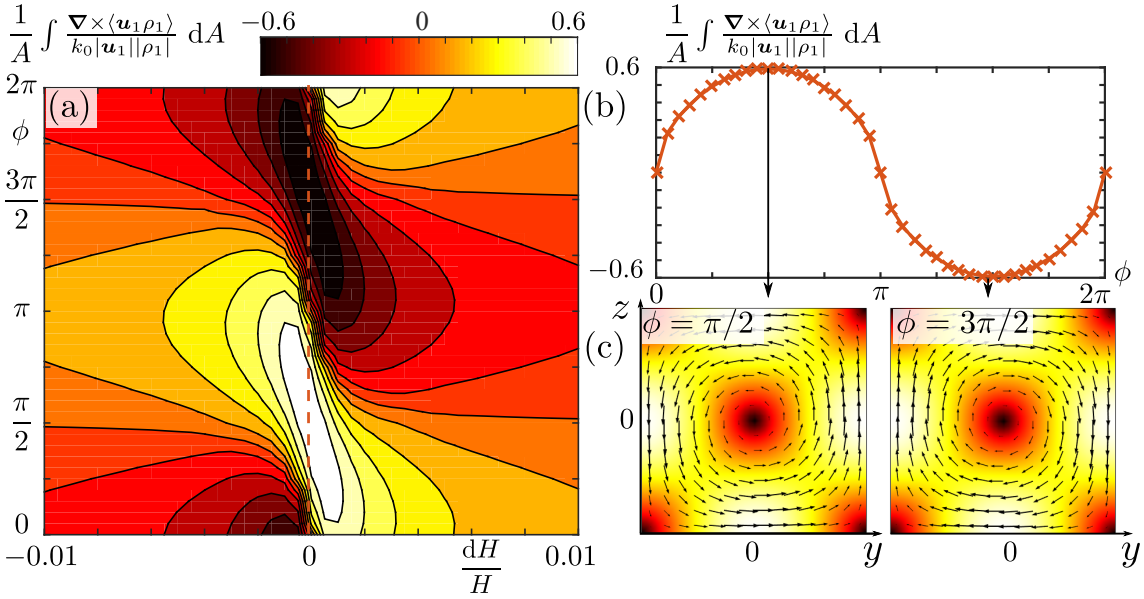

Figure 6.6: Analysis of streaming force $\Gamma\omega \langle \boldsymbol{u}_1\rho_1 \rangle$ in symmetric square set-up. (a) Contourplot of the average normalized curl of streaming force for $f = 3.252$ MHz giving resonance along y. Positive curl means counter-clockwise rotation as in (c-left). (b) line plot along the orange dashed line in (a). (c) Direction and magnitude of $\Gamma\omega \langle \boldsymbol{u}_1\rho_1 \rangle$ at the two maxima in (a) from 0 to 362 N m^{-3} (black-white).

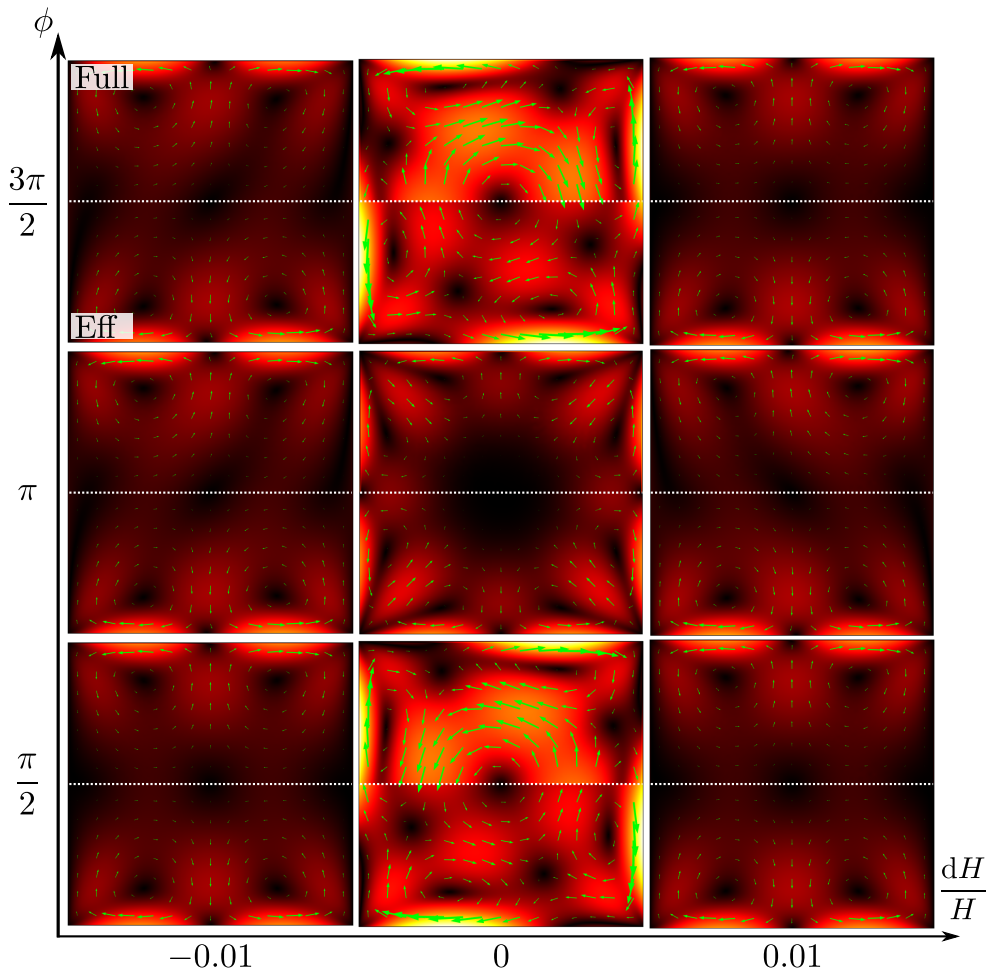

Figure 6.7: Streaming patterns close to symmetry. The streaming pattern for 9 different sets of $\mathrm{d}H/H$ and ϕ to be compared with Fig. 6.6. The frequency $f = 3.252$ MHz is always resonant in the y-direction. The upper part of all pictures show the full model and the lower part shows the effective model. Colors show streaming velocity from 0-8 ms^{-1} (black-yellow) and arrows show direction.

These special streaming patterns have three characteristics compared to the others:

(i) There is one large roll in the center with a diameter of around $\lambda/2$

(ii) At each wall half of the boundary streaming is suppressed and the other half is enhanced

(iii) The error between the full and effective model is much larger than in the other cases.

We will treat these three characteristics in the following.

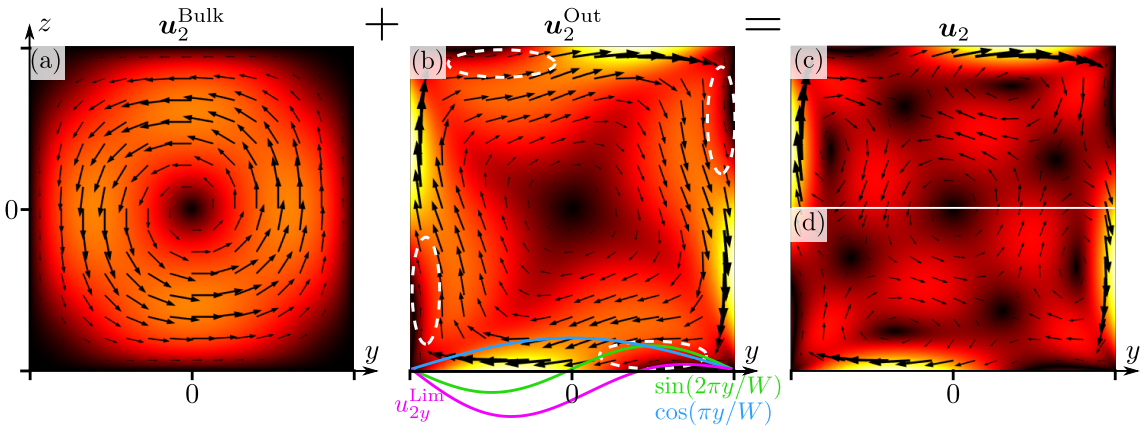

Figure 6.8: Streaming for same situation as Fig. 6.6 with $\phi = \pi/2$ and $\mathrm{d}H/H = 0$. Colours show velocity magnitude from 0-8 $\times\, 10^{-4}\,\mathrm{m\,s^{-1}}$ (black-yellow). (a-c) The bulk streaming $\boldsymbol{u}_2^{\text{Bulk}}$, outer streaming $\boldsymbol{u}_2^{\text{Out}}$ and their sum respectively calculated from Eq. (6.36). White dashed ellipses mark the areas where streaming is suppressed compared to Fig. 6.2(a). Coloured graphs are the components of Eq. (6.40). (d) The streaming $\boldsymbol{u}_2$ calculated from Eq. (6.10).

From the decomposition derived in this chapter we now have a powerful way to understand the first two characteristics. In Fig. 6.8(a-b) we show both $\boldsymbol{u}_2^{\text{Bulk}}$ and $\boldsymbol{u}_2^{\text{Out}}$ for $\phi = \pi/2$ and $\mathrm{d}H/H = 0$. From this we see clearly that $\boldsymbol{u}_2^{\text{Bulk}}$ follows the force shown in Fig. 6.6(c-left) which gives the bulk streaming with diameter of half a wavelength. The outer streaming in fact also show one large roll but in the opposite direction. We see clearly that half of the boundary streaming is suppressed (white ellipses). Finally their sum gives the more complicated pattern in Fig. 6.8(c) where we also show in Fig. 6.8(d) a calculation without decomposition (i.e. Eq. (6.10)) to confirm that our decomposition is right.

In this simple set-up we can understand the bulk streaming and the outer streaming from some simple analytics as treated in the following.

6.7.2 Analytics

Following the approach from Section 5.2 the pressure can be superimposed by the pressures resulting from each wall-pair each having the form of Eq. (5.22a) so we can write approximately,

$$p_1 = P_0 \left[\sin\left(\frac{\pi y}{W}\right) + e^{\mathrm{i}\phi} \sin\left(\frac{\pi z}{W}\right) \right], \tag{6.37}$$

where P_0 is a constant pressure.

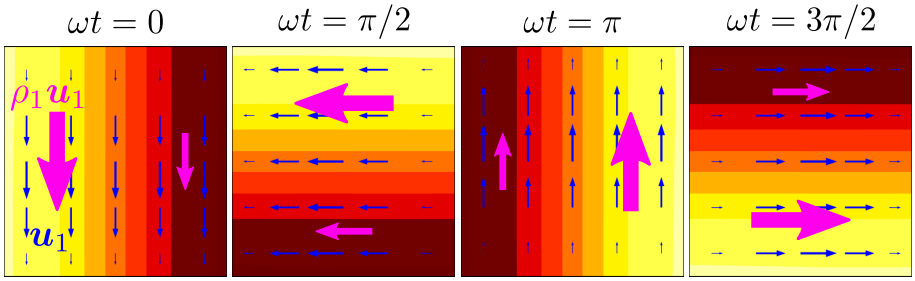

Figure 6.9: Time laps over one period of the mass density ρ_1 increasing from brown to yellow ($\pm 1.07\,\mathrm{kg\,m^{-3}}$) (or equivalently $p_1 = \pm 2.39$ MPa) together with fluid velocity $\boldsymbol{u}_1$ (blue arrows) with maximum of $1.26\,\mathrm{mm\,s^{-1}}$. The magenta arrows indicate the magnitude of the mass current density $\rho_1 \boldsymbol{u}_1$. This simulation at resonance $f = 3.252\,\mathrm{MHz}$ and $\phi = \pi/2$, $\mathrm{d}H/H = 0$.

Bulk streaming We first evaluate the term $\Gamma\omega \langle \boldsymbol{u}_1 \rho_1 \rangle$ driving the bulk streaming. With $\boldsymbol{u}_1 = \dfrac{1}{\mathrm{i}\omega\rho_0}\boldsymbol{\nabla} p_1$ and $\rho_1 = p_1/c_0^2$ we find the expression for the force density,

$$\Gamma\omega \langle \boldsymbol{u}_1 \rho_1 \rangle = \Gamma \frac{\pi P_0^2}{2W\rho_0 c_0^2} \left[-\cos\left(\frac{\pi y}{W}\right) \sin\left(\frac{\pi z}{W}\right) \boldsymbol{e}_y + \sin\left(\frac{\pi y}{W}\right) \cos\left(\frac{\pi z}{W}\right) \boldsymbol{e}_z \right] \sin(\phi). \quad (6.38)$$

This has the same form as we saw in Fig. 6.6(c-left) and is indeed maximized at $\phi = \pm\pi/2$ as shown in Fig. 6.6(b). It rotates in *one* large roll with diameter of a half wavelength and it has zeros at $\dfrac{|y| + |z|}{W} = n/\pi$, $n \in \mathbb{Z}$.

The physical interpretation of the large net mass transport $\langle \boldsymbol{u}_1 \rho_1 \rangle$ is illustrated in Fig. 6.9. It is a consequence of having phase shifted resonance in perpendicular directions. Focusing at e.g. the left part of the channel, at $t = 0$ the side walls compress fluid and the top/bottom walls pushes it downwards. Half a period later $\omega t = \pi$ decompressed fluid moves upwards. Over a full period this implies a net mass transport $\langle \boldsymbol{u}_1 \rho_1 \rangle$ downwards in this left side of the channel. The overall picture is then a rotating mass transport as shown in Fig. 6.6(c-left). As predicted in Eq. (6.13) we here get a large bulk force since the fluid is rotating.

Outer streaming Comparing with the Rayleigh streaming in Fig. 6.2 we see that half of the boundary-streaming is suppressed Fig. 6.8 (marked with white ellipses). We now have a tool for understanding this, namely the limiting velocity. Investigating the parallel limiting velocity from Eq. (6.34a) at the bottom wall $z = -H/2$ gives,

$$u_{2y}^{\mathrm{Lim}} = -\frac{1}{4\omega} \mathrm{Re}\left\{ u_{1y} \partial_y u_{1y}^* + u_{1y}^* \partial_y u_{1y} (2 + \mathrm{i}) - (2\mathrm{i}) u_{1y}^* \partial_z u_{1z} \right\}. \quad (6.39)$$

Again using $\boldsymbol{u}_1 = \dfrac{1}{\mathrm{i}\omega\rho_0}\boldsymbol{\nabla} p_1$ and p_1 from Eq. (6.37) we find,

$$u_{2y}^{\mathrm{Lim}} = c_0 \left(\frac{P_0}{\rho_0 c_0^2}\right)^2 \left[\frac{3}{8} \sin\left(2\frac{\pi y}{W}\right) - \frac{1}{2} \cos\left(\frac{\pi y}{W}\right) \sin(\phi) \right], \quad (6.40)$$

The first term (green in Fig. 6.8(b)) gives the Rayleigh streaming pattern as in Fig. 6.2(a) i.e. with two rolls per half wave. The second term (blue in Fig. 6.8(b)) is maximum at a wall phase difference of $\phi = \pi/2$ for which it is positive across the entire channel. It arises since the bottom wall creates a large gradient $\partial_z u_{1z}$ in the perpendicular velocity. The entire u_{2y}^{Lim} at the bottom then becomes enhanced to the left and supressed to the right as shown with magenta in Fig. 6.8(b).

We have here seen that a special streaming pattern can occur as a result of perpendicular resonances inducing rotations in the fluid. This is most likely the phenomena observed by Hagsäter *et al.* in Fig. 6.5. Further we have seen that a perpendicular gradient $\partial_\zeta u_{1\zeta}$ can affect the limiting velocity significantly. Maybe this can be used in a more efficient suppression of streaming.

However, in Fig. 6.7 we saw a remarkable large error between the full and effective model for these situations but a similar result for the other. Even though the qualitative behaviour is well calculated, the quantitative error is too large to accept. We will investigate this error in the following.

6.7.3 Error between effective and full model

In Fig. 6.10 we show the case $\phi = \pi/2$, $\mathrm{d}H/H = 0$ and plot the velocities along the center line $z = 0$ which show that u_{2y} (circles) fits well but u_{2z} (triangles) differs significantly from the full model. Still u_{2z} approaches v_{2z} close to the wall, so we believe that the error is a bulk effect and not an error in the limiting velocity. The picture is opposite for the

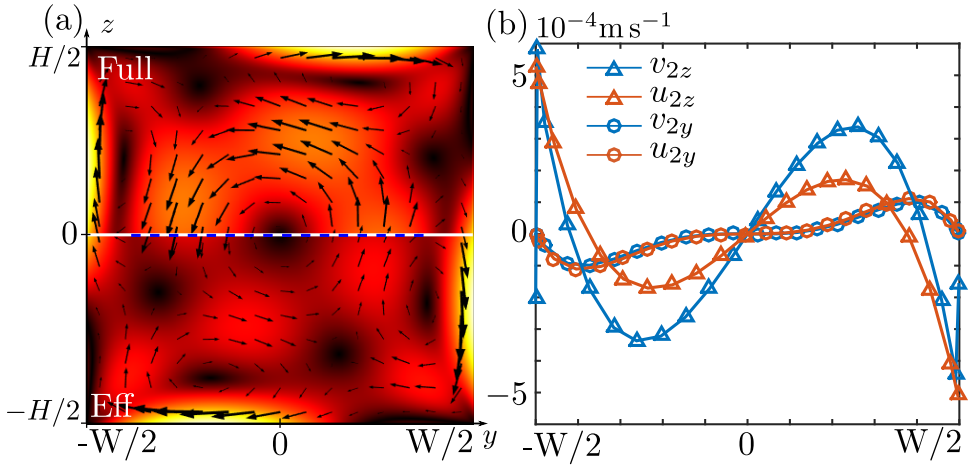

Figure 6.10: Comparison between the effective and full model in the square channel. (a) Magnitude and direction of streaming calculated with the full (upper) and effective (lower) model. Same color scale as Fig. 6.8. (b) the streaming velocities along the white center line $z = 0$ in (a). Note that the z- components have large errors while the y- components fit well.

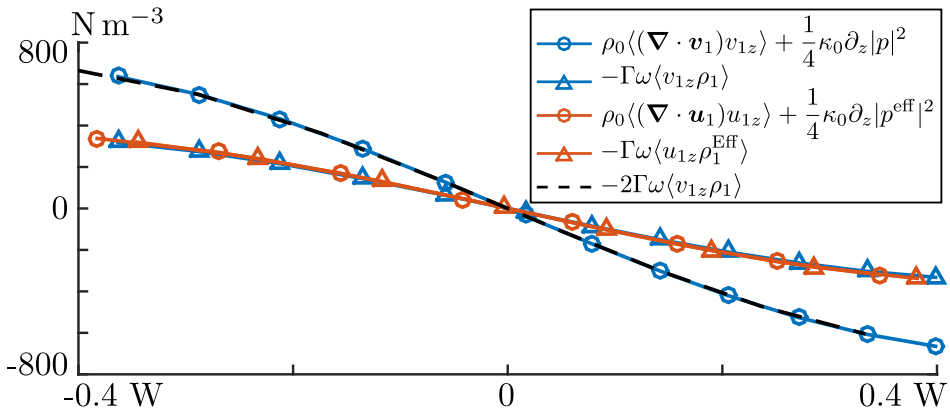

Figure 6.11: Possible origin of streaming error in Fig. 6.10. We here check Eq. (6.41a) and the graphs show the left hand side (circles) and right hand side (trangles) of the full (blue) and effective (red) model respectively. The black dashed line show the right hand side of Eq. (6.41a) multiplied by 2 for the full model.

line $y = 0$ (not shown).

The origin of this error is not fully understood but after backtracking the entire derivation we can suggest one crucial point. When deriving the force density $\Gamma\omega\,\langle \boldsymbol{u}_1\rho_1\rangle$ we used $\boldsymbol{\nabla}\cdot\boldsymbol{u}_1 = \dfrac{\mathrm{i}\omega}{\rho_0 c_0^2}p_1$ and $\boldsymbol{u}_1 = \dfrac{\boldsymbol{\nabla}p_1}{\mathrm{i}\omega\rho_0}(1-\mathrm{i}\Gamma)$ and expected that

$$\text{Expected:} \qquad \rho_0\,\langle(\boldsymbol{\nabla}\cdot\boldsymbol{v}_1)v_{1z}\rangle + \frac{1}{4}\kappa_0\partial_z|p_1| = -\Gamma\omega\,\langle v_{1z}\rho_1\rangle\,. \tag{6.41a}$$

since we assume $\boldsymbol{v}_1 \approx \boldsymbol{u}_1$ in the bulk. We check this equation in Fig. 6.11 where we plot the left hand side (circles) and right hand side (triangles) for both the effective (red) and full (blue) model. We see that the effective model satisfies this equation as expected. The full model however does not satisfy the equation. In fact from the black dashed curve it seems like the right hand side should be doubled,

$$\text{From full simulation:} \qquad \rho_0\,\langle(\boldsymbol{\nabla}\cdot\boldsymbol{v}_1)v_{1z}\rangle + \frac{1}{4}\kappa_0\partial_z|p_1| = -2\Gamma\omega\,\langle v_{1z}\rho_1\rangle\,. \tag{6.41b}$$

Please note that we are here only plotting *first order fields* so this has nothing to do with the derivations in this chapter. Further, this is a *full simulation* that does not fit with the analytics so ssuming the full simulation to be true we might have missed a $\mathcal{O}(\Gamma)$-term in our analytic work. We can localize two places where we made assumptions to reach Eq. (6.41a),

(i) $\boldsymbol{v}_1 \approx \boldsymbol{u}_1$ in the bulk,

(ii) $\left[\nabla^2\boldsymbol{u}_1 + k_\mathrm{c}^2\boldsymbol{u}_1\right] + \dfrac{k_\mathrm{c}^2}{k_\mathrm{s}^2}\left[\nabla^2\boldsymbol{w}_1 + k_\mathrm{s}^2\boldsymbol{w}_1\right] = \boldsymbol{0} \quad \Rightarrow \quad \nabla^2\boldsymbol{u}_1 + k_\mathrm{c}^2\boldsymbol{u}_1 = \nabla^2\boldsymbol{w}_1 + k_\mathrm{s}^2\boldsymbol{w}_1 = \boldsymbol{0}.$

Since the error seem to be a nice factor of 2 there is also the third possibility that we made a simple typo in our numerics or analytics. Due to limited time we have not been able to localize this error.

We saw from Fig. 6.7 that this error only occurs when simulating the bulk streaming $\boldsymbol{u}_2^{\text{Bulk}}$ and in Fig. 6.6 we show that we could predict whether bulk streaming would be significant at all. As we have seen this is a rare phenomena related to a degenerate resonance in different directions and in asymmetric set-ups we will only expect insignificant bulk streaming and hence small errors. Even in the case of bulk streaming we have seen from Fig. 6.10(a) that the qualitative streaming fits well and we "only" need to find a factor of ~ 2 somewhere. Finally from Fig. 6.8(c-d) we justified our decomposition from $\boldsymbol{u}_2 \to \boldsymbol{u}_2^{\text{Bulk}} + \boldsymbol{u}_2^{\text{Out}}$.

6.8 Concluding remarks on effective model for streaming

We have in this chapter provided the limiting velocity as a boundary condition for $\boldsymbol{u}_2^{\text{Out}}$ which is valid for curved walls with actuation in any direction. Due to many complicated terms we have not been able to rigorously test all possible scenarios of this limiting velocity, so there something for future work here.

Further we have derived a decomposition of the total streaming field into the inner streaming $\boldsymbol{w}_1$, outer streaming $\boldsymbol{u}_2^{\text{Out}}$, and bulk streaming $\boldsymbol{u}_2^{\text{Bulk}}$. This decomposition allows for a much more intuitive formulation of the streaming equations and as we have seen in the example of the square channel we can now analyse complicated streaming patterns in more detail by considering each of these fields separately. In particular we have shown that the special streaming pattern observed by Hagsäter *et al.* can be related to degenerate resonances in perpendicular directions. In this set-up we also saw how streaming above an oscillating wall can be suppressed in some areas due to perpendicular gradients in the velocity $\partial_\zeta u_{1\zeta}$. This phenomena can potentially be used to design new acoustofluidic devices where streaming is much more efficiently suppressed than we have here seen.

With the effective model derived in this chapter we are now in a position to simulate acoustic streaming in larger 3-dimensional systems which we will show in an example in the next chapter.

Chapter 7

3-dimensional acoustic streaming

In the preceding chapter we tested our effective model and found good agreement with a full model in spite of the error in the bulk forcing term. In the following we will enter the regime where it is not so easy to compare with a full model namely acoustic streaming in 3 dimensions. As we mention in Chapter 1 one of the goals of acoustofluidics is to obtain control of particles suspended in a liquid. Whereas large particles can be efficiently focused by the acoustic radiation force[25], smaller particles ($\lesssim 1$ µm) will be dragged around in patterns similar to those we saw in Chapter 6. One way of of trapping sub-micron particles is by using a seed particle in a so-called acoustic trap. As shown experimentally by Hammarström *et al.* a larger seed particle can bee levitated in the center of a channel coursing smaller nano particles to be trapped on that seed particle. In Fig. 7.1 we show some figures from this experiment. The channel shown here has a cross section of 0.2×2 mm^2 and a half

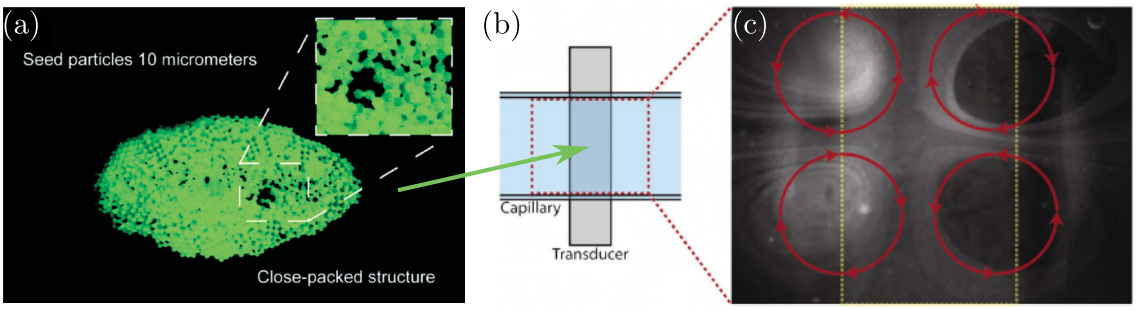

Figure 7.1: Acoustic trapping figures adapted from the paper by Hammarström *et al.*[13]. (a) seed particle constituted by 10 µm polysterene beads. The insert show small cavities where nano particles can be trapped. Due to to the acoustic radiation force the seed particles is fixed in the center of the channel shown in (b). (b) top view of the channel with cross section 0.2×2 mm^2 (into the paper $\times$ vertically) with flow from left to right. The transducer below the channel induces a half wave resonance in the shortest direction (into the paper). (c) The acoustic streaming pattern inside the channel without seed particle. Yellow lines show the transducer area.

wave resonance is induced along the smallest dimension. The streaming pattern shown in

Fig. 7.1(c) is studied by Lei *et al.* [28] and is different from what we have seen so far in this thesis. It has dimensions of the channel width which is much longer than the wavelength $\lambda \approx 0.4$ mm. In the experiment it is pointed out that this streaming pattern can help collecting small nano particles into the center where they can be trapped at the seed particle. This particular streaming pattern is not fully understood but Lei suggests an explanation based on the term $\frac{1}{4\omega}\mathrm{Re}\left\{\boldsymbol{u}_{1\|}^{*}(2\mathrm{i}\partial_\zeta u_{1\zeta})\right\}$ from the limiting velocity Eq. (6.34). This term can indeed be large in this flat channel since $\partial_\zeta u_{1\zeta}$ scales inversely with the channel height.

In this chapter we will not go into any detail about the streaming in Fig. 7.1(c) but instead focus on the streaming due to the presence of the seed particle. Part of the purpose of this example will be to show the entire machinery of effective modelling of acoustic streaming in 3D curvilinear coordinates.

7.1 Acoustic streaming around a sphere

In Fig. 7.2(a) we show the set-up we choose here which is a closed box of dimensions $L \times W \times H = 500 \times 700 \times 200$ µm^3 with a sphere of radius $R = H/4 = 50$ µm in the center. We choose to oscillate the bottom surface in the interval $-L/4 < x < L/4$ with an amplitude $d_1 = 0.1$ nm and resonance frequency $f = 3.7028$ MHz inducing a half wave resonance as shown in Fig. 7.2(a). In Fig. 7.2(b) we show the local curvilinear basis vectors in each point at the sphere. Please note that the normal vector $\boldsymbol{n}$ always points towards the fluid but the tangent vectors $\boldsymbol{t}_\xi$,$\boldsymbol{t}_\eta$ point in completely different directions from point to point while satisfying the right hand rule $\boldsymbol{t}_\xi \times \boldsymbol{t}_\eta = \boldsymbol{n}$. In Chapter D we show how these basis vectors are implemented in COMSOL.

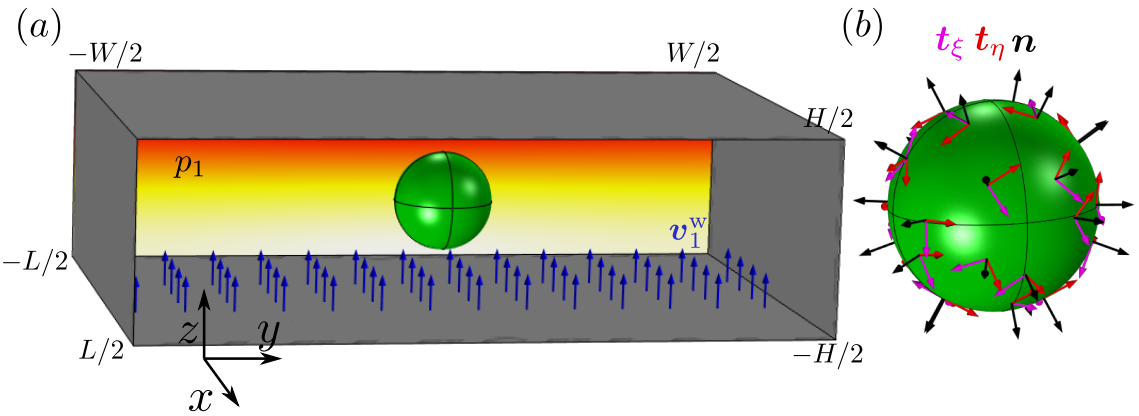

Figure 7.2: Simple 3D setup to model streaming around a seed particle. (a) A sphere of radius $R = H/4 = 50$ µm mimics the seed particle and is placed in the center of a closed box with dimensions $L \times W \times H = 500 \times 700 \times 200$ µm^3. The bottom wall induces a half wave resonance of $p_1 = \pm 1.73$ MPa (white-black) in the z-direction with $f = 3.7028$ MHz. The coordinate system (x, y, z) has origo in the center of the sphere. (b) The local curvilinear basis vectors $\boldsymbol{t}_\xi, \boldsymbol{t}_\eta, \boldsymbol{n}$ in different points at sphere.

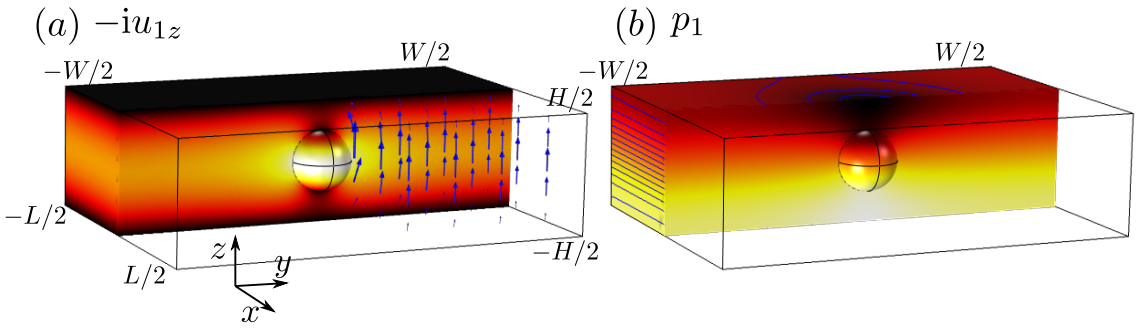

Figure 7.3: The first-order fields u_{1z} and p_1 inside the set-up in Fig. 7.2. (a) first order vertical velocity $-\mathrm{i}u_{1z}$ where the phase is with respect to the wall phase. Colors show 0-1.49 m s^{-1} (black-white). (b) first order pressure p_1 from ± 1.74 MPa (white-black). Blue lines are contours separated 0.174 MPa.

7.1.1 First order analysis

We first solve for the first-order fields by solving the effective model Eq. (6.36). The results are shown in Fig. 7.3. Note how large velocity gradients of order u_{1z}/R are formed at the sphere. These give rise to a large limiting velocity as we will see. The next step is to project these results from (x, y, z) onto the curvilinear basis vectors $\boldsymbol{t}_\xi, \boldsymbol{t}_\eta, \boldsymbol{n}$ shown at the sphere in Fig. 7.2(b) and then calculate the limiting velocity from Eq. (6.34). That result is then projected back to the (x, y, z) coordinate system (see Chapter D). In Fig. 7.4 we show the limiting velocity as surface plots. Please note that the magnitude $|\boldsymbol{u}_2^{\mathrm{Lim}}|$ is around 10 times larger at the sphere than at the side walls. Note also the smoothness of of $\boldsymbol{u}_2^{\mathrm{Lim}}$ at the sphere even though the local basis vectors in Fig. 7.2(b) are completely discontinuous. The final step in the first-order analysis is to evaluate the ratio S between

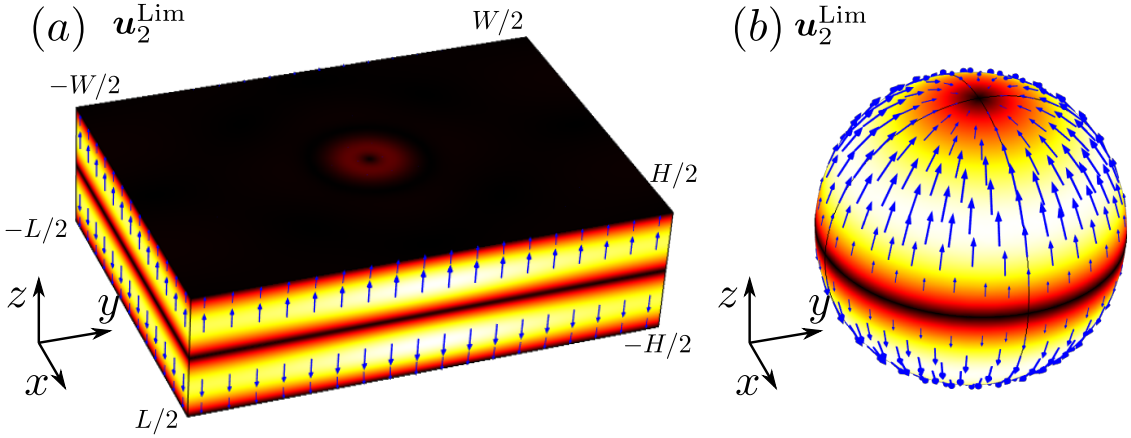

Figure 7.4: 3D visualization of the limiting velocity. (a) colors show the magnitude $\left|\boldsymbol{u}_2^{\mathrm{Lim}}\right|$ from 0-2.06 $\times$ 10^{-4} m s^{-1} (black-white) and arrows show direction. (b) colors show the magnitude $\left|\boldsymbol{u}_2^{\mathrm{Lim}}\right|$ from 0-1.19 $\times$ 10^{-3} m s^{-1} (black-white) and arrows show direction.

bulk streaming and outer streaming from Eq. (6.22). For this set-up we found numerically $S \approx 10^{-3}$ and consequently we only have to calculate the outer streaming, $\boldsymbol{u}_2 \approx \boldsymbol{u}_2^{\text{Out}}$.

7.1.2 Second order analysis

The outer streaming $\boldsymbol{u}_2^{\text{Out}}$ is visualized in 3D in Fig. 7.5 where we show direction and magnitude of $\boldsymbol{u}_2^{\text{Out}}$. As expected the streaming is much larger close to the sphere due to the geometric variations here. We see that rolls are formed in the yz-plane while a "sink" is formed in the xy-plane with streaming towards the sphere. In Fig. 7.6 we show sections close to the sphere of these two planes where these effects are shown more clearly. We see in Fig. 7.6(b) that the in the xy-plane the streaming is towards the sphere within a distance of $\sim 3R$. We compare this result with the analytic solution to the radial streaming velocity due to a free sphere from Lee *et al.*[24],

$$u_{2r}^{\infty} = -\frac{45}{32}\frac{P^2}{\omega R \rho_0^2 c_0^2}\left[\frac{R^2}{r^2} - \frac{R^4}{r^4}\right] \qquad \text{at } z = 0. \tag{7.1}$$

where P is the pressure amplitude. We see that the simulated result decays over a shorter distance probably due to the top/bottom walls. To investigate this we increased the height to $H = 900$ µm and plotted the normalized velocity $u_{2y}^{900} = u_{2y}\frac{(P^{900})^2}{P^2}\frac{\omega}{\omega^{900}}$, in the same plot where superscript 900 refers to this second simulation with $H = 900$ µm. We see from the new curve in Fig. 7.6(b) (dashed orange) that the streaming indeed approaches the analytic result for a free sphere as we increase the height of the box as expected. Please note that we still have $W/2 = 7R$ and $L/2 = 5R$, so to get a better fit we should increase

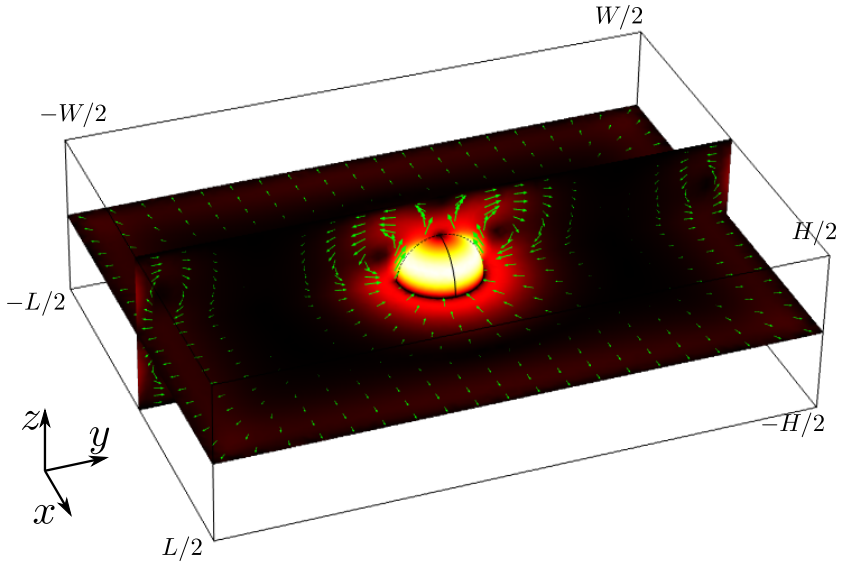

Figure 7.5: 3D visualization of streaming around the sphere. The green arrows show direction of $\boldsymbol{u}_2$ with logarithmic magnitude. Colours show the magnitude $|\boldsymbol{u}_2|$ from 0-1.2×10^{-3} m s^{-1}.

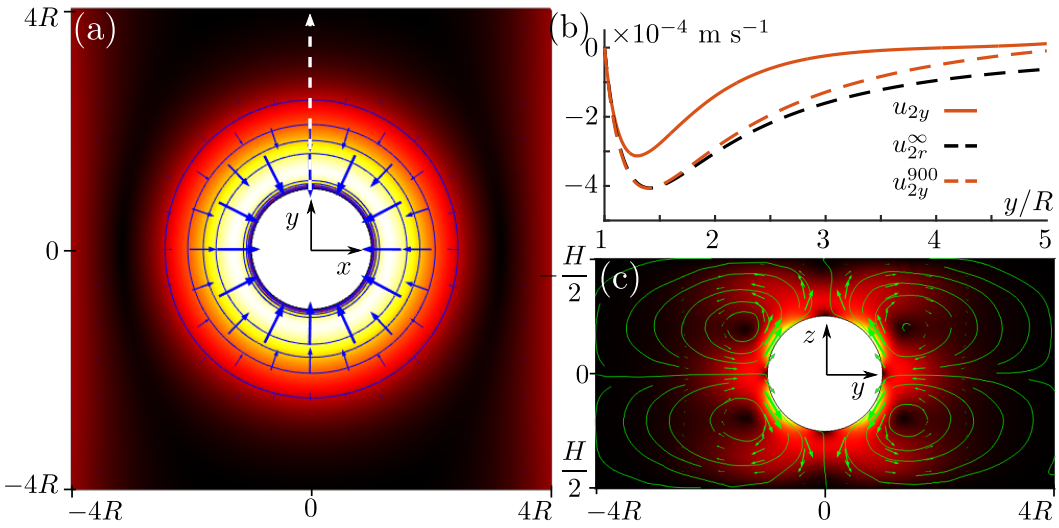

Figure 7.6: 2D and 1D visualisation of streaming around the sphere. (a) section of the xy-plane from Fig. 7.5 showing magnitude from 0-3.16 $\times$ 10^{-4} ms^{-1} (black-white) and direction (blue arrows). Contours separation is 20% of the maximum value. (b) Radial velocity along the white dashed line in (a). u_{2y} (orange) is the simulation for the system shown in Fig. 7.2. u_{2y}^{900} is the normalized streaming velocity (see text) for $H = 900$ µm and W, L fixed. u_{2r}^{∞} (black dashed) is the analytic result from Lee *et al.* [24]. (c) section of the yz-plane in Fig. 7.5. The green arrows show the streaming direction with proportional magnitude. Colors show the magnitude $|\boldsymbol{u}_{2yz}|$ from 0-1.18 $\times$ 10^{-3} m s^{-1}.

all dimensions of the box which we will not do here. We cannot simply reduce the radius of the sphere since we then violate $R/\delta \ll 1$.

Since we have seen that the streaming due to the sphere is much stronger than the streaming due to the side walls it becomes hard to believe that the transducer plane streaming pattern observed in the experiment without seed particle (Fig. 7.1(c)) should be the only reason for attracting nanoparticles onto the seed particle. Since the transducer plane streaming of Fig. 7.1(c) probably originates from variations in the velocity over the system dimensions as proposed by Lei *et al.* [28] the next step will be to make a simulation of the *open* channel and with the right transducer actuation envelope.

Finally, although we did not make a convergence test in 3D we mention that this setup was solved with 440936 DOF and 23 GB RAM for p_1 with quartic shape functions and 621458 DOF and 37 GB RAM for $\boldsymbol{u}_2^{\text{Out}}$,$p_2^{\text{Out}}$ with quadratic and linear shape functions respectively. The solution time was only around 5 min. So with the effective models explained in this thesis we clearly open op for new possibilities to simulate acoustic streaming in 3D.

Chapter 8

Conclusion and outlook

Acoustic streaming is one of the major challenges within the field of acoustofluidics since this phenomena sets a lower limit on the particle size that can be controlled efficiently. A better understanding of this phenomena is therefore important for future engineering of acoustofluidic devices. In this thesis we have developed effective models for calculation of both (i) first order acoustic oscillatory motion and (ii) second order steady acoustic streaming.

The most important contribution in the first-order analysis (i) is a new boundary condition on the acoustic pressure which allows calculations accounting for the significant viscous damping inside the acoustic boundary layer without resolving this region numerically. Compared to previous work[11, 22–24], where it is assumed that $\boldsymbol{n} \cdot \boldsymbol{\nabla} p_1 = 0$ on stationary walls, this new boundary condition gives a much more realistic result and it can be implemented in any system where the boundary layer width δ is the smallest length scale.

In the second part (ii) we combined the limiting velocity theory developed Nyborg[1], Lee[10, 24], and Vanneste[11] and formulated the limiting velocity on a curved surface with *any* wall oscillation as long the wall amplitude is much smaller than δ and the wall curvature is much larger than δ. We then developed a decomposition of the acoustic streaming into the three fields with different physical origin: Inner streaming, outer streaming, and bulk streaming. Whereas outer streaming is always present we formulated a criterion on when to expect bulk streaming. In particular we found a strong relation between the predicted bulk streaming in a square channel and the streaming pattern observed by Hagsäter *et al.*[26] with only one streaming roll per acoustic wave length. This special streaming pattern were found to be related with rotational motion in the fluid set up due to degenerate resonances in perpendicular directions in a symmetric channel. Finally, based on the expression for the limiting velocity we explained how streaming over an oscillating wall can be suppressed in some areas due to gradients in the perpendicular velocity. This phenomena might be interesting for future engineering purposes to efficiently suppress streaming by choosing the right wall oscillation.

As a finishing example we showed in Chapter 7 how we could use the effective models to simulate acoustic streaming in a 3-dimensional system with a sphere in the center. This example establishes the foundation for future simulation of streaming in the acoustic trap as well as other larger 3-dimensional devices.

Appendix A

Curvilinear coodinates

We here derive the curvilinear differential operators used in this thesis. The gradient is

$$\boldsymbol{\nabla} f = \frac{1}{h_\xi}\frac{\partial f}{\partial \xi}\boldsymbol{t}_\xi + \frac{1}{h_\eta}\frac{\partial f}{\partial \eta}\boldsymbol{t}_\eta + \frac{1}{h_\zeta}\frac{\partial f}{\partial \zeta}\boldsymbol{n} \approx \frac{\partial f}{\partial \xi}\boldsymbol{t}_\xi + \frac{\partial f}{\partial \eta}\boldsymbol{t}_\eta + \frac{\partial f}{\partial \zeta}\boldsymbol{n}. \tag{A.1}$$

The divergence is,

$$\begin{aligned}
\boldsymbol{\nabla}\cdot\boldsymbol{A} &= \frac{1}{h_\xi h_\eta h_\zeta}\left(\frac{\partial (A_\xi h_\eta h_\zeta)}{\partial \xi} + \frac{\partial (h_\xi A_\eta h_\zeta)}{\partial \eta} + \frac{\partial (h_\xi h_\eta A_\zeta)}{\partial \zeta}\right) \\
&= \frac{1}{h_\xi h_\eta}\left(\frac{\partial (A_\xi h_\eta)}{\partial \xi} + \frac{\partial (A_\eta h_\xi)}{\partial \eta}\right) + \frac{\partial A_\zeta}{\partial \zeta} + \mathcal{H} A_\zeta. && \text{(A.2a)} \\
&\approx \boldsymbol{\nabla}_\parallel \cdot \boldsymbol{A}_\parallel + \frac{\partial A_\zeta}{\partial \zeta} + \mathcal{H} A_\zeta, && \text{(A.2b)}
\end{aligned}$$

where we have used the parallel divergence $\boldsymbol{\nabla}_\parallel \cdot \boldsymbol{A}_\parallel \equiv \partial_\xi A_\xi + \partial_\eta A_\eta$.
The Laplacian is $\boldsymbol{\nabla}\cdot(\boldsymbol{\nabla} f)$,

$$\begin{aligned}
\nabla^2 f &= \frac{1}{h_\xi h_\eta h_\zeta}\left[\frac{\partial}{\partial \xi}\left(\frac{h_\eta h_\zeta}{h_\xi}\frac{\partial f}{\partial \xi}\right) + \frac{\partial}{\partial \eta}\left(\frac{h_\xi h_\zeta}{h_\eta}\frac{\partial f}{\partial \eta}\right) + \frac{\partial}{\partial \zeta}\left(\frac{h_\xi h_\eta}{h_\zeta}\frac{\partial f}{\partial \zeta}\right)\right] && \text{(A.3a)} \\
&= \frac{1}{h_\xi h_\eta}\left[\frac{\partial}{\partial \xi}\left(\frac{h_\eta}{h_\xi}\frac{\partial f}{\partial \xi}\right) + \frac{\partial}{\partial \eta}\left(\frac{h_\xi}{h_\eta}\frac{\partial f}{\partial \eta}\right) + \frac{\partial}{\partial \zeta}\left(h_\xi h_\eta \frac{\partial f}{\partial \zeta}\right)\right] && \text{(A.3b)} \\
&= \frac{1}{h_\xi^2}\left[\left(\frac{1}{h_\eta}\frac{\partial h_\eta}{\partial \xi} - \frac{1}{h_\xi}\frac{\partial h_\xi}{\partial \xi}\right)\frac{\partial f}{\partial \xi} + \frac{\partial^2 f}{\partial \xi^2}\right] + \frac{1}{h_\eta^2}\left[\left(\frac{1}{h_\xi}\frac{\partial h_\xi}{\partial \eta} - \frac{1}{h_\eta}\frac{\partial h_\eta}{\partial \eta}\right)\frac{\partial f}{\partial \eta} + \frac{\partial^2 f}{\partial \eta^2}\right] \\
&\quad + \frac{\partial^2 f}{\partial \zeta^2} + \mathcal{H}\frac{\partial f}{\partial \zeta}, && \text{(A.3c)} \\
&\approx \frac{\partial^2 f}{\partial \xi^2} + \frac{\partial^2 f}{\partial \eta^2} + \frac{\partial^2 f}{\partial \zeta^2} + \mathcal{H}\frac{\partial f}{\partial \zeta} && \text{(A.3d)}
\end{aligned}$$

In the special case where f varies over length scale δ in ζ and over length scale l in ξ, η, where $l = \min\{\lambda, R\} \gg \delta$ we get to lowest order in ε,

$$\nabla^2 f \approx \frac{\partial^2 f}{\partial \zeta^2} \qquad \text{if } f \text{ varies } \varepsilon \text{ slower in tangential direction than perpendicular.} \tag{A.4}$$

Helmholtz equation in curvilinear coordinates for slow parallel variations

In the special case where f varies slowly with ξ, η we can use the Laplacian in Eq. (A.4) and the Helmholtz equation becomes

$$\frac{\partial^2 f}{\partial \zeta^2} + \mathcal{H}\frac{\partial f}{\partial \zeta} + k^2 f = 0, \tag{A.5}$$

where $\mathcal{H}$ is constant. If $k = k_\mathrm{s}$ we have $k \gg \mathcal{H}$, and the non-growing solution is easily found to be,

$$f = A\exp\left[\left(-\frac{1}{2}\mathcal{H} + \mathrm{i}k_\mathrm{s}\sqrt{1 - \frac{\mathcal{H}^2}{(2k_\mathrm{s})^2}}\right)\zeta\right] \approx A\exp\left[\mathrm{i}k_\mathrm{s}\zeta - \frac{\mathcal{H}}{2}\zeta\right]. \tag{A.6}$$

where the approximation gives the first order solution.

Convective derivative in curvilinear coordinates

In curvilinear coordinates ((ξ, η, ζ) the i-th component of the convective derivative is

$$\boldsymbol{e}_i\cdot[\boldsymbol{A}\cdot\boldsymbol{\nabla}\boldsymbol{B}] = \boldsymbol{e}_i\cdot\left[\left(\frac{A_\xi}{h_\xi}\frac{\partial}{\partial\xi} + \frac{A_\eta}{h_\eta}\frac{\partial}{\partial\eta} + \frac{A_\zeta}{h_\zeta}\frac{\partial}{\partial\zeta}\right)(B_\xi\boldsymbol{e}_\xi + B_\eta\boldsymbol{e}_\eta + B_\zeta\boldsymbol{e}_\zeta)\right] \tag{A.7a}$$

$$= \sum_{k=\xi,\eta,\zeta}\frac{A_k}{h_k}\frac{\partial B_i}{\partial k} + \sum_{j,k=\xi,\eta,\zeta}\frac{A_k}{h_k}B_j\boldsymbol{e}_i\cdot\frac{\partial\boldsymbol{e}_j}{\partial k} \tag{A.7b}$$

$$= \sum_{k=\xi,\eta,\zeta}\frac{A_k}{h_k}\left(\frac{\partial B_i}{\partial k} + \sum_{j=\xi,\eta,\zeta}B_j T_{ijk}\right) \tag{A.7c}$$

with $T_{ijk} \equiv \boldsymbol{e}_i\cdot\dfrac{\partial\boldsymbol{e}_j}{\partial k}$. Using the Frenet-Serret frame with ξ- and η- curves as lines of curvature we get,

$$T_{\zeta\xi\xi} = \kappa_\xi, \qquad T_{\zeta\xi\xi} = \kappa_\eta, \qquad T_{\xi\zeta\xi} = -\kappa_\xi, \qquad T_{\eta\zeta\eta} = -\kappa_\eta, \tag{A.8}$$

and the rest are zero. If we further use that to zeroth order in ε we have $h_\xi = h_\eta = h_\zeta = 1$ we have,

$$\begin{aligned}(\boldsymbol{A}\cdot\boldsymbol{\nabla}\boldsymbol{B})_\parallel = {} & A_\xi\left(\frac{\partial\boldsymbol{B}_\parallel}{\partial\xi} + B_\xi\boldsymbol{T}_{\parallel\xi\xi} + B_\eta\boldsymbol{T}_{\parallel\eta\xi} + B_\zeta\boldsymbol{T}_{\parallel\zeta\xi}\right)\\ & + A_\eta\left(\frac{\partial\boldsymbol{B}_\parallel}{\partial\eta} + B_\xi\boldsymbol{T}_{\parallel\xi\eta} + B_\eta\boldsymbol{T}_{\parallel\eta\eta} + B_\zeta\boldsymbol{T}_{\parallel\zeta\eta}\right)\\ & + A_\zeta\left(\frac{\partial\boldsymbol{B}_\parallel}{\partial\zeta} + B_\xi\boldsymbol{T}_{\parallel\xi\zeta} + B_\eta\boldsymbol{T}_{\parallel\eta\zeta} + B_\zeta\boldsymbol{T}_{\parallel\zeta\zeta}\right)\end{aligned} \tag{A.9a}$$

$$= \boldsymbol{A}_\parallel\cdot\boldsymbol{\nabla}_\parallel\boldsymbol{B}_\parallel + A_\zeta\frac{\partial\boldsymbol{B}_\parallel}{\partial\zeta} - A_\zeta\boldsymbol{Q}_B \tag{A.9b}$$

where $\boldsymbol{Q}_B = (\kappa_\xi B_\xi, \kappa_\eta B_\eta)$ and for the perpendicular component,

$$
\begin{aligned}
(\boldsymbol{A}\cdot\boldsymbol{\nabla}\boldsymbol{B})_\zeta &= A_\xi\left(\frac{\partial B_\zeta}{\partial\xi} + B_\xi T_{\zeta\xi\xi} + B_\eta T_{\zeta\eta\xi} + B_\zeta T_{\zeta\zeta\xi}\right) \\
&+ A_\eta\left(\frac{\partial B_\zeta}{\partial\eta} + B_\xi T_{\zeta\xi\eta} + B_\eta T_{\zeta\eta\eta} + B_\zeta T_{\zeta\zeta\eta}\right) \\
&+ A_\zeta\left(\frac{\partial B_\zeta}{\partial\zeta} + B_\xi T_{\zeta\xi\zeta} + B_\eta T_{\zeta\eta\zeta} + B_\zeta T_{\zeta\zeta\zeta}\right) \qquad \text{(A.10a)} \\
&= \boldsymbol{A}_\parallel\cdot\boldsymbol{\nabla}_\parallel B_\zeta + A_\zeta\frac{\partial B_\zeta}{\partial\zeta} + \boldsymbol{A}_\parallel\cdot\boldsymbol{Q}_B \qquad \text{(A.10b)}
\end{aligned}
$$

In these equations we have used the parallel Nabla-operator which is $\boldsymbol{\nabla}_\parallel \equiv \boldsymbol{t}_\xi\partial_\xi + \boldsymbol{t}_\eta\partial_\eta$.

Appendix B

Evaluation of the limiting velocity

In this chapter we solve for $\boldsymbol{w}_{2\parallel}$ in Eq. (6.28) restated here,

$$\eta\nabla^2\boldsymbol{w}_{2\parallel} \approx \eta\partial_\zeta^2\boldsymbol{w}_{2\parallel} = \rho_0 \left\langle \boldsymbol{\nabla}\cdot(\boldsymbol{v}_1\boldsymbol{v}_1 - \boldsymbol{u}_1\boldsymbol{u}_1)\right\rangle_\parallel , \tag{B.1}$$

with the boundary condition $\boldsymbol{w}_{2\parallel} \to \boldsymbol{0}$ as $\zeta \to \infty$. We then evaluate the boundary condition on $\boldsymbol{u}_2$ (please recall that the total field is $\boldsymbol{v}_2 = \boldsymbol{u}_2 + \boldsymbol{w}_2$),

$$\boldsymbol{u}_2^{\mathrm{Lim}} = -\boldsymbol{w}_2 - \frac{1}{\omega}\left\langle (\mathrm{i}\boldsymbol{v}_1^{\mathrm{s}})\cdot\boldsymbol{\nabla}\boldsymbol{v}_1\right\rangle \qquad \text{at} \quad \zeta = 0. \tag{B.2}$$

We will use the curvilinear versions of the convective derivative given in Eqs. (A.9) and (A.10), where we have assumed a geometry where the surface is locally parametrized by arc length in the parallel ξ, η plane such that the ξ- and η-curves are principal curves of curvature. ζ is thus always the the perpendicular coordinate.

We first evaluate the boundary condition Eq. (B.2),

$$\frac{1}{\omega}\left\langle (\mathrm{i}\boldsymbol{v}^{\mathrm{s}})\cdot\boldsymbol{\nabla}\boldsymbol{v}_1\right\rangle_\parallel = \frac{1}{\omega}\left\langle \mathrm{i}\boldsymbol{v}_{1\parallel}^{\mathrm{s}}\cdot\boldsymbol{\nabla}_\parallel\boldsymbol{v}_{1\parallel}^{\mathrm{s}} + \mathrm{i}v_{1\zeta}^{\mathrm{s}}\partial_\zeta\boldsymbol{v}_{1\parallel} - \mathrm{i}v_{1\zeta}^{\mathrm{s}}\boldsymbol{Q}_{v^{\mathrm{s}}}\right\rangle \tag{B.3a}$$

$$= \frac{1}{4\omega}\mathrm{Re}\left\{2\mathrm{i}\left(\boldsymbol{v}_{1\parallel}^{\mathrm{s}}\cdot\boldsymbol{\nabla}_\parallel(\boldsymbol{v}_{1\parallel}^{\mathrm{s}})^* + (v_{1\zeta}^{\mathrm{s}})^*\boldsymbol{Q}_{v^{\mathrm{s}}}\right) - v_{1\zeta}^{\mathrm{s}}\tilde{\boldsymbol{u}}_{1\parallel}^*\frac{2-2\mathrm{i}}{\delta}\right\} \tag{B.3b}$$

$$\frac{1}{\omega}\left\langle (\mathrm{i}\boldsymbol{v}^{\mathrm{s}})\cdot\boldsymbol{\nabla}\boldsymbol{v}_1\right\rangle_\zeta = \frac{1}{\omega}\left\langle \mathrm{i}\boldsymbol{v}_{1\parallel}^{\mathrm{s}}\cdot\boldsymbol{\nabla}_\parallel v_{1\zeta}^{\mathrm{s}} + \mathrm{i}v_{1\zeta}^{\mathrm{s}}\partial_\zeta v_{1\zeta} + \mathrm{i}\boldsymbol{v}_{1\parallel}^{\mathrm{s}}\cdot\boldsymbol{Q}_{v^{\mathrm{s}}}\right\rangle \tag{B.3c}$$

$$= \frac{1}{4\omega}\mathrm{Re}\left\{2\mathrm{i}\left(\boldsymbol{v}_{1\parallel}^{\mathrm{s}}\cdot\boldsymbol{\nabla}_\parallel(v_{1\zeta}^{\mathrm{s}})^* - (v_{1\zeta}^{\mathrm{s}})^*\left(\boldsymbol{\nabla}_\parallel\cdot\tilde{\boldsymbol{u}}_{1\parallel} + \partial_\zeta u_{1\zeta}\right)\right)\right\} \tag{B.3d}$$

$$= \frac{1}{4\omega}\mathrm{Re}\left\{2\mathrm{i}\left(\boldsymbol{\nabla}_\parallel\cdot\left[(v_{1\zeta}^{\mathrm{s}})^*\boldsymbol{v}_{1\parallel}^{\mathrm{s}}\right] - (v_{1\zeta}^{\mathrm{s}})^*\boldsymbol{\nabla}\cdot\boldsymbol{u}_1\right)\right\} \tag{B.3e}$$

where we have used that $\mathrm{Re}\left\{\mathrm{i}\boldsymbol{v}_{1\parallel}^{\mathrm{s}}\cdot\boldsymbol{Q}_{v^{\mathrm{s}}}\right\} = 0$.

We then evaluate the source term,

$$\left\langle \boldsymbol{\nabla}\cdot(\boldsymbol{v}_1\boldsymbol{v}_1 - \boldsymbol{u}_1\boldsymbol{u}_1)\right\rangle_\parallel = \left\langle \boldsymbol{w}_1\cdot\boldsymbol{\nabla}\boldsymbol{u}_1 + \boldsymbol{w}_1\boldsymbol{\nabla}\cdot\boldsymbol{u}_1 + \boldsymbol{v}_1\cdot\boldsymbol{\nabla}\boldsymbol{w}_1\right\rangle_\parallel \tag{B.4}$$

The first term is (with $f \equiv \mathrm{e}^{\mathrm{i}k_\mathrm{s}\zeta}$)

$$\langle \boldsymbol{w}_1 \cdot \boldsymbol{\nabla} \boldsymbol{u}_1 \rangle_\parallel \approx \left\langle \boldsymbol{w}_{1\parallel} \cdot \boldsymbol{\nabla}_\parallel \boldsymbol{u}_{1\parallel} - v^\mathrm{s}_{1\zeta} \boldsymbol{Q}_w \right\rangle \tag{B.5a}$$

$$= \left\langle -(\tilde{\boldsymbol{u}}_{1\parallel} f) \cdot \boldsymbol{\nabla}_\parallel \boldsymbol{u}_{1\parallel} + v^\mathrm{s}_{1\zeta} \boldsymbol{Q}_{\tilde{u}} f \right\rangle \tag{B.5b}$$

$$= \frac{1}{2}\mathrm{Re}\left\{ -\tilde{\boldsymbol{u}}_{1\parallel} \cdot \boldsymbol{\nabla}_\parallel \tilde{\boldsymbol{u}}^*_{1\parallel} f - \tilde{\boldsymbol{u}}_{1\parallel} \cdot \boldsymbol{\nabla}_\parallel (\boldsymbol{v}^\mathrm{s}_{1\parallel})^* f + (v^\mathrm{s}_{1\zeta})^* \boldsymbol{Q}_{\tilde{u}} f \right\} \tag{B.5c}$$

Here we have used that $w_{1\zeta} \ll w_{1\parallel}$ and that $u_{1\zeta} \approx v^\mathrm{s}_{1\zeta}$ inside the boundary layer. The second term is

$$\langle \boldsymbol{w}_1 \boldsymbol{\nabla} \cdot \boldsymbol{u}_1 \rangle_\parallel = \left\langle -(\tilde{\boldsymbol{u}}_{1\parallel} f) \boldsymbol{\nabla} \cdot \boldsymbol{u}_1 \right\rangle \tag{B.6a}$$

$$= \frac{1}{2}\mathrm{Re}\left\{ -\tilde{\boldsymbol{u}}^*_{1\parallel} \boldsymbol{\nabla} \cdot \boldsymbol{u}_1 f^* \right\}, \tag{B.6b}$$

$$\approx \frac{1}{2}\mathrm{Re}\left\{ -\tilde{\boldsymbol{u}}^*_{1\parallel} \left(\boldsymbol{\nabla}_\parallel \cdot \tilde{\boldsymbol{u}}_{1\parallel} + \boldsymbol{\nabla}_\parallel \cdot \boldsymbol{v}^\mathrm{s}_{1\parallel} + \partial_\zeta u_{1\zeta} + \mathcal{H}_0 v^\mathrm{s}_{1\zeta} \right) f^* \right\}. \tag{B.6c}$$

Finally the third term becomes,

$$\langle \boldsymbol{v}_1 \cdot \nabla \boldsymbol{w}_1 \rangle_\parallel \approx \left\langle \boldsymbol{v}_{1\parallel} \cdot \boldsymbol{\nabla}_\parallel \boldsymbol{w}_{1\parallel} + v_{1\zeta} \frac{\partial \boldsymbol{w}_{1\parallel}}{\partial \zeta} \right\rangle \tag{B.7a}$$

$$= \left\langle -(\boldsymbol{v}^\mathrm{s}_{1\parallel} + \tilde{\boldsymbol{u}}_{1\parallel}(1-f)) \cdot \boldsymbol{\nabla}_\parallel (\tilde{\boldsymbol{u}}_{1\parallel} f) - \left(v^\mathrm{s}_{1\zeta} + \zeta \partial_\zeta u_{1\zeta} - \boldsymbol{\nabla}_\parallel \cdot \tilde{\boldsymbol{u}}_{1\parallel} \frac{1-f}{\mathrm{i}k_\mathrm{s}} \right) \left(\tilde{\boldsymbol{u}}_{1\parallel} (\mathrm{i}k_\mathrm{s} f) \right) \right\rangle \tag{B.7b}$$

$$= \frac{1}{2}\mathrm{Re}\Big\{ - \boldsymbol{v}^\mathrm{s}_{1\parallel} \cdot \boldsymbol{\nabla}_\parallel \tilde{\boldsymbol{u}}^*_{1\parallel} f^* - \tilde{\boldsymbol{u}}_{1\parallel} \cdot \boldsymbol{\nabla}_\parallel \tilde{\boldsymbol{u}}^*_{1\parallel} (1-f) f^* - \tilde{\boldsymbol{u}}^*_{1\parallel} \left[\zeta \partial_\zeta u_{1\zeta} - \boldsymbol{\nabla}_\parallel \cdot \tilde{\boldsymbol{u}}_{1\parallel} \frac{1-f}{\mathrm{i}k_\mathrm{s}} \right] (\mathrm{i}k_\mathrm{s} f)^*$$
$$- \tilde{\boldsymbol{u}}^*_{1\parallel} v^\mathrm{s}_{1\zeta} (\mathrm{i}k_\mathrm{s} f)^* \Big\}, \tag{B.7c}$$

where we have again used that $w_{1\zeta} \ll w_{1\parallel}$. Please note that the last term is $\mathcal{O}(\varepsilon^{-1})$ larger than the other terms. However it will be exactly cancelled when evaluating $\boldsymbol{u}^\mathrm{Lim}_{2\parallel}$. In total we get,

$$\langle \boldsymbol{\nabla} \cdot (\boldsymbol{v}_1 \boldsymbol{v}_1 - \boldsymbol{u}_1 \boldsymbol{u}_1) \rangle_\parallel$$
$$= \frac{1}{2}\mathrm{Re}\Big\{ - \tilde{\boldsymbol{u}}_{1\parallel} \cdot \boldsymbol{\nabla}_\parallel \tilde{\boldsymbol{u}}^*_{1\parallel} \left(f + (1-f) f^* \right) - \tilde{\boldsymbol{u}}^*_{1\parallel} \left[\partial_\zeta u_{1\zeta} \left(1 + \zeta((\mathrm{i}k_\mathrm{s})^*) \right) f^* + \boldsymbol{\nabla}_\parallel \cdot \tilde{\boldsymbol{u}}_{1\parallel} \left(f^* - \frac{1-f}{\mathrm{i}k_\mathrm{s}} (\mathrm{i}k_\mathrm{s} f)^* \right) \right]$$
$$- \left[\tilde{\boldsymbol{u}}^*_{1\parallel} \left(\mathcal{H}_0 v^\mathrm{s}_{1\zeta} + \boldsymbol{\nabla}_\parallel \cdot \boldsymbol{v}^\mathrm{s}_{1\parallel} \right) + \boldsymbol{v}^\mathrm{s}_{1\parallel} \cdot \boldsymbol{\nabla}_\parallel \tilde{\boldsymbol{u}}^*_{1\parallel} \right] f^* - \left[\tilde{\boldsymbol{u}}_{1\parallel} \cdot \boldsymbol{\nabla}_\parallel (\boldsymbol{v}^\mathrm{s}_{1\parallel})^* - (v^\mathrm{s}_{1\zeta})^* \boldsymbol{Q}_{\tilde{u}} \right] f - \tilde{\boldsymbol{u}}^*_{1\parallel} v^\mathrm{s}_{1\zeta} (\mathrm{i}k_\mathrm{s} f)^* \Big\}. \tag{B.8a}$$

It now becomes convenient to define the functions,

$$N_1 = -\left(f + (1-f)f^*\right), \tag{B.9a}$$
$$N_2 = -\left(1 + \zeta(\mathrm{i}k_\mathrm{s})^*\right) f^* \tag{B.9b}$$
$$N_3 = -\left(f^* - \frac{1-f}{\mathrm{i}k_\mathrm{s}}(\mathrm{i}k_\mathrm{s}f)^*\right) \tag{B.9c}$$
$$N_4 = -f^*, \tag{B.9d}$$
$$N_5 = -f, \tag{B.9e}$$
$$N_6 = -(\mathrm{i}k_\mathrm{s}f)^*. \tag{B.9f}$$

Please note that N_6 is δ^{-1} larger than N_{1-5}. The source term now becomes

$$\langle \boldsymbol{\nabla}\cdot(\boldsymbol{v}_1\boldsymbol{v}_1 - \boldsymbol{u}_1\boldsymbol{u}_1)\rangle_\parallel = \frac{1}{2}\mathrm{Re}\Big\{ \tilde{\boldsymbol{u}}_{1\parallel}\cdot\boldsymbol{\nabla}_\parallel\tilde{\boldsymbol{u}}^*_{1\parallel}N_1 + \tilde{\boldsymbol{u}}^*_{1\parallel}\left[\partial_\zeta u_{1\zeta}N_2 + \boldsymbol{\nabla}_\parallel\cdot\tilde{\boldsymbol{u}}_{1\parallel}N_3\right]$$
$$+ \left[\tilde{\boldsymbol{u}}^*_{1\parallel}\left(\mathcal{H}_0 v^\mathrm{s}_{1\zeta} + \boldsymbol{\nabla}_\parallel\cdot\boldsymbol{v}^\mathrm{s}_{1\parallel}\right) + \boldsymbol{v}^\mathrm{s}_{1\parallel}\cdot\boldsymbol{\nabla}_\parallel\tilde{\boldsymbol{u}}^*_{1\parallel}\right]N_4 + \left[\tilde{\boldsymbol{u}}_{1\parallel}\cdot\boldsymbol{\nabla}_\parallel(\boldsymbol{v}^\mathrm{s}_{1\parallel})^* - (v^\mathrm{s}_{1\zeta})^*\boldsymbol{Q}_{\tilde{u}}\right]N_5 + \tilde{\boldsymbol{u}}^*_{1\parallel}v^\mathrm{s}_{1\zeta}N_6\Big\}. \tag{B.10}$$

We can now integrate

$$\frac{\partial^2\boldsymbol{w}_{2\parallel}}{\partial\tilde{\zeta}^2} = \frac{2}{\omega}\left\langle \boldsymbol{w}_1\cdot\boldsymbol{\nabla}\boldsymbol{u}_1 + \boldsymbol{w}_1\boldsymbol{\nabla}\cdot\boldsymbol{u}_1 + \boldsymbol{v}_1\cdot\boldsymbol{\nabla}\boldsymbol{w}_1\right\rangle_\parallel, \tag{B.11}$$

where we have defined $\tilde{\zeta} = \zeta/\delta$. We choose integrations constants such that $\boldsymbol{w}_{1\parallel} \to \infty$ as $\zeta \to \infty$. Since all the ζ-dependence is contained in the $N_i(\zeta)$ we only need to integrate these. We use the notation,

$$n_i = \int\int N_i(\tilde{\zeta})\mathrm{d}\tilde{\zeta}\mathrm{d}\tilde{\zeta}, \tag{B.12}$$

without explicitly evaluating n_i here. The solution is then

$$\boldsymbol{w}_{2\parallel} = \frac{1}{\omega}\mathrm{Re}\Big\{ \tilde{\boldsymbol{u}}_{1\parallel}\cdot\boldsymbol{\nabla}_\parallel\tilde{\boldsymbol{u}}^*_{1\parallel}n_1 + \tilde{\boldsymbol{u}}^*_{1\parallel}\left[\partial_\zeta u_{1\zeta}n_2 + \boldsymbol{\nabla}_\parallel\cdot\tilde{\boldsymbol{u}}_{1\parallel}n_3\right]$$
$$+ \left[\tilde{\boldsymbol{u}}^*_{1\parallel}\left(\mathcal{H}_0 v^\mathrm{s}_{1\zeta} + \boldsymbol{\nabla}_\parallel\cdot\boldsymbol{v}^\mathrm{s}_{1\parallel}\right) + \boldsymbol{v}^\mathrm{s}_{1\parallel}\cdot\boldsymbol{\nabla}_\parallel\tilde{\boldsymbol{u}}^*_{1\parallel}\right]n_4 + \left[\tilde{\boldsymbol{u}}_{1\parallel}\cdot\boldsymbol{\nabla}_\parallel(\boldsymbol{v}^\mathrm{s}_{1\parallel})^* - (v^\mathrm{s}_{1\zeta})^*\boldsymbol{Q}_{\tilde{u}}\right]n_5 + \tilde{\boldsymbol{u}}^*_{1\parallel}v^\mathrm{s}_{1\zeta}n_6\Big\}, \tag{B.13}$$

which should now be evaluated at $\zeta = 0$,

$$\boldsymbol{w}_{2\parallel}(\zeta=0) = \frac{1}{4\omega}\mathrm{Re}\Big\{ \tilde{\boldsymbol{u}}_{1\parallel}\cdot\boldsymbol{\nabla}_\parallel\tilde{\boldsymbol{u}}^*_{1\parallel} + \tilde{\boldsymbol{u}}^*_{1\parallel}\left[\partial_\zeta u_{1\zeta}(-2\mathrm{i}) + \boldsymbol{\nabla}_\parallel\cdot\tilde{\boldsymbol{u}}_{1\parallel}(2+\mathrm{i})\right]$$
$$+ \left[\tilde{\boldsymbol{u}}^*_{1\parallel}\left(\mathcal{H}_0 v^\mathrm{s}_{1\zeta} + \boldsymbol{\nabla}_\parallel\cdot\boldsymbol{v}^\mathrm{s}_{1\parallel}\right) + \boldsymbol{v}^\mathrm{s}_{1\parallel}\cdot\boldsymbol{\nabla}_\parallel\tilde{\boldsymbol{u}}^*_{1\parallel}\right](2\mathrm{i}) + \left[\tilde{\boldsymbol{u}}_{1\parallel}\cdot\boldsymbol{\nabla}_\parallel(\boldsymbol{v}^\mathrm{s}_{1\parallel})^* - (v^\mathrm{s}_{1\zeta})^*\boldsymbol{Q}_{\tilde{u}}\right](-2\mathrm{i}) + \tilde{\boldsymbol{u}}^*_{1\parallel}v^\mathrm{s}_{1\zeta}\frac{2-2\mathrm{i}}{\delta}\Big\}. \tag{B.14}$$

The perpendicular velocity

This section is an attempt to estimate the perpendicular velocity better. However, the result of this section seem to be wrong.

To find the perpendicular component $w_{2\zeta}$ we use the continuity equation,

$$\boldsymbol{\nabla}\cdot\boldsymbol{w}_2 = \boldsymbol{\nabla}_\parallel\cdot\boldsymbol{w}_{2\parallel} + \partial_\zeta w_{2\zeta} + H_0 w_{2\zeta} = -\frac{1}{\rho_0}\left\langle \boldsymbol{w}_1\cdot\boldsymbol{\nabla}\rho_1\right\rangle . \tag{B.15}$$

Since the variations of $\boldsymbol{w}_2$ are much faster in the ζ direction than in the parallel direction we have $\partial_\zeta w_{2\zeta} \gg \mathcal{H}_0 w_{2\zeta}$. So we can find $w_{2\zeta}$ from integration,

$$w_{2\zeta} = -\int \boldsymbol{\nabla}_\parallel\cdot\boldsymbol{w}_{2\parallel}\,\mathrm{d}\zeta - \frac{1}{\rho_0}\int \left\langle \boldsymbol{w}_1\cdot\boldsymbol{\nabla}\rho_1\right\rangle \,\mathrm{d}\zeta, \tag{B.16}$$

and use $w_{2\zeta}\to 0$ as $\zeta\to\infty$. The first term involves integration of the n_i-functions where in each integration we use $w_{2\zeta}\to 0$ as $\zeta\to\infty$. Hence the first term is,

$$\begin{aligned}
&-\int \boldsymbol{\nabla}_\parallel\cdot\boldsymbol{w}_2\,\mathrm{d}\zeta = -\boldsymbol{\nabla}_\parallel\cdot\int \boldsymbol{w}_2\,\mathrm{d}\zeta\\
&= -\delta\boldsymbol{\nabla}_\parallel\cdot\left[\frac{1}{\omega}\mathrm{Re}\left\{\tilde{\boldsymbol{u}}_{1\parallel}\cdot\boldsymbol{\nabla}_\parallel\tilde{\boldsymbol{u}}^*_{1\parallel}\left(-\frac{5}{8}\right) + \tilde{\boldsymbol{u}}^*_{1\parallel}\left[\partial_\zeta u_{1\zeta}\left(\frac{1+\mathrm{i}}{2}\right) + \boldsymbol{\nabla}_\parallel\cdot\tilde{\boldsymbol{u}}_{1\parallel}\left(\frac{-4+\mathrm{i}}{8}\right)\right]\right.\right.\\
&+\left[\tilde{\boldsymbol{u}}^*_{1\parallel}\left(\mathcal{H}_0 v^{\mathrm{s}}_{1\zeta} + \boldsymbol{\nabla}_\parallel\cdot\boldsymbol{v}^{\mathrm{s}}_{1\parallel}\right) + \boldsymbol{v}^{\mathrm{s}}_{1\parallel}\cdot\boldsymbol{\nabla}_\parallel\tilde{\boldsymbol{u}}^*_{1\parallel}\right]\left(\frac{-1-\mathrm{i}}{4}\right)\\
&\left.\left.+\left[\tilde{\boldsymbol{u}}_{1\parallel}\cdot\boldsymbol{\nabla}_\parallel(\boldsymbol{v}^{\mathrm{s}}_{1\parallel})^* - (v^{\mathrm{s}}_{1\zeta})^*\boldsymbol{Q}_{\tilde{u}}\right]\left(\frac{-1+\mathrm{i}}{4}\right) + \tilde{\boldsymbol{u}}^*_{1\parallel}v^{\mathrm{s}}_{1\zeta}\left(\frac{\mathrm{i}}{2\delta}\right)\right\}\right]
\end{aligned} \tag{B.17a}$$

We note that the very last term here is much larger than all the others. So if there is a perpendicular velocity $v^{\mathrm{s}}_{1\zeta}$ this term is completely dominating,

$$w_{2\zeta} = -\frac{1}{4\omega}\mathrm{Re}\left\{2\mathrm{i}\boldsymbol{\nabla}_\parallel\cdot\left[\tilde{\boldsymbol{u}}^*_{1\parallel}v^{\mathrm{s}}_{1\zeta}\right]\right\} \qquad \text{on walls with } v^{\mathrm{s}}_{1\zeta}\neq 0. \tag{B.18}$$

On walls with no perpendicular velocity we have from Eq. (5.6) that $u_{1\zeta} \ll \left|\boldsymbol{u}_{1\parallel}\right|$. To proceed in a not too complicated way we need to assume that the parallel velocity of the wall $\boldsymbol{v}^{\mathrm{s}}_{1\parallel}$ is also small compared to $\boldsymbol{u}_{1\parallel}$. In that case we can evaluate Eq. (B.17) with $\boldsymbol{v}^{\mathrm{s}}_1 \approx \boldsymbol{0}$ giving

$$-\int \boldsymbol{\nabla}_\parallel\cdot\boldsymbol{w}_2\,\mathrm{d}\zeta = -\delta\boldsymbol{\nabla}_\parallel\cdot\left[\frac{1}{\omega}\mathrm{Re}\left\{\boldsymbol{u}_{1\parallel}\cdot\boldsymbol{\nabla}_\parallel\boldsymbol{u}^*_{1\parallel}\left(-\frac{5}{8}\right) + \boldsymbol{u}^*_{1\parallel}\left[\boldsymbol{\nabla}_\parallel\cdot\boldsymbol{u}_{1\parallel}\left(\frac{-4+\mathrm{i}}{8}\right)\right]\right\}\right] \qquad \text{for } \boldsymbol{v}^{\mathrm{s}}_1 \ll \boldsymbol{u}_{1\parallel} \tag{B.19a}$$

We will now evaluate this in terms of the lowest derivatives as possible for numerical reasons. From Eq. (5.6) we have $\boldsymbol{\nabla}_\parallel\cdot\boldsymbol{u}_{1\parallel} = -\mathrm{i}k_{\mathrm{s}}u_{1\zeta}$. Each term is then found using index

notation with $i,j \in \xi,\eta$

$$\begin{aligned}\boldsymbol{\nabla}_\parallel\cdot\mathrm{Re}\left\{(\boldsymbol{u}_{1\parallel}\cdot\boldsymbol{\nabla}_\parallel\boldsymbol{u}_{1\parallel}^*)\right\} &= \partial_i\mathrm{Re}\left\{(u_j\partial_j u_i^*)\right\} = \mathrm{Re}\left\{(\partial_i u_j)(\partial_j u_i^*) + u_j\partial_j\partial_i u_i^*\right\}\\ &= \frac{1}{2}\left|\boldsymbol{\nabla}_\parallel\boldsymbol{u}_{1\parallel}\right|^2 - \mathrm{Re}\left\{\boldsymbol{u}_{1\parallel}^*\cdot\boldsymbol{\nabla}_\parallel(\mathrm{i}k_\mathrm{s}u_{1\zeta})\right\}, \qquad \text{(B.20a)}\\ \boldsymbol{\nabla}_\parallel\cdot(\boldsymbol{u}_{1\parallel}^*\boldsymbol{\nabla}_\parallel\cdot\boldsymbol{u}_{1\parallel}) &= -\partial_i[u_i^*(\mathrm{i}k_\mathrm{s}u_{1\zeta})] = |k_\mathrm{s}u_{1\zeta}|^2 - [\boldsymbol{u}_{1\parallel}^*\cdot\boldsymbol{\nabla}_\parallel(\mathrm{i}k_\mathrm{s}u_{1\zeta})] \qquad \text{(B.20b)}\end{aligned}$$

In total we have

$$\begin{aligned}-\int\boldsymbol{\nabla}_\parallel\cdot\boldsymbol{w}_2\,\mathrm{d}\zeta &= -\frac{\delta}{\omega}\left(\frac{-5}{16}\left|\boldsymbol{\nabla}_\parallel\boldsymbol{u}_{1\parallel}\right|^2 - \mathrm{Re}\left\{\frac{-5+(-4+\mathrm{i})}{8}[\boldsymbol{u}_{1\parallel}^*\cdot\boldsymbol{\nabla}_\parallel(\mathrm{i}k_\mathrm{s}u_{1\zeta})]\right\} + \mathrm{Re}\left\{\frac{-4+\mathrm{i}}{8}\left|k_\mathrm{s}u_{1\zeta}\right|^2\right\}\right)\\ &= \frac{\delta}{4\omega}\left(\frac{5}{4}\left|\boldsymbol{\nabla}_\parallel\boldsymbol{u}_{1\parallel}\right|^2 - \mathrm{Re}\left\{\frac{9-\mathrm{i}}{2}[\boldsymbol{u}_{1\parallel}^*\cdot\boldsymbol{\nabla}_\parallel(\mathrm{i}k_\mathrm{s}u_{1\zeta})]\right\} + 2\left|k_\mathrm{s}u_{1\zeta}\right|^2\right), \qquad \text{(B.21a)}\end{aligned}$$

which is valid for no wall oscillations. Finally we evaluate the last term in Eq. (B.16) again with no wall velocity,

$$\begin{aligned}-\frac{1}{\rho_0}\int\langle\boldsymbol{w}_1\cdot\boldsymbol{\nabla}\rho_1\rangle\,\mathrm{d}\zeta &\approx \frac{\omega}{c_0^2}\int\left\langle(\boldsymbol{u}_{1\parallel}\mathrm{e}^{\mathrm{i}k_\mathrm{s}\zeta}\cdot(\mathrm{i}\boldsymbol{u}_{1\parallel})\right\rangle\mathrm{d}\zeta = -\frac{k_0^2\delta}{2\omega}\left\langle(1+\mathrm{i})\boldsymbol{u}_{1\parallel}\cdot(\mathrm{i}\boldsymbol{u}_{1\parallel})\right\rangle\\ &= -\frac{k_0^2\delta}{4\omega}\left|\boldsymbol{u}_{1\parallel}\right|^2 \qquad \text{(B.22a)}\end{aligned}$$

Eq. (B.16) now becomes,

$$w_{2\zeta}|_{\zeta=0} = \frac{\delta}{4\omega}\left[\frac{5}{4}\left|\boldsymbol{\nabla}_\parallel\boldsymbol{u}_{1\parallel}\right|^2 + 2\left|k_\mathrm{s}u_{1\zeta}\right|^2 - k_0^2\left|\boldsymbol{u}_{1\parallel}\right|^2 - \mathrm{Re}\left\{\frac{9-\mathrm{i}}{2}[\boldsymbol{u}_{1\parallel}^*\cdot\boldsymbol{\nabla}_\parallel(\mathrm{i}k_\mathrm{s}u_{1\zeta})]\right\}\right] \qquad \text{(B.23a)}$$

Total limiting velocity

In conclusion we get at $\zeta = 0$,

$$\begin{aligned}\boldsymbol{u}_{2\parallel}^{\mathrm{Lim}} &= -\boldsymbol{w}_{2\parallel} - \frac{1}{\omega}\left\langle\mathrm{i}\boldsymbol{v}^\mathrm{s}\cdot\boldsymbol{\nabla}\boldsymbol{v}_1\right\rangle_\parallel \qquad \text{(B.24a)}\\ &= -\frac{1}{4\omega}\mathrm{Re}\Big\{\tilde{\boldsymbol{u}}_{1\parallel}\cdot\boldsymbol{\nabla}_\parallel\tilde{\boldsymbol{u}}_{1\parallel}^* + \tilde{\boldsymbol{u}}_{1\parallel}^*\left[\partial_\zeta u_{1\zeta}(-2\mathrm{i}) + \boldsymbol{\nabla}_\parallel\cdot\tilde{\boldsymbol{u}}_{1\parallel}(2+\mathrm{i})\right]\\ &+ \left[\tilde{\boldsymbol{u}}_{1\parallel}^*\left(\mathcal{H}_0 v_{1\zeta}^\mathrm{s} + \boldsymbol{\nabla}_\parallel\cdot\boldsymbol{v}_{1\parallel}^\mathrm{s}\right) + \boldsymbol{v}_{1\parallel}^\mathrm{s}\cdot\boldsymbol{\nabla}_\parallel\tilde{\boldsymbol{u}}_{1\parallel}^*\right](2\mathrm{i}) + \left[\tilde{\boldsymbol{u}}_{1\parallel}\cdot\boldsymbol{\nabla}_\parallel(\boldsymbol{v}_{1\parallel}^\mathrm{s})^* - (v_{1\zeta}^\mathrm{s})^*\boldsymbol{Q}_{\tilde{u}}\right](-2\mathrm{i})\\ &+ \left(\boldsymbol{v}_{1\parallel}^\mathrm{s}\cdot\boldsymbol{\nabla}_\parallel(\boldsymbol{v}_{1\parallel}^\mathrm{s})^* + (v_{1\zeta}^\mathrm{s})^*\boldsymbol{Q}_{v^\mathrm{s}}\right)(2\mathrm{i})\Big\} \qquad \text{(B.24b)}\\ &= -\frac{1}{4\omega}\mathrm{Re}\Big\{\tilde{\boldsymbol{u}}_{1\parallel}\cdot\boldsymbol{\nabla}_\parallel\tilde{\boldsymbol{u}}_{1\parallel}^* + \tilde{\boldsymbol{u}}_{1\parallel}^*\left[\boldsymbol{\nabla}_\parallel\cdot\tilde{\boldsymbol{u}}_{1\parallel}(2+\mathrm{i}) + (\mathcal{H}_0 v_{1\zeta}^\mathrm{s} + \boldsymbol{\nabla}_\parallel\cdot\boldsymbol{v}_{1\parallel}^\mathrm{s} - \partial_\zeta u_{1\zeta})(2\mathrm{i})\right]\\ &+ (2\mathrm{i})\left[(v_{1\zeta}^\mathrm{s})^*\boldsymbol{Q}_u + \boldsymbol{v}_{1\parallel}^\mathrm{s}\cdot\boldsymbol{\nabla}_\parallel\boldsymbol{u}_{1\parallel}^* - \boldsymbol{u}_{1\parallel}\cdot\boldsymbol{\nabla}_\parallel(\boldsymbol{v}_{1\parallel}^\mathrm{s})^* + \boldsymbol{v}_{1\parallel}^\mathrm{s}\cdot\boldsymbol{\nabla}_\parallel(\boldsymbol{v}_{1\parallel}^\mathrm{s})^*\right]\Big\}, \qquad \text{(B.24c)}\end{aligned}$$

where we have used that $\mathrm{Re}\{\mathrm{i}AB^*\} = \mathrm{Re}\{-\mathrm{i}A^*B\}$. The perpendicular component is,

$$u_{2\zeta}^{\mathrm{Lim}} = -w_{2\zeta} - \frac{1}{\omega}\left\langle (\mathrm{i}\boldsymbol{v}^{\mathrm{s}})\cdot\boldsymbol{\nabla}\boldsymbol{v}_1\right\rangle_\zeta \tag{B.25a}$$

$$= -\frac{1}{4\omega}\mathrm{Re}\left\{2\mathrm{i}\left(\boldsymbol{\nabla}_\parallel\cdot[(v_{1\zeta}^{\mathrm{s}})^*\tilde{\boldsymbol{u}}_{1\parallel}] + \boldsymbol{\nabla}_\parallel\cdot\left[(v_{1\zeta}^{\mathrm{s}})^*\boldsymbol{v}_{1\parallel}^{\mathrm{s}}\right] - (v_{1\zeta}^{\mathrm{s}})^*\boldsymbol{\nabla}\cdot\boldsymbol{u}_1\right)\right\} \tag{B.25b}$$

$$= -\frac{1}{4\omega}\mathrm{Re}\left\{2\mathrm{i}\left(\boldsymbol{u}_{1\parallel}\cdot\boldsymbol{\nabla}_\parallel(v_{1\zeta}^{\mathrm{s}})^* + v_{1\zeta}^{\mathrm{s}}\partial_\zeta u_{1\zeta}^*\right)\right\} \tag{B.25c}$$

Appendix C

Perpendicular surface oscillations

The last term in Eq. (6.30) arises due to the term $\rho_0 \langle v_{1\zeta} \partial_\zeta \boldsymbol{w}_{1\parallel} \rangle$ in the force density $\rho_0 \boldsymbol{\nabla} \cdot \langle \boldsymbol{v}_1 \boldsymbol{v}_1 \rangle$. The physical origin of this term can be seen by considering the amount of x-momentum leaving an infinitesimal volume inside the boundary layer. Integrating over

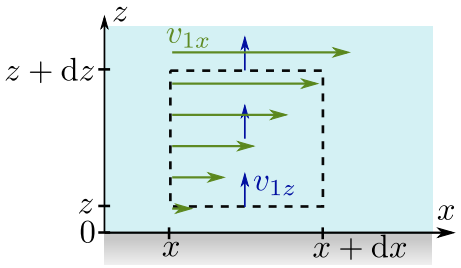

Figure C.1: Sketch of parallel momentum flux in the boundary layer. x-momentum (green) is transported out of the dashed Gaussian box by the perpendicular velocity v_{1z} (blue). For simplicity there are no variations in v_{1z} and no parallel variations in v_{1x}.

a small Gaussian box as in Fig. C.1 we find

$$\oint (\rho_0 v_{1x}) \boldsymbol{v}_1 \cdot \mathrm{d}\boldsymbol{a} \approx \rho_0 \left[v_{1x}(z + \mathrm{d}z) - v_{1x}(z) \right] v_{1z} \, \mathrm{d}x \, \mathrm{d}y = \rho_0 v_{1z} \partial_z v_{1x} \, \mathrm{d}V, \tag{C.1}$$

where we for simplicity have assumed no variations in v_{1z} within the boundary layer and no perpendicular variations in v_{1x}. From this we see that $\langle (\rho_0 v_{1\zeta}) \partial_\zeta \boldsymbol{w}_{1\parallel} \rangle$ is the parallel momentum flux density

is the parallel momentum density transported in the perpendicular direction by $v_{1\zeta}$. This large transport of parallel momentum gives a large force density $\rho_0 \boldsymbol{\nabla} \cdot (\langle \boldsymbol{v}_1 \boldsymbol{v}_1 \rangle)$ close to the surface and therefore a large $\boldsymbol{w}_{2\parallel}(\zeta = 0)$.
However, there is something not so physical here. How can we ensure no *particle* flux through the surface if there is a large perpendicular velocity close to the surface? What we forgot here is that the *physical* surface will move with $v_{1\zeta}^{\mathrm{s}}$ and so the velocity profile (green arrows in Fig. C.1) in the boundary layer will move accordingly. We should instead

think of the time averaged *particle* velocity given in Eq. (2.25),

$$\boldsymbol{v}_2^{\mathrm{L}} = \boldsymbol{v}_2 + \langle \boldsymbol{r}_1 \cdot \boldsymbol{\nabla} \boldsymbol{v}_1 \rangle \,, \tag{C.2}$$

where it turns out that the last term exactly cancels $\left\langle (\rho_0 v_{1\zeta}) \partial_\zeta \boldsymbol{w}_{1\parallel} \right\rangle$ (see the appendix around Eq. (B.3b) for details).

We have here learned that the *Eulerian* streaming velocity can be very large over a perpendicularly oscillating surface. However the more physical velocity to consider in second order is the *particle velocity* which is not so large. As we will see in the following when evaluating the limiting velocity $\boldsymbol{u}_2^{\mathrm{Lim}} \equiv -\boldsymbol{w}_2(\zeta = 0) - \left\langle \frac{\mathrm{i}}{\omega} \boldsymbol{v}_1 \cdot \boldsymbol{\nabla} \boldsymbol{v}_1 \right\rangle$, the large part of $\boldsymbol{w}_{2\parallel}$ will be cancelled and will not affect the outer streaming $\boldsymbol{u}_{2\parallel}^{\mathrm{Out}}$. In full simulations however, one can get a large $\boldsymbol{v}_{2\parallel}$ inside the boundary layer.

Appendix D

Implementation of curvilinear coordinates in COMSOL

Imagine we have found the pressure field p_1 from which we can calculate the acoustic velocity field $\boldsymbol{u}_1$. We then now the components of $\boldsymbol{u}_1$ in our background frame (x, y, z). The velocity along the surface basis vectors (tangent and normal vectors) are then simply,

$$u_{1\xi} = \boldsymbol{t}_\xi \cdot \boldsymbol{u}_1 \equiv \texttt{uX1}, \qquad u_{1\eta} = \boldsymbol{t}_\eta \cdot \boldsymbol{u}_1 \equiv \texttt{uY1}, \qquad u_{1\zeta} = \boldsymbol{n} \cdot \boldsymbol{u}_1 \equiv \texttt{uZ1}. \tag{D.1}$$

Where the font `uX1` means a COMSOL definition. Similarly the spatial derivatives along the new basis vectors are

$$\partial_\xi = \boldsymbol{t}_\xi \cdot \boldsymbol{\nabla}, \qquad \partial_\eta = \boldsymbol{t}_\eta \cdot \boldsymbol{\nabla}, \qquad \partial_\zeta = \boldsymbol{n} \cdot \boldsymbol{\nabla}, \tag{D.2}$$

so e.g., with $i, j = \xi, \eta, \zeta$ and using the general basis vectors $\boldsymbol{e}_i$,

$$\partial_i u_{1j} = (\boldsymbol{e}_i \cdot \boldsymbol{\nabla})(\boldsymbol{e}_j \cdot \boldsymbol{u}_1) = \partial_i \boldsymbol{e}_j \cdot \boldsymbol{u}_1 + \boldsymbol{e}_j \cdot (\boldsymbol{e}_i \cdot \boldsymbol{\nabla})\boldsymbol{u}_1 \tag{D.3}$$

where (i'th row, j'th column)

$$\partial_i \boldsymbol{e}_j = \begin{bmatrix} \kappa_\xi \boldsymbol{n} & 0 & -\kappa_\xi \boldsymbol{t}_\xi \\ 0 & \kappa_\eta \boldsymbol{n} & -\kappa_\eta \boldsymbol{t}_\eta \\ 0 & 0 & 0 \end{bmatrix}. \tag{D.4}$$

D.1 2D geometry (η, ζ)

We now consider the case of two background dimensions (y, z) and also two curvilinear coordinates η, ζ which we will call (Y, Z) in COMSOL. Since the normal vector is usually out of a domain in COMSOL we should use,

$$\boldsymbol{n} \equiv \overbrace{(\texttt{Ny}, \texttt{Nz})}^{\text{Own definition}} = \overbrace{(-\texttt{ny}, -\texttt{nz})}^{\text{COMSOL}}, \qquad \boldsymbol{t}_\eta \equiv \overbrace{(\texttt{Ty}, \texttt{Tz})}^{\text{Own definition}} = \overbrace{(\texttt{Nz}, -\texttt{Ny})}^{\text{COMSOL}}. \tag{D.5}$$

The direction of the tangent vector is not that important in 2D but will be in 3D and hence we make the new definition with capital letters for consistency. Also the variable `curv` in COMSOL gives the curvature which is positive in the direction of the (COMSOL) normal vector. Hence this should also be redefined,

$$\kappa_\eta \equiv \overbrace{\texttt{KAP}}^{\text{Own definition}} = \overbrace{-\texttt{curv}}^{\text{COMSOL}}. \tag{D.6}$$

The derivatives are now obtained from Eqs. (D.3) and (D.4)

$$\begin{aligned}\partial_\eta u_{1\eta} &= \kappa_\eta u_{1\zeta} + \boldsymbol{t}_\eta \cdot (\boldsymbol{t}_\eta \cdot \boldsymbol{\nabla})\boldsymbol{u}_1 \\ &= \texttt{uY1Y} \equiv \texttt{KAP} * \texttt{uZ1} + \texttt{Ty} * (\texttt{Ty} * \texttt{uy1y} + \texttt{Tz} * \texttt{uy1z}) + \texttt{Tz} * (\texttt{Ty} * \texttt{uz1y} + \texttt{Tz} * \texttt{uz1z})\end{aligned} \tag{D.7a}$$

$$\begin{aligned}\partial_\eta u_{1\zeta} &= -\kappa_\eta u_{1\eta} + \boldsymbol{n} \cdot (\boldsymbol{t}_\eta \cdot \boldsymbol{\nabla})\boldsymbol{u}_1 \\ &= \texttt{uZ1Y} \equiv -\texttt{KAP} * \texttt{uY1} + \texttt{Ny} * (\texttt{Ty} * \texttt{uy1y} + \texttt{Tz} * \texttt{uy1z}) + \texttt{Nz} * (\texttt{Ty} * \texttt{uz1y} + \texttt{Tz} * \texttt{uz1z})\end{aligned} \tag{D.7b}$$

$$\begin{aligned}\partial_\zeta u_{1\eta} &= \boldsymbol{t}_\eta \cdot (\boldsymbol{n} \cdot \boldsymbol{\nabla})\boldsymbol{u}_1 \\ &= \texttt{uY1Z} \equiv \texttt{Ty} * (\texttt{Ny} * \texttt{uy1y} + \texttt{Nz} * \texttt{uy1z}) + \texttt{Tz} * (\texttt{Ny} * \texttt{uz1y} + \texttt{Nz} * \texttt{uz1z})\end{aligned} \tag{D.7c}$$

$$\begin{aligned}\partial_\zeta u_{1\zeta} &= \boldsymbol{n} \cdot (\boldsymbol{n} \cdot \boldsymbol{\nabla})\boldsymbol{u}_1 \\ &= \texttt{uZ1Z} \equiv \texttt{Ny} * (\texttt{Ny} * \texttt{uy1y} + \texttt{Nz} * \texttt{uy1z}) + \texttt{Nz} * (\texttt{Ny} * \texttt{uz1y} + \texttt{Nz} * \texttt{uz1z}).\end{aligned} \tag{D.7d}$$

D.2 3D geometry (ξ, η, ζ)

We now extend the 2D method such that the background coordinate system is (x, y, z) and curvilinear coordinate system is (ξ, η, ζ) which we call (X, Y, Z) in COMSOL. In 3D it is now important to choose the tangent vectors $\boldsymbol{t}_\xi$ and $\boldsymbol{t}_\eta$ to point in the principal direction of curvature. COMSOL is already equipped with the vectos $(\texttt{tcurv1x}, \texttt{tcurv1y}, \texttt{tcurv1z})$ and $(\texttt{tcurv2x}, \texttt{tcurv2y}, \texttt{tcurv2z})$ where the first points in the direction of the smallest principal curvature. Here positive principal curvature is to towards the normal direction. These two vectors are mutually orthogonal and are both orthogonal to the normal vector $\boldsymbol{n}$. However we have to be sure that $\boldsymbol{t}_\xi$,$\boldsymbol{t}_\eta$, $\boldsymbol{n}$ form a *right-handed* coordinate system. Hence we first define $\boldsymbol{n}$ and $\boldsymbol{t}_\xi$ and then choose $\boldsymbol{t}_\eta = \boldsymbol{n} \times \boldsymbol{t}_\xi$,

$$\boldsymbol{n} \equiv \overbrace{(\texttt{Nx}, \texttt{Ny}, \texttt{Nz})}^{\text{Own definition}} = \overbrace{(-\texttt{nx}, -\texttt{ny}, -\texttt{nz})}^{\text{COMSOL}}, \tag{D.8a}$$

$$\boldsymbol{t}_\xi \equiv (\texttt{TXx}, \texttt{TXy}, \texttt{TXz}) = (\texttt{tcurv1x}, \texttt{tcurv1y}, \texttt{tcurv1z}), \tag{D.8b}$$

$$\boldsymbol{t}_\eta \equiv (\texttt{TYx}, \texttt{TYy}, \texttt{TYz}) = (\texttt{Ny} * \texttt{TXz} - \texttt{Nz} * \texttt{TXy}, \texttt{Nz} * \texttt{TXx} - \texttt{Nx} * \texttt{TXz}, \texttt{Nx} * \texttt{TXy} - \texttt{Ny} * \texttt{TXx}). \tag{D.8c}$$

Similarly to 2D we define the curvatures,

$$\kappa_\xi \equiv \texttt{KAPX} = -\texttt{curv1}, \qquad \kappa_\eta \equiv \texttt{KAPY} = -\texttt{curv2}. \tag{D.9}$$

The components of $\boldsymbol{u}$ in the curvilinear coordinates are now found from Eq. (D.1) and derivatives from Eqs. (D.3) and (D.4). We write up the result here,

$$\partial_\xi u_{1\xi} = \texttt{uX1X} = \boldsymbol{t}_\xi \cdot (\boldsymbol{t}_\xi \cdot \boldsymbol{\nabla})\boldsymbol{u}_1 + \kappa_\xi u_{1\zeta}, \tag{D.10a}$$
$$\partial_\eta u_{1\xi} = \texttt{uX1Y} = \boldsymbol{t}_\xi \cdot (\boldsymbol{t}_\eta \cdot \boldsymbol{\nabla})\boldsymbol{u}_1, \tag{D.10b}$$
$$\partial_\zeta u_{1\xi} = \texttt{uX1Z} = \boldsymbol{t}_\xi \cdot (\boldsymbol{n} \cdot \boldsymbol{\nabla})\boldsymbol{u}_1, \tag{D.10c}$$
$$\partial_\xi u_{1\eta} = \texttt{uY1X} = \boldsymbol{t}_\eta \cdot (\boldsymbol{t}_\xi \cdot \boldsymbol{\nabla})\boldsymbol{u}_1, \tag{D.10d}$$
$$\partial_\eta u_{1\eta} = \texttt{uY1Y} = \boldsymbol{t}_\eta \cdot (\boldsymbol{t}_\eta \cdot \boldsymbol{\nabla})\boldsymbol{u}_1 + \kappa_\eta u_{1\zeta}, \tag{D.10e}$$
$$\partial_\zeta u_{1\eta} = \texttt{uY1Z} = \boldsymbol{t}_\eta \cdot (\boldsymbol{n} \cdot \boldsymbol{\nabla})\boldsymbol{u}_1, \tag{D.10f}$$
$$\partial_\xi u_{1\zeta} = \texttt{uZ1X} = \boldsymbol{n} \cdot (\boldsymbol{t}_\xi \cdot \boldsymbol{\nabla})\boldsymbol{u}_1 - \kappa_\xi u_{1\xi}, \tag{D.10g}$$
$$\partial_\eta u_{1\zeta} = \texttt{uZ1Y} = \boldsymbol{n} \cdot (\boldsymbol{t}_\eta \cdot \boldsymbol{\nabla})\boldsymbol{u}_1 - \kappa_\eta u_{1\eta}, \tag{D.10h}$$
$$\partial_\zeta u_{1\zeta} = \texttt{uZ1Z} = \boldsymbol{n} \cdot (\boldsymbol{n} \cdot \boldsymbol{\nabla})\boldsymbol{u}_1, \tag{D.10i}$$

Bibliography

[1] W. L. Nyborg, *Acoustic streaming near a boundary*. J. Acoust. Soc. Am. **30**(4), 329–339 (1958).

[2] J. D. Adams, C. L. Ebbesen, R. Barnkob, A. H. J. Yang, H. T. Soh, and H. Bruus, *High-throughput, temperature-controlled microchannel acoustophoresis device made with rapid prototyping*. J Micromech Microeng **22**(7), 075017 (2012).

[3] P. Augustsson, J. T. Karlsen, H.-W. Su, H. Bruus, and J. Voldman, *Iso-acoustic focusing of cells for size-insensitive acousto-mechanical phenotyping*. Nat. Commun. **7**, 11556 (2016).

[4] P. Thevoz, J. D. Adams, H. Shea, H. Bruus, and H. T. Soh, *Acoustophoretic synchronization of mammalian cells in microchannels*. Anal. Chem. **82**(7), 3094–3098 (2010).

[5] R. Barnkob, *Physics of microparticle acoustophoresis*. Ph.D. thesis, DTU (2012, http://wwwstaffdtudk/bruus/Researchgroup/TMFthesesPhDaspx).

[6] M. Settnes and H. Bruus, *Forces acting on a small particle in an acoustical field in a viscous fluid*. Phys. Rev. E **85**, 016327 (2012).

[7] Lord Rayleigh, *On the circulation of air observed in Kundt's tubes, and on some allied acoustical problems*. Philos. Trans. R. Soc. London **175**, 1–21 (1884).

[8] C. Eckart, *Vortices and streams caused by sound waves*. Phys. Rev. **73**, 68–76 (1948).

[9] H. Schlichting, *Berechnung ebener periodischer grenzeschichtströmungen*. Phys. Z. **33**, 327–335 (1932).

[10] C. Lee and T. Wang, *Near-boundary streaming around a small sphere due to 2 orthogonal standing waves*. J. Acoust. Soc. Am. **85**(3), 1081–1088 (1989).

[11] J. Vanneste and O. Bühler, *Streaming by leaky surface acoustic waves* **467**, 1779–1800 (2010).

[12] P. B. Muller, R. Barnkob, M. J. H. Jensen, and H. Bruus, *A numerical study of microparticle acoustophoresis driven by acoustic radiation forces and streaming-induced drag forces*. Lab Chip **12**, 4617–4627 (2012).

[13] B. Hammarström, T. Laurell, and J. Nilsson, *Seed particle enabled acoustic trapping of bacteria and nanoparticles in continuous flow systems.* Lab Chip **12**, 4296–4304 (2012).

[14] H. Bruus, *Theoretical Microfluidics* (Oxford University Press, Oxford) (2008).

[15] P. B. Muller and H. Bruus, *Numerical study of thermoviscous effects in ultrasound-induced acoustic streaming in microchannels.* Phys. Rev. E **90**(4), 043016 (2014).

[16] C. E. Bradley, *Acoustic streaming field structure: the influence of the radiator.* The Journal of the Acoustical Society of America **100**(3), 1399–1408 (1996).

[17] COMSOL Multiphysics 5.2, www.comsol.com (2015).

[18] T. Banchoff and S. Lovett, *Differential geometry of curves and surfaces* (2010).

[19] A. Christakou, M. Ohlin, B. Onfelt, and M. Wiklund, *Ultrasonic three-dimensional on-chip cell culture for nynamic studies of tumor immune surveillance by natural killer cells.* Lab Chip **15**(15), 3222–3231 (2015).

[20] L. D. Landau and E. M. Lifshitz, *Fluid Mechanics*, vol. 6 (Pergamon Press, Oxford), 2nd edn. (1993).

[21] J. T. Karlsen, *Theory of thermoviscous acoustofluidics in microsystems.* Master's thesis (2014, http://wwwstaffdtudk/bruus/Researchgroup/TMFthesesMScaspx).

[22] J. Lei, P. Glynne-Jones, and M. Hill, *Modal rayleigh-like streaming in layered acoustofluidic devices.* Phisics of fluids **28**, 012004 (2016).

[23] J. Lei, M. Hill, and P. Glynne-Jones, *Numerical simulation of 3d boundary-driven acoustic streaming in microfluidic devices.* Lab Chip **14**(3), 532–541 (2014).

[24] C. P. Lee and T. G. Wang, *Outer acoustic streaming* **88 (5)**, 2367–2375 (1990).

[25] M. Settnes and H. Bruus, *Theoretical analysis of viscous corrections to the acoustic radiation force on cells in microchannel acoustophoresis.* In J. Landers, A. Herr, D. Juncker, N. Pamme, and J. Bienvenue (eds.), *Proc. 15th MicroTAS, 2 - 6 October 2011, Seattle (WA), USA*, 160–162 (CBMS) (2011).

[26] S. M. Hagsäter, T. G. Jensen, H. Bruus, and J. P. Kutter, *Acoustic resonances in microfluidic chips: full-image micro-PIV experiments and numerical simulations.* Lab Chip **7**(10), 1336–1344 (2007).

[27] M. Antfolk, P. B. Muller, P. Augustsson, H. Bruus, and T. Laurell, *Focusing of sub-micrometer particles and bacteria enabled by two-dimensional acoustophoresis.* Lab Chip **14**, 2791–2799 (2014).

[28] H. Lei, D. A. Fedosov, B. Caswell, and G. E. Karniadakis, *Blood flow in small tubes: quantifying the transition to the non-continuum regime.* J. Fluid Mech. **722**, 214–239 (2013).